

Cranked Relativistic Hartree-Bogoliubov Theory: probing the gateway to superheavy nuclei

A. V. Afanasjev^(1,2,3), T. L. Khoo⁽¹⁾, S. Frauendorf^(2,4), G. A. Lalazissis⁽⁵⁾, I. Ahmad⁽¹⁾

¹*Physics Division, Argonne National Laboratory, Argonne, IL 60439, USA*

²*Department of Physics, University of Notre Dame, Notre Dame, Indiana 46556, USA*

³*Laboratory of Radiation Physics, Institute of Solid State Physics, University of Latvia,
LV 2169 Salaspils, Miera str. 31, Latvia*

⁴*IKH, Research Center Rossendorf, Dresden, Germany*

⁵*Department of Theoretical Physics, Aristotle University of Thessaloniki, GR-54124,
Thessaloniki, Greece*

(November 2, 2018)

Abstract

The cranked relativistic Hartree+Bogoliubov theory has been applied for a systematic study of the nuclei around ^{254}No , the heaviest elements for which detailed spectroscopic data are available. The deformation, rotational response, pairing correlations, quasi-particle and other properties of these nuclei have been studied with different parametrizations for the effective mean-field Lagrangian. Pairing correlations are taken into account by a finite range two-body force of Gogny type. While the deformation properties are well reproduced, the calculations reveal some deficiencies of the effective forces both in the particle-hole and particle-particle channels. For the first time, the quasi-particle spectra of odd deformed nuclei have been calculated in a fully self-consistent way within the framework of the relativistic mean field (RMF) theory. The energies of the spherical subshells, from which active deformed states of these nuclei emerge, are described with an accuracy better than 0.5 MeV for most of the subshells with the NL1 and NL3 parametrizations. However, for a few subshells the discrepancies reach 0.7-1.0 MeV. In very heavy systems, where the level density is high, this level of accuracy is not sufficient for reliable predictions of the location of relatively small deformed shell gaps. The calculated moments of inertia reveal only small sensitivity to the RMF parametrization and, thus, to differences in the single-particle structure. However, in contrast to lighter systems, it is necessary to decrease the strength of the D1S Gogny force in the pairing channel in order to reproduce the moments of inertia.

PACS: 21.60.Cs, 21.60Jz, 27.90.+b, 21.10.Pc

I. INTRODUCTION

The possible existence of shell-stabilized superheavy nuclei, predicted with realistic nuclear potentials [1–3] and the macroscopic-microscopic (MM) method [4–6], has been a driving force behind experimental and theoretical efforts to investigate the superheavy nuclei. These investigations pose a number of experimental and theoretical challenges. The recent discovery of elements with $Z=112$ [7], $Z=114$ [8] and $Z=116$ [9] (for review of the present experimental situation see Refs. [10–12]) clearly shows great progress on the experimental side, but also indicates difficulties in the investigation of nuclei with low production cross-sections and analyses based only on 1 or 2 events.

The theoretical challenges are also considerable since different theoretical methods predict different spherical shell closures. Modern calculations based on the MM method with the Woods-Saxon [4,13,14], Nilsson [5], and folded Yukawa [15] potentials indicate $Z = 114$ and $N = 184$ as the spherical shell closures. It is necessary to say, however, that some earlier calculations indicated $Z = 126$ as a possible magic number (see Ref. [10] for a review). There are differences in the predictions of self-consistent calculations, which depend both on the approach and on the effective force. Self-consistent calculations based on the Hartree-Fock method with Skyrme forces (SHF) predict spherical shell closures at $Z = 126$ and $N = 184$ for most of the forces [14,16,17]. However, some forces indicate $Z = 114$ (SkI4) and $Z = 120$ (SkI3) as proton shell closures, while some predict no doubly magic superheavy nuclei at all. On the other hand, the relativistic mean field theory (RMF) prefers $Z = 120$ and $N = 172$ as spherical shell closures [16,17]. However, $Z = 114$ and $N = 184$ also appear as the shell closures in some RMF calculations [18,19]. For a detailed comparison of the predictions of the different Skyrme and RMF calculations, see Refs. [17,20]. Hartree-Fock-Bogoliubov (HFB) calculations with the Gogny force give $Z = 120, 126$ and $N = 172, 184$ as spherical shell closures [21].

Clearly, the accuracy of predictions of spherical shell closures depends sensitively on the accuracy of describing the single-particle energies, which becomes especially important for superheavy nuclei, where the level density is very high. Variations in single-particle energy of 1 – 1.5 MeV yield spherical shell gaps at different particle numbers, which restricts the reliability in extrapolating to the unknown region.

Usually, the MM method describes the single-particle energies rather well. This is due to the fact that the experimental data on single-particle states are used directly in the parametrization of the single-particle potential. Moreover, different parametrizations of the single-particle potential are used in different mass regions. However, the extrapolation of the single-particle potential may be much less reliable since it is not determined self-consistently. For example, microscopic models predict that the appearance of the shell closures in superheavy nuclei is influenced by a central depression of the nuclear density distribution [17,22]. This effect cannot be treated in self-consistent way in current MM models.

Although the nucleonic potential is defined in SHF and RMF approaches in a fully self-consistent way, this does not guarantee that single-particle degrees of freedom are accurately described, as indicated by the large variety of the parametrizations (more than 60 for SHF and about 20 for RMF [20]). In addition, the parameters have been fitted in almost all cases to the bulk properties of spherical nuclei. Single-particle information on spin-orbit splittings

is used only in the fits of the parameters of the Skyrme and Gogny forces. The spin-orbit interaction is a relativistic effect, which arises naturally in the RMF theory. Thus, available RMF fits were obtained without the use of any single-particle information. For heavy nuclei, the calculated RMF single-particle states were directly compared with experimental data only in spherical nuclei (see, for example, Refs. [23,24] and references quoted therein). These comparisons, however, do not reveal the accuracy of the description of the single-particle states because the particle-vibration coupling, which can affect considerably the energies of single-particle states in spherical nuclei [25–27], has been neglected.

Compared with the MM method, self-consistent calculations have been confronted with experiment to a lesser degree and for a smaller number of physical observables (mainly binding energies and quantities related to their derivatives). For many parametrizations, even the reliability of describing conventional nuclei is poorly known. In such a situation, it is important to perform a comprehensive study of the heaviest nuclei for which detailed spectroscopic information is available. *The results of such a study will allow us to better judge the reliability of predictions for superheavy nuclei.* The experimental data on deformed nuclei around ^{254}No provides sufficient information for such a test. The purpose of this work is to compare the predictions of RMF theory with these data.

RMF calculations have been compared with experiment in this mass region in only Ref. [28]. However, the comparison was restricted to binding energies and quantities related to their derivatives. In addition, the pair correlations were treated in the BCS approximation, with no particle number projection.

In the present manuscript, the cranked relativistic Hartree-Bogoliubov (CRHB) theory [29,30], with approximate particle number projection by means of the Lipkin-Nogami method (CRHB+LN theory), is employed for a detailed investigation of a wide set of experimental observables. The use of the Lipkin-Nogami method has the clear advantage of avoiding the collapse of pairing correlations at large shell gaps. We address for the first time the question of the blocking procedure in odd mass nuclei in the framework of the RMF theory, with effects of time-reversal symmetry breaking taken into account in a fully self-consistent way. The calculated binding energies, deformations, moments of inertia and quasi-particle states are compared with experiment.

The paper is organized in the following way. In Sect. II, a brief description of the CRHB+LN theory and of some specific features of the present calculations are given. In order to outline the general features of the evolution of physical observables as a function of proton and neutron number, systematic calculations with different RMF parametrizations are performed along the $Z = 100$ (Fm) isotope and $N = 152$ isotone chains. In addition, calculations are carried out for Cm, Cf and No nuclei, for which experimental data are available. The rotational properties are studied in detail in Sect. III, the deformations are discussed in Sect. IV and the shell structure in Sect. V. The quasiparticle spectra of selected nuclei are compared with experiment in Sect. VI. Finally, Sect. VII summarizes our main conclusions.

II. THEORETICAL FORMALISM

In relativistic mean field (RMF) theory [23,31,32] the nucleus is described as a system of point-like nucleons (Dirac spinors) coupled to mesons and photons. The nucleons interact

by exchanging scalar σ -mesons, vector ω -, ρ - mesons and photons. The isoscalar-scalar σ -mesons generate strong intermediate range attraction between the nucleons. For the vector particles we have to distinguish the time-like and the space-like components. In the case of photons, they correspond to the Coulomb field and the magnetic field when currents are present. For the isoscalar-vector ω -meson, the time-like component provides a very strong repulsion at short distances for all combinations of nucleons, pp , nn and pn . For the isovector-vector ρ -meson, the time-like components give rise to a short range repulsion for like nucleons (pp and nn) and a short range attraction for unlike nucleons (np). They also have a strong influence on the symmetry energy. The space-like components of the ω - and ρ -mesons lead to an interaction between currents, which is attractive in the case of the ω -meson for all combinations (pp , nn and pn) and in the case of the ρ -meson attractive for pp and nn , but repulsive for pn . Within the mean field theory, these currents only occur in cases of time-reversal breaking mean fields, which applies to rotating or odd-mass nuclei.

The cranked relativistic Hartree-Bogoliubov (CRHB) theory [29,30] extends the RMF theory to rotating nuclei and includes pairing correlations. If an approximate particle number projection is performed by means of the Lipkin-Nogami (LN) method [33–36], the abbreviation CRHB+LN will be used. Since the theory is described in detail in Ref. [30], only the features important for the present discussion will be outlined below.

A. The CRHB+LN equations

The CRHB+LN equations for the fermions in the rotating frame are given by [30]

$$\begin{pmatrix} \hat{h}'_D - \lambda' - \Omega_x \hat{J}_x & \hat{\Delta} \\ -\hat{\Delta}^* & -\hat{h}'_D^* + \lambda' + \Omega_x \hat{J}_x^* \end{pmatrix} \begin{pmatrix} U(\mathbf{r}) \\ V(\mathbf{r}) \end{pmatrix}_k = E'_k \begin{pmatrix} U(\mathbf{r}) \\ V(\mathbf{r}) \end{pmatrix}_k, \quad (1)$$

where

$$\hat{h}'_D = \hat{h}_D + 4\lambda_2\rho - 2\lambda_2 Tr(\rho), \quad (2)$$

$$\lambda' = \lambda_1 + 2\lambda_2, \quad (3)$$

$$E'_k = E_k - \lambda_2. \quad (4)$$

Here, \hat{h}_D is the Dirac Hamiltonian for the nucleon with mass m ; λ_1 is defined from the average particle number constraints for protons and neutrons; $\rho_\tau = V_\tau^* V_\tau^T$ is the density matrix; $U_k(\mathbf{r})$ and $V_k(\mathbf{r})$ are quasiparticle Dirac spinors; E_k denotes the quasiparticle energies; and \hat{J}_x is the angular momentum component. The LN method corresponds to a restricted variation of $\lambda_2 \langle (\Delta N)^2 \rangle$ (see Ref. [30] for definitions of λ_1 and λ_2), where λ_2 is calculated self-consistently in each step of the iteration. The form of the CRHB+LN equations given above corresponds to the shift of the LN modification into the particle-hole channel.

The Dirac Hamiltonian \hat{h}_D contains an attractive scalar potential $S(\mathbf{r})$

$$S(\mathbf{r}) = g_\sigma \sigma(\mathbf{r}), \quad (5)$$

a repulsive vector potential $V_0(\mathbf{r})$

$$V_0(\mathbf{r}) = g_\omega \omega_0(\mathbf{r}) + g_\rho \tau_3 \rho_0(\mathbf{r}) + e \frac{1 - \tau_3}{2} A_0(\mathbf{r}), \quad (6)$$

and a magnetic potential $\mathbf{V}(\mathbf{r})$

$$\mathbf{V}(\mathbf{r}) = g_\omega \boldsymbol{\omega}(\mathbf{r}) + g_\rho \tau_3 \boldsymbol{\rho}(\mathbf{r}) + e \frac{1 - \tau_3}{2} \mathbf{A}(\mathbf{r}). \quad (7)$$

The last term breaks time-reversal symmetry and induces currents. In rotating nuclei, the time-reversal symmetry is broken by the Coriolis field. Without rotation, it is broken when the time-reversal orbitals are not occupied pairwise. In the Dirac equation, the space-like components of the vector mesons $\boldsymbol{\omega}(\mathbf{r})$ and $\boldsymbol{\rho}(\mathbf{r})$ have the same structure as the space-like component $\mathbf{A}(\mathbf{r})$ generated by the photons. Since $\mathbf{A}(\mathbf{r})$ is the vector potential of the magnetic field, by analogy the effect due to presence of the vector field $\mathbf{V}(\mathbf{r})$ is called *nuclear magnetism* [37]. It has considerable influence on the magnetic moments [38] and the moments of inertia [39–41]. In the present calculations the spatial components of the vector mesons are properly taken into account in a fully self-consistent way. The detailed description of the mesonic degrees of freedom in the CRHB+LN theory is presented in Ref. [30].

The pair field $\hat{\Delta}$ is given by

$$\hat{\Delta} \equiv \Delta_{ab} = \frac{1}{2} \sum_{cd} V_{abcd}^{pp} \kappa_{cd} \quad (8)$$

where the indices a, b, \dots denote quantum numbers which specify the single-particle states with the space coordinates \mathbf{r} , as well as the Dirac and isospin indices s and τ . It contains the pairing tensor κ

$$\kappa = V^* U^T \quad (9)$$

and the matrix elements V_{abcd}^{pp} of the effective interaction in the particle-particle (pp) channel, for which the phenomenological non-relativistic Gogny-type finite range interaction

$$V^{pp}(1, 2) = f \sum_{i=1,2} e^{-[(\mathbf{r}_1 - \mathbf{r}_2)/\mu_i]^2} \times (W_i + B_i P^\sigma - H_i P^\tau - M_i P^\sigma P^\tau) \quad (10)$$

is used. The clear advantage of such a force is that it provides an automatic cutoff of high-momentum components. The motivation for such an approach to the description of pairing is given in Ref. [30,42]. In Eq. (10), μ_i , W_i , B_i , H_i and M_i ($i = 1, 2$) are the parameters of the force and P^σ and P^τ are the exchange operators for the spin and isospin variables, respectively. Note that a scaling factor f is introduced in Eq. (10). In our previous studies, the original (scaling factor $f = 1.0$) parameter set D1S [43,44] provided a good description of the moments of inertia in the $A \sim 75$ [45], $A \sim 160 - 170$ [46] and $A \sim 190$ [29,30] mass regions. As discussed in Sect. III B, it produces pairing correlations in the $A \sim 250$ mass region that are too strong, and, thus, it has to be attenuated ($f < 1.0$).

As a measure for the size of the pairing correlations in Hartree-(Fock)-Bogoliubov calculations, we use the pairing energy

$$E_{pairing} = -\frac{1}{2} \text{Tr}(\Delta \kappa). \quad (11)$$

B. The RMF parametrizations

In the present study, the NL1 [47], NL-Z [48], NL3 [49], NLSH [50] and NL-RA1 [19] parametrizations will be compared in order to see how well observables, such as the moments of inertia, the deformations, the quasiparticle energies, the separation energy and the quantity $\delta_{2n}(Z, N)$ related to its derivative, agree with each other and with experiment.

These sets differ in the experimental input used in the fitting procedure. The binding energies of a number of spherical nuclei were included in the fit of all those sets, but the selection of nuclei was different. NL1 and NL-Z employ the data mainly from the valley of beta-stability, while additional information on neutron-rich nuclei has been used in the fit of the NL3 set. Moreover, there is a difference in the selection of additional observables used in the fit. Charge diffraction radii and surface thicknesses were included in the fit of NL1 and NL-Z sets [47,48]. The NL-Z set is a re-fit of NL1 where the correction for spurious center-of-mass motion is calculated from an actual many-body wave function [48]. On the contrary, NL3 and NLSH employ data on charge and neutron radii [49,50]. This (together with the fact that in the NL3 set more experimental data on neutron rich nuclei were used in fitting procedure) provides better a description of isospin, surface and symmetry properties of finite nuclei in the NL3 and NLSH sets. Unfortunately, Ref. [19] does not state which data the NL-RA1 set is fitted to.

The sets NL1, NL3 and NLSH have been used extensively in RMF studies and tested on a wide range of physical observables related, for example, to the ground state properties, rotational properties, properties of giant resonances etc.; see Ref. [23] for review. The sets NL-Z and NL-RA1 have been tested only for observables related to ground state properties. The set NL-Z is a re-fit of NL1 with a correction for spurious center-of-mass motion [48] given by

$$E_{cm} = -\langle \hat{\mathbf{P}}_{cm}^2 \rangle / 2mA, \quad (12)$$

where $\hat{\mathbf{P}}_{cm}$ is the total momentum operator in the center-of-mass frame, m is the nucleon mass and A the mass number. This term is added after the variation is performed to circumvent two-body terms in the mean field equations. Thus, the use of other prescriptions instead of Eq. (12) for the treatment of the center-of-mass motion with NL-Z will affect only the binding energies and the quantities related to their derivatives. In all our calculations (including those with NL-Z), the correction for the spurious center-of-mass motion is approximated by its value in a nonrelativistic harmonic oscillator potential

$$E_{cm} = -\frac{3}{4}41A^{-1/3} \quad \text{MeV.} \quad (13)$$

This is consistent with the NL1, NL3, NLSH and NL-RA1 parametrizations. As illustrated in Ref. [51], Eq. (13) is a very good approximation to Eq. (12) in the $A \sim 250$ mass region: the difference between two prescriptions does not exceed 0.3 MeV, which is only $\approx 0.017\%$ correction to the typical binding energy and changes smoothly with the mass number A . Based on the results given in Fig. 2 of Ref. [51] one can estimate that in this mass region the use of Eq. (13) instead of Eq. (12) will affect two-particle separation energies $S_{2n}(Z, N)$ and $\delta_{2n}(Z, N)$ by at most 0.030 MeV. This justifies the use of Eq. (13) for NL-Z.

The parametrization NL-RA1 has been introduced recently in Ref. [19]. A number of conclusions of this article has been strongly questioned in Ref. [52], in part due to the use of an unrealistically strong pairing interaction. However, if a more realistic pairing is employed, this parametrization provides a rather good description of the binding energies (see Fig. 2 in Ref. [52]).

C. Details of the calculations

The CRHB(+LN) equations are solved in the basis of an anisotropic three-dimensional harmonic oscillator in Cartesian coordinates with the deformation parameters $\beta_0 = 0.3$, $\gamma = 0^\circ$ and oscillator frequency $\hbar\omega_0 = 41A^{-1/3}$ MeV. All fermionic and bosonic states belonging to the shells up to $N_F = 14$ and $N_B = 16$ are taken into account in the diagonalization of the Dirac equation and the matrix inversion of the Klein-Gordon equations, respectively. The detailed investigation of $^{246,248,250}\text{Fm}$ indicates that this truncation scheme provides reasonable numerical accuracy. The values of the kinematic moment of inertia $J^{(1)}$, charge quadrupole moment Q_0 , mass hexadecapole moment Q_{40} , binding energies, separation energies $S_{2n}(Z, N)$, and $\delta_{2n}(Z, N)$ obtained with truncation of the basis at $N_F = 14$ and $N_B = 16$ differ from the values obtained with $N_F = 18$ and $N_B = 18$ by less than 0.75%, 0.9%, 3.4%, 0.1%, 40 keV, and 40 keV, respectively. The convergence in energy of our calculations is similar to that reported in non-relativistic calculations of Ref. [53] based on the Gogny force.

III. ROTATIONAL RESPONSE

A. The ^{254}No ground band

The observed moments of inertia of the ground band in ^{254}No [54–56] are compared with the calculated values in Fig. 1. The CRMF calculations without pairing, based on the NL1 parameterization, marked as CRMF(NL1) in Fig. 1a, provide an almost constant kinematic moment of inertia $J^{(1)} \approx 87 \text{ MeV}^{-1}$ up to $\Omega_x \sim 0.26$ MeV and a dynamic moment of inertia which slightly increases with rotational frequency. A band crossing with another configuration takes place at $\Omega_x \sim 0.26$ MeV. These calculations provide a reference point for how much the moments of inertia decrease due to pairing. It is interesting to note that the moments of inertia in the calculations without pairing are only one half of the rigid body value. This unexpected result will be discussed in detail in forthcoming article [45].

The CRHB calculations without particle number projection (scaling factor $f = 1$), marked as CRHB (NL1+D1S) in Fig. 1b, agree very well with experiment up to $\Omega_x = 0.18$ MeV. At higher frequency, experiment and theory diverge. With approximate particle number projection using the LN method, marked as NL1+D1S+LN in Fig. 1c, the theory underestimates the experimental kinematic and dynamic moments of inertia by $\sim 25\%$. This result is in contrast with the good agreement obtained by the same method for superdeformed bands with $A \sim 190$ [29,30] and for nuclei in the rare-earth [46] and $A \sim 75$ [45] regions.

Different parametrizations of the RMF Lagrangian give quite similar results for the moments of inertia if $f = 1$. For example, the results of the CRHB+LN calculations based on the NL3 parametrization [49] (marked as NL3+D1S+LN in Fig. 1c) provide moments of inertia which are only slightly lower (by ≈ 3 MeV $^{-1}$) than the ones obtained with the NL1 parametrization. The CRHB+LN calculations with the NL-Z [48], NLSH [50] and NL-RA1 [19] parametrizations of the RMF Lagrangian give results which are quite similar to those obtained with NL3¹ and, thus, they are not shown in Fig. 1. The moments of inertia are very similar despite the differences in the single-particle spectra near the Fermi level (see Figs. 2 and 3). Hence, the most likely reason for discrepancies between experiment and the CRHB+LN calculations lies in an inadequate parametrization of the Gogny force (D1S) in the particle-particle channel for this mass region, which gives too strong pair correlations. This is not quite unexpected since no experimental data above ^{208}Pb have been used when the D1S set was fitted. The study of other heavy nuclei around ^{254}No also shows that the kinematic moments of inertia obtained in the CRHB+LN calculations with the original D1S force (scaling factor $f = 1.0$) are systematically lower than experimental ones (by $\sim 20\%$ in even-even $^{236-244}\text{Pu}$ nuclei). Different parametrizations of the RMF Lagrangian give similar results and the deformations of these nuclei are well described in the calculations (see Sect. IV). It is unlikely that other available parametrizations for the Gogny force such as D1 [61] and D1P [62] will improve the situation, since they produce even stronger pairing than the D1S set in superdeformed bands of the $A \sim 190$ mass region [29].

The results of the calculations for the ^{254}No rotational band obtained in the non-relativistic cranked HFB approach based on the Gogny force with D1S set of parameters [65] seem to support this interpretation. These calculations, which are performed without particle number projection, also come very close to the data. One presumes that the inclusion of particle number projection by means of the LN method will lower the calculated kinematic moment of inertia, as has been seen in the rare-earth region [46], leading to a similar situation as described above.

B. Selection of the pairing strength

Quantitative information on the strength of the pair correlations can be extracted from the odd-even mass differences, excitation energies of high-K isomers or the moments of inertia. We use the moments of inertia for an adjustment of the strength of the Gogny force because they are not too sensitive to the details of the single-particle spectrum (see above).

Our CRHB+LN calculations indicate that in the $A \sim 250$ mass region the strength of pairing correlations should be reduced in order to reproduce the observed moments of inertia. The scaling factor f of the Gogny D1S force (see Eq. (10)) has been chosen to reproduce the experimental kinematic moment of inertia of ^{254}No at rotational frequency $\Omega_x = 0.15$

¹The CRMF calculations (without pairing) for the ground state band in ^{254}No also show a weak dependence of the moments of inertia on the RMF parametrization, and, thus on details of the single-particle structure. A similar situation has been encountered earlier in the $A \sim 60$ [57] and $A \sim 150$ [58–60] mass regions of superdeformation.

MeV. The values found for the various parametrizations of the RMF Lagrangian are given in Table I. These scaling factors, which are nearly the same, are used in all subsequent calculations, unless otherwise specified. The scaled CRHB+LN calculations reproduce the amplitude and the Ω_x -dependence of the dynamic and the kinematic moments of inertia in ^{254}No (see Fig. 4b,d) rather well. With NL3, experiment and theory agree very well, while with NL1 some discrepancy develops above $\Omega_x = 0.2$ MeV. Our choice of the scaling factor f leads also to a reasonable description of the odd-even mass differences in the CRHB+LN calculations (see columns 5 and 6 in Table II).

The need for attenuation of the D1S force within the framework of the CRHB+LN theory is not surprising since its pairing properties were adjusted by fitting only the odd-even mass differences of the Sn isotopes. Thus the quality of the description of pairing may deteriorate far from this mass region. Indeed, the moments of inertia of nuclei in mass regions closer to the Sn region, such as the rare-earth region [46], the superdeformed $A \sim 190$ mass region [29,30] and neutron-deficient $A \sim 75$ region [45], are described well by means of CRHB+LN calculations using the original D1S force.

CRHB calculations (without LN) with original scaling factor $f = 1.0$ provide a reasonable description of both moments of inertia before band crossing (see Fig. 1b) and odd-even mass differences (see Table II). This approach will be applied to the calculations of the quasiparticle spectra in odd nuclei (see Sects. VI E and VI D), for which the CRHB+LN calculations are numerically less stable. However, it is not justified for the calculations at large rotational frequencies because an unphysical pairing collapse takes place above the crossing between the ground and S -bands.

C. High-spin behavior

Alignment and backbending features of the rotational bands in the actinide region have been discussed in a number of publications; see Refs. [66,67] and references quoted therein. In this mass region, two high- j shells ($i_{13/2}$ for protons and $j_{15/2}$ for neutrons) come close to the Fermi surface and the angular momentum of quasiparticles in either orbital can align with the axis of rotation. The CRHB+LN calculations with the NL3 parametrization show that the alignment of the proton $i_{13/2}$ pair ($\pi[633]7/2$) and neutron $j_{15/2}$ pair ($\nu[734]9/2$) (see Fig. 5) takes place simultaneously in ^{254}No at $\Omega_x \approx 0.32$ MeV (see Fig. 6). The total angular momentum gain at the band crossing is $\approx 17\hbar$, with proton and neutron contributions of $\approx 7\hbar$ and $\approx 10\hbar$, respectively. The alignment leads to a decrease of the mass quadrupole moment Q_0 , to a sign change of the mass hexadecapole moment Q_{40} and to an appreciable increase of γ -deformation (see Fig. 7a,b,c). A similar situation holds also in ^{252}No , but the total angular momentum gain at the band crossing is smaller ($\approx 11\hbar$).

The simultaneous alignment of proton and neutron pairs occurs also in calculations with NL1. The crossing frequency is shifted down by ≈ 0.01 MeV (see caption of Fig. 4), the angular momentum gain at the band crossing is slightly different, and the high- j particles align in ^{252}No more gradually.

Our results differ from those of the cranked HFB calculations based on the Gogny force [65], which indicate in ^{254}No upbending at $I \sim 30\hbar$ and backbending at $I \sim 38\hbar$. These calculations are performed without particle number projection, which result in a collapse of neutron pairing correlations at relatively low spin, $I \sim 20\hbar$. In our calculations, the pairing

energies decrease with increasing rotational frequency due to the Coriolis anti-pairing effect, but there is no collapse of pairing (see Fig. 7d). The experimental data do not extend up to predicted backbending and thus do not discriminate between these calculations.

D. ^{252}No versus ^{254}No

The kinematic and dynamic moments of inertia of the band in ^{252}No show similar trends in rotational frequency as the experimental data (see Fig. 4a,c). In experiment, the moments of inertia at low rotational frequencies are smaller for $N = 150$ than for $N = 152$, in contrast with the calculations. One possible reason is the fact that the CRHB+LN calculations give deformed shell gaps at $N = 148$ and/or 150 (dependent on parametrization), rather than at $N = 152$ as seen in experiment (see Sects. V and VI for details). Indeed, in the calculations with the NL3 set the neutron contribution to the total moment of inertia (see Fig. 8) increases at the $N = 148$ shell gap, most likely due to the weakening of the neutron pair correlations (see the pairing energies for the Fm isotopes in Fig. 9, which are similar to those for the No isotopes). This suggests that if the calculations were to give a shell gap at $N = 152$, the relative magnitudes of the moments of inertia in $^{252,254}\text{No}$ would be reproduced.

E. Results for other nuclei and general trends of the moments of inertia as functions of the particle number

Figures 10 and 11 demonstrate that the N -dependence of the moments of inertia in $^{254,256}\text{Fm}$ and $^{248,250,252}\text{Cf}$ is rather well described in all parametrizations, whereas some problems exist for $^{242-250}\text{Cm}$ (see Fig. 11a). The absolute values are typically reproduced within a few % in the Fm and Cf isotopes, but the discrepancy between experiment and calculations becomes somewhat larger for the Cm isotopes. The experimental values of the moments of inertia in the $N = 152$ isotopes are reproduced rather well in all RMF parametrizations, with the exception of NLSH, which somewhat underestimates the moments of inertia (see Fig. 12). One should note, however, that the maximum value of $J^{(1)}$ is at $Z = 96$ in the calculations, while available data show the maximum at $Z = 98$.

It is interesting to compare the present CRHB+LN results with those from other models. The calculations using the MM method in Ref. [68] agree reasonably well with experimental excitation energies of $E(2^+)$ states and thus with the moments of inertia (see Figs. 10, 11 and 12) in this mass region. This is not surprising considering that these data have been used in the fit of the strengths (monopole and isospin-dependent) of the proton and neutron pairing correlations. However, despite the use of 4 adjustable parameters for pairing and better single-particle spectra obtained in the Woods-Saxon potential, the overall level of agreement is comparable with that obtained in the CRHB+LN calculations (see Figs. 10, 11 and 12). For example, a detailed examination indicates that the N -dependence is not described correctly for $^{248,250}\text{Cf}$ and $^{244,246}\text{Cm}$ (see Table 1 in Ref. [68] and Fig. 11 in the present manuscript). A similar problem exists for the Z -dependence of the moments of inertia in ^{254}No and ^{250}Cf nuclei (see Fig. 12). This suggests that the description of the single-particle states within the Woods-Saxon potential, with the “universal” set of parameters [69], is still not completely correct in this mass region, despite the fact that the

systematics of the experimental data on both spherical and deformed odd-mass nuclei were simultaneously taken into account in the fit of these parameters.

While there are several calculations of the moments of inertia by means of the MM method in the actinide and trans-actinide regions (see Ref. [68] and references therein), little has been done in microscopic approaches so far. The rotational bands in $^{252,254}\text{No}$ have been studied in the cranked HFB approaches based on the Skyrme [70,71] and Gogny forces [65,72] (see discussion above). The relative magnitude of the moments of inertia of these two nuclei is not reproduced in either approach (see, for example, Fig. 6 in Ref. [70]). In the calculations with Skyrme forces, this is most likely due to the fact that the deformed shell gap appears at $N = 150$ [28], instead of the experimentally observed value of $N = 152$.

The systematic calculations for the Fm isotopes and $N = 152$ isotones permit the following general observations. Different RMF parametrizations give similar N - and Z -dependencies of the moment of inertia (see Figs. 10 and 12). In the Fm isotopes, the correlation between the calculated quadrupole deformations β_2 (see Fig. 14) and moments of inertia $J^{(1)}$ (see Fig. 10) is clearly seen with nearly constant values of $J^{(1)}$ and β_2 at $N = 138 - 160$, followed by a pronounced drop of both for $N \geq 160$.

The situation is more complicated in the $N = 152$ isotones, where the change of $J^{(1)}$ as a function of proton number does not correlate with β_2 . While β_2 is almost constant for $90 \leq Z \leq 110$ (see Fig. 13), $J^{(1)}$ shows a maximum at $Z = 96$ and a minimum at $Z = 108$ (see Fig. 12).

By comparing the different RMF parametrizations, one can see that the sets which produce a smaller quadrupole deformation also produce a smaller moment of inertia. NL1 and NL-Z give very similar $J^{(1)}$. The same holds for NL3 and NL-RA1, whereas NLSH provides smaller values of $J^{(1)}$. It can also be seen that differences in the underlying single-particle spectrum (see Sect. VI) do not lead to significant modifications of the moments of inertia. This suggests that many orbitals contribute to the angular momentum.

F. Summary for Section III

In general, the moments of inertia for the heaviest nuclei are well described by the CRHB+LN theory. However, it was necessary to reduce the strength of the D1S Gogny force in the pairing channel by $\approx 12\%$, whereas in lighter nuclei with $A \approx 70 - 190$, the moments of inertia are well reproduced with a full strength D1S force. This points to a somewhat different A -dependence of the pairing strength than given by the Gogny force. The trends around $A \sim 250$ with respect to neutron or proton numbers are reasonably well reproduced. The calculations with and without pairing indicate very weak dependence (within $\approx 5\%$) of the moments of inertia on the parametrization of the RMF Lagrangian. The moments of inertia in this mass region are highly collective. Since many single-particle orbitals contribute, they are insensitive to fine details of the single-particle states. On the other hand, deformed shell gaps affect moments of inertia to some extend leading to a larger values.

IV. DEFORMATIONS

A. Comparison with experiment

Direct experimental information on the deformations of nuclei from Coulomb excitation and lifetime measurements is quite limited [73]. An alternative method is to derive a quadrupole moment from the $2^+ \rightarrow 0^+$ transition energy by employing the relation given by Grodzins [74] or by later refinements [73,75]. The prescription of Ref. [75] has an accuracy of about 10%. In Figs. 13, 14 and 15, the results of the CRHB+LN calculations are compared with deformations extracted by this method. From the calculated and experimental charge quadrupole moments Q , we derive the deformation parameters β_2 by the relation

$$Q = \sqrt{\frac{16\pi}{5}} \frac{3}{4\pi} Z R_0^2 \beta_2, \quad \text{where} \quad R_0 = 1.2 A^{1/3}. \quad (14)$$

The simple linear expression is used to maintain consistency with earlier papers [73]. It is sufficient for comparison between calculations and experiment because the same relation is used. Including higher powers of β_2 , e. g. as in Ref. [76], yields values of β_2 that are $\approx 10\%$ lower.

Figures 13, 14 and 15 demonstrate that the values of β_2 obtained from the $2^+ \rightarrow 0^+$ transition energies with the prescription of Ref. [75] are consistent with those from Coulomb excitation measurements. The CRHB+LN calculations with the NL3, NL-RA1, NL1, and NL-Z parametrizations agree rather well with these values. Considering the uncertainties on the extracted values of β_2 and the limited experimental data, it is difficult to give any preference for a particular set. Only NLSH seems to systematically underestimate β_2 .

B. General trends

Figures 13 and 14 illustrate the general trends of deformation as functions of proton and neutron numbers for the $N = 152$ isotones and for the Fm ($Z = 100$) isotopes. In the Fm chain, β_2 increases gradually from $N = 138$ up to $N \approx 150$ for all parametrizations except NLSH, which gives a slight decrease around $N = 140$. For $N \geq 150$, there is a gradual decrease of the β_2 values, which becomes more rapid above $N \approx 160$. These trends are more pronounced with NL3, NLSH and NL-RA1, which have been fitted to the data on neutron-rich nuclei as well. The variations are more gradual in the NL1 parametrization, which was obtained by fit to data from the beta-stability valley. The mass hexadecapole moments Q_{40} are similar for all parametrizations and decrease with increasing neutron number. While the changes of the slope of β_2 as a function of neutron number (see Fig. 14a) correlate with the shell gaps at $N = 148, 150$ and $N = 160, 162$ (Sect. V), no such correlations are seen for the Q_{40} values (see Fig. 14b).

The β_2 and Q_{40} values change more gradually with proton number Z in the $N = 152$ chain (see Fig. 13). The β_2 values are almost constant as a function of proton number. The calculated mass hexadecapole moments Q_{40} show a sinusoid-like curve as a function of proton number, with a maximum at $Z \approx 94$ and a minimum at $Z \approx 106$.

We expect that the trends are similar in the chains adjacent to the Fm and $N = 152$ chains, which is corroborated by the less systematic calculations for the Cm, Cf and No

isotopes (see Fig. 15). The equilibrium deformations are very similar for NL3 and NL-RA1 on the one hand, and for NL1 and NL-Z on the other hand. For this reason, the results obtained with NL-RA1 and NL-Z are omitted in Figs. 13, 14 and 15. The calculated β_2 increases as the parametrization changes from NL-SH to NL3 to NL1. This trend has previously been seen in the $A \sim 60, 150$, and 190 regions of superdeformation [30,57,59].

C. Summary for Section IV

In summary, the CRHB+LN theory with the NL3, NL1, NL-RA1 and NL-Z parameter sets satisfactorily reproduces the magnitude of the β_2 deformation of the heaviest nuclei, where they have been measured, whereas NLSH systematically underestimates it.

V. SHELL STRUCTURE

The stability of the superheavy elements is due to a region of low level density in the single-particle spectrum. For deformed nuclei all single-particle states are two-fold degenerate, and, thus, the region of low level density generally correlates with the 'shell gap'. The situation is more complicated in spherical nuclei, where the shell correction energy depends not only on the size of the shell gap, but also on the degeneracy of single-particle states in the vicinity of the Fermi level [77,78]. It is a concern of this paper to study how well the different RMF parametrizations reproduce the shell gaps in the heavy deformed elements. A simple intuitive measure for the level density at the Fermi surface is the distance E_{SP-GAP} between the last occupied and the first empty levels. Another way is to consider the two-neutron $S_{2n}(Z, N)$ and two-proton $S_{2p}(Z, N)$ separation energies

$$\begin{aligned} S_{2n}(Z, N) &= B(Z, N) - B(Z, N - 2) \\ S_{2p}(Z, N) &= B(Z, N) - B(Z - 2, N), \end{aligned} \quad (15)$$

where $B(N, Z)$ is the binding energy. The separation energies show a sudden drop at the shell gaps, if they are large. If the variations of the level density are less pronounced, the quantity $\delta_{2n}(Z, N)$ related to the derivative of the separation energy is a more sensitive indicator of the localization of the shell gaps. For the neutrons (and similarly for the protons) it is defined as

$$\begin{aligned} \delta_{2n}(Z, N) &= S_{2n}(Z, N) - S_{2n}(Z, N + 2) = \\ &= -B(Z, N - 2) + 2B(Z, N) - B(Z, N + 2). \end{aligned} \quad (16)$$

We show in Appendix A that variations (but not their absolute values) of $\delta_{2n}(Z, N)$ and E_{SP-GAP} agree rather well.

In this section, we study the shell structure along both the Fm ($Z = 100$) and the $N = 152$ chains.

A. Shell structure along the $Z = 100$ line

The results for two-neutron separation energies $S_{2n}(Z, N)$ in the Fm ($Z = 100$) chain with different RMF parametrizations are shown in Fig. 16. There is a systematic difference between the NL1, NL-Z sets and the NL3, NLSH, NL-RA1 sets. The former underestimate two-neutron separation energies, thus revealing their weakness in the description of isotopic trends. NL-Z is somewhat better as compared with NL1. Considering that these two sets are fitted to the same data, this result together with the one shown in Fig. 2 of Ref. [52] possibly indicate the importance of a more microscopic treatment of the center-of-mass correction for the reproduction of isotopic trends. On the other hand, NL3, NLSH and NL-RA1 better reproduce the experimental $S_{2n}(Z, N)$ values (see Fig. 16) indicating that the isovector component of the interaction has been treated more carefully in these sets.

The latter sets reasonably describe $S_{2n}(Z, N)$ for $144 \leq N \leq 148$ and $154 \leq N \leq 159$, but underestimate $S_{2n}(Z, N)$ for $N = 150, 152$. The shoulder in experimental $S_{2n}(Z, N)$ values at $N = 152$ reveals a deformed shell gap [79], which is better seen in the plot of $\delta_{2n}(Z, N)$ (Fig. 17a). The size of this gap depends sensitively on proton number. As seen in Fig. 17, there are discrepancies with experiment: NL3 and NL-RA1 (NL1 and NL-Z) produce a gap at $N = 148$ ($N = 148, 150$) instead of at $N = 152$ and NLSH does not show a clear gap (see also Figs. 3 and 19). The analysis of the neutron quasi-particle spectra in $^{249,251}\text{Cf}$ (see Sect. VID) also indicates that the calculated shell gaps do not correspond to the experimental ones.

Earlier calculations predicted the presence of a deformed neutron shell gap at $N = 162$ in superheavy nuclei (see, for example, Refs. [14,28] and references quoted therein). The presence of this gap in nuclei with $Z \approx 108$ was confirmed by recent experimental information [10,12]. The appearance of this gap and its size strongly depend on the parametrization of the specific theory and on the proton number. For example, in the Skyrme Hartree-Fock calculations [28], this gap is pronounced in the SkI3 parametrization, where it is seen over the proton range of $Z = 98 - 116$, but is absent in the SkP parametrization. This gap is clearly seen in RMF calculations with the NL3 and PL-40 parametrizations [28] but only at proton numbers around $Z = 106$. The present CRHB+LN calculations in the Fm chain indicate a gap at $N = 162$ for NL3 and at $N = 160$ for NL1, NL-Z and NL-RA1 (see Fig. 17). However, the small value of $\delta_{2n}(Z, N) \approx 0.8$ MeV suggests a small gap.

B. Shell structure along the $N = 152$ line

To judge the reliability of predictions of superheavy nuclei, it is critical to see how different RMF parametrizations are able to describe the experimental shell gaps as a function of proton number. The calculations for the $N = 152$ isotones are compared with experimental data in Figs. 20 and 21. As for the two-neutron separation energies, one can see that the two-proton separation energies $S_{2p}(Z, N)$ are best described by NL3, NLSH, NL-RA1. In contrast, the $S_{2p}(Z, N)$ values are overestimated by NL1 and NL-Z, which were obtained by fit to stable nuclei. The $S_{2p}(Z, N)$ plots do not show clearly where the proton deformed gaps are located, which becomes visible in the $\delta_{2p}(Z, N)$ plots. The experimental data show a shell gap at $Z = 100$. Only NLSH describes the position of this gap and the $\delta_{2p}(Z, N)$ values agree very well. However, the analysis of the quasi-particle spectra in Sect. VI G

reveals that this gap lies between the wrong bunches of single-particle states. Calculations with NLSH also indicate a gap at $Z = 108$, which has not been observed so far. NL-RA1 does not show any deformed gap for $92 \leq Z \leq 108$ (see Fig. 21). NL3, NL1 and NL-Z give a shell gap at $Z = 104$, in contradiction with experiment. The analysis of the proton quasi-particle spectra in ^{249}Bk (see Sect. VI E) leads to the same conclusion.

Many effective interactions not specifically fitted to the actinide region encounter similar problems. For example, most of the Skyrme forces fail to reproduce the deformed $Z = 100$ shell gap in the $N = 152$ isotones (see Fig. 5 in Ref. [28]). SkI4 is the only force which shows this gap. The SkI3, SkI1 and Sly6 forces show a $Z = 104$ shell gap, while the SkM* and SkP forces do not show any gap at $Z = 100 - 104$.

C. Pairing along the $Z = 100$ and $N = 152$ lines

Figure 9 shows the pairing energies E_{pairing} (see Eq. (11)) obtained with NL1 and NL3 as a function of neutron number along the $Z = 100$ line and as a function of proton number along the $N = 152$ line. The general trend as a function of nucleon number is the same for both sets.

Let us first discuss the $Z = 100$ line. In both RMF parametrizations, neutron pairing correlations are weakest at $N \approx 148$, reflecting the presence of a shell gap at $N = 148$ in the NL3 parametrization and somewhat smaller gaps at $N = 148$ and $N = 150$ in the NL1 parametrization (see Fig. 3). Going away from these shell gaps, the neutron pairing energies increase in absolute value, reflecting the increasing level density (Fig. 19). The neutron pairing is weakened at $N \approx 160$ due to the presence of smaller shell gaps at $N = 160$ (NL1, see Sect. V A) and at $N = 162$ (NL3, see Fig. 19). The weakening of the neutron pairing at $N \approx 148$ and $N \approx 160$ is more pronounced in the NL3 parametrization as compared with NL1, reflecting larger shell gaps (see Fig. 3).

The proton pairing shows the same trend as the neutron pairing, but with much smoother changes in neutron number. In both parametrizations, proton pairing is smaller and stays relatively constant at $N = 138 - 150$, reflecting low and nearly constant level density below the Fermi level (see Figs. 2 and 22). For $N \geq 150$, the deformation modifications induced by changes in the neutron number increase the proton level density near the Fermi level (see Fig. 22), enhancing the proton pairing.

The pairing energies on the $N = 152$ line exhibit the same features as discussed above. Both in the neutron and proton subsystems they reflect the presence of the $Z = 104$ and $Z = 96$ shell gaps (see Figs. 2 and 9).

D. Summary for Section V

The experimental $\delta_{2n}(Z, N)$ quantity shows a distinct deformed shell gap at $N = 152$, which is quite pronounced for No and Fm nuclei and less so for Cm and Cf (see Fig. 18). For the Fm isotopes, the CRHB+LN calculations predict a deformed shell gap(s) at $N = 148$ (NL3 and NL-RA1) or at $N = 148, 150$ (NL1 and NL-Z); see Fig. 17. The NLSH parameterization does not give a clear gap. The experimental data for the $N = 152$ isotones show a shell gap at $Z = 100$; NL1, NL-Z and NL3 give a gap at $Z = 104$ and NL-RA1 no

gap at all. Only NLSH gives a gap at $Z = 100$; however, it lies between the wrong bunches of single-particle states (see Sect. VI). This demonstrates the fact that the usual analysis of shell structure, in terms of only $S_{2n}(Z, N)$ and/or $\delta_{2n}(Z, N)$, maybe insufficient to judge the quality of the parametrization.

VI. QUASI-PARTICLE STATES

The investigation of the single-particle states in the $A \sim 250$ deformed mass region can shed additional light on the reliability of the RMF predictions of the energies of spherical subshells responsible for 'magic' numbers in superheavy nuclei. This is because several deformed single-particle states experimentally observed in odd nuclei of this mass region (see Table III) originate from these subshells. Considerable deviations between experiment and theory for a specific deformed state will indicate that the position of the spherical subshell from which this state originates is poorly described.

In the past, the RMF studies of single-particle spectra have been mostly performed in spherical or near-spherical nuclei (see, for example, Ref. [24] and references quoted therein), where a number of restrictions, such as the neglect of the currents or of the breaking of the Kramer's degeneracy, have been imposed in order to simplify the task. In addition, the BCS approximation was used. Moreover, a direct comparison between experimental and theoretical single-particle states in spherical nuclei should include the particle-vibration coupling, which can modify the single-particle energies considerably [27]. The modification of the quasiparticle states by particle-vibration coupling is weaker in deformed nuclei [84–86].

Not much is known about the accuracy of the description of the quasiparticle states in deformed nuclei within the framework of the RMF theory. In most cases the analysis of odd nuclei was based on the single-particle spectra calculated in neighboring even-even nuclei. To our best knowledge, a direct comparison between experimental and theoretical quasi-particle spectra has not been published.

The most detailed attempt to analyze the single-particle properties at finite deformation and their connections with those at spherical shape has been done within the cranked RMF theory in Ref. [59] for superdeformed (SD) bands in the $A \sim 150$ mass region. Although a direct comparison between experimental and calculated single-particle energies was not possible, some general conclusions were drawn based on a systematic analysis of experimental data and the expected response of specific single-particle states to a change of deformation. It was found that the RMF theory provides a reasonable description of the single-particle states in the vicinity of the SD shell gaps. However, some deviations between experiment and theory were detected, which could reach ≈ 1 MeV for some states. For example, the relative positions of the $\nu[651]1/2$ and $\nu[642]5/2$ states from the $\nu2g_{9/2}$ and $\nu1i_{13/2}$ spherical subshells are not reproduced. This problem exists in the NL1, NL3 and NLSH parametrizations of the RMF Lagrangian.

A. Computational details

In the present manuscript, we address for the first time the question of a fully self-consistent description of quasiparticle states in the framework of the RMF theory. A proper

description of odd nuclei implies the loss of the time-reversal symmetry of the mean-field, which is broken by the unpaired nucleon. The BCS approximation has to be replaced by the Hartree-(Fock-)Bogoliubov method, with time-odd mean fields taken into account. The breaking of time-reversal symmetry leads to the loss of the double degeneracy (Kramer's degeneracy) of the quasiparticle states. This requires the use of the signature or simplex basis in numerical calculations, thus doubling the computing task. Furthermore, the breaking of the time-reversal symmetry leads to nucleonic currents, which cause the *nuclear magnetism* discussed in Sect. II A.

The CRHB(+LN) theory takes all these effects into account. Thus, the effects of blocking due to odd particle are included in a fully self-consistent way. The CRHB computer code is set up in a signature basis and in three-dimensional Cartesian coordinates. The latter allows one to study also the γ -deformation. In order to specify the detailed structure of blocked orbitals, the existing CRHB code [30] has been extended to describe odd and odd-odd nuclei. The blocking procedure is implemented according to Refs. [26,87,88]. The blocked orbital can be specified either by its dominant main oscillator quantum number N or by the dominant Ω quantum number (Ω is the projection of the total angular momentum on the symmetry axis) of the wave function, or by combination of both. In addition, it can be specified by the particle or hole nature of the blocked orbital. Note that Ω is not a conserved quantum number in the CRHB code. As a consequence, convergence problems, emerging from the interaction of the blocked orbital with others, appear somewhat more frequently than in a computer code restricted to axial symmetry. Convergence problems appear more frequently when approximate particle number projection by means of the Lipkin-Nogami method is imposed, which is most likely due to additional non-linearities.

As illustrated in Fig. 23, the quasi-particle spectra calculated within the CRHB+LN (with LN) framework and using the scaled D1S Gogny force given in Table I are very similar to those obtained by means of the CRHB (without LN) with the original D1S force. The difference in the energies of the quasi-particle states is typically less than 150 keV and the level ordering is the same. Thus in order to avoid the convergence problems in the calculations with LN, all other calculations of quasi-particle states were performed in the CRHB framework with the original D1S force.

B. Particle-vibration coupling and other effects

Figures 23, 24 and 25 show that the calculated quasiparticle spectra are less dense than in experiment. The average level density of the single-particle states is related to the effective mass (Lorentz mass in the notation of Ref. [90] for the case of RMF theory) of the nucleons at the Fermi surface $m^*(k_F)/m$. The RMF theory gives a low effective mass $m^*(k_F)/m \approx 0.66$ [17]. The experimental density of the quasiparticle levels corresponds to an effective mass $m^*(k_F)/m$ close to one. This discrepancy appears also for non-relativistic mean-field models [23]. It has been demonstrated for spherical nuclei that the particle-vibration coupling brings the average level density in closer agreement with experiment [27], which means $m^*(k_F)/m$ closer to one. In a similar way, the particle-vibration coupling leads to a compression of the quasi-particle spectra in deformed nuclei [86]. The surface vibrations are less collective in deformed nuclei than in spherical ones because they are more fragmented [84,91]. As a consequence, the corrections to the energies of quasiparticle states

in odd nuclei due to particle-vibration coupling are less state-dependent in deformed nuclei. Hence the comparison between experimental and mean field single-particle states is less ambiguous in deformed nuclei as compared with spherical ones [27,91], at least at low excitation energies, where vibrational admixtures in the wave functions are small. Calculations within the quasiparticle-phonon model [92,93] indicate that in the $A \sim 250$ mass region the lowest states have mainly quasi-particle nature and the corrections to their energies due to particle-vibration coupling are typically at the level of 150 keV or less. The states above ≈ 700 keV contain very large vibrational admixtures [86] and thus experimental states above this energy should not be compared with the pure quasiparticle states obtained in the CRHB calculations.

Since particle-vibration coupling is not included, it is important to estimate how large is the discrepancy between calculated and experimental quasiparticle energies due to the low effective mass $m^*(k_F)/m$ of the RMF theory. Assuming for an estimate that the effective mass just stretches the energy scale, the difference between the energies of quasiparticle states obtained in the calculations with $\frac{m^*(k_F)}{m}$ and $\frac{m^*(k_F)}{m} = 1$ is

$$\Delta E_{qp} = E_{qp} \left(\frac{m^*(k_F)}{m} \right) \left(1 - \frac{m^*(k_F)}{m} \right), \quad (17)$$

which remains below ~ 200 keV as long as the calculated state is located in the energy window of 700 keV with respect to the Fermi surface, whereas it grows for higher excitation energies.

We are mostly interested in how well the positions of spherical subshells are described in the RMF calculations. One may reduce the error by comparing the experimental and calculated averages of two (or more) deformed single-particle states emerging from the same spherical subshell. The average of deformed states has the same energy when extrapolated to spherical shape as each of these states. The advantage is that the average of the states has smaller excitation energy than at least one of these states. As a result, the energy of the spherical subshell can be estimated more precisely (within 200 keV if $| (E_{qp,1} + E_{qp,2})/2 | \leq 700$ keV). Such an approach is especially useful when one of the states has particle ($E_{qp}^p > 0$) and the other hole ($E_{qp}^h < 0$) nature, since their average energy can be well within the 700 keV energy window even if the excitation energy of each is far outside this window.

An additional source of uncertainty is the Coriolis interaction between the quasi-particle states, which is neglected. It is relatively modest, affecting the energies of quasi-particle states by at most 100 – 200 keV [63,94]. As a whole, the uncertainty of our estimate for the spherical subshell energies in Sects. VI E and VID is around 300 keV.

C. General observations

Figures 2 and 3, where the single-particle states in ^{254}No are shown for different parametrizations, reveal important trends. The energies of some single-particle states depend strongly on the parametrization. For example, for $\pi[521]3/2$ and $\pi[521]1/2$ ², the

²These states are of special interest since they originate from the spin-orbit partner spherical subshells $\pi 2f_{7/2}$ and $\pi 2f_{5/2}$, which define the size and the position of the magic spherical proton

single-particle energies calculated with NL1 and NLSH differ by ≈ 2 MeV. The small differences in the self-consistent deformations cannot explain the differences in the single-particle energies.

Another observation is that the relative energies of the different Ω states, which emerge from the same spherical subshell, almost do not depend on the parametrization. For protons, these are, for example, the $\pi[642]5/2$, $\pi[633]7/2$, $\pi[624]9/2$ states from the $\pi 1i_{13/2}$ spherical subshell and the $\pi[514]7/2$, $\pi[505]9/2$ states from the $\pi 1h_{9/2}$ subshell. This is expected because the splitting of different Ω states from the same spherical subshell is a consequence of the deformation of the mean field, which is not very sensitive to the parametrization (see Sect. IV). On the other hand, the single-particle energies of the $\pi 2f_{7/2}$ and $\pi 2f_{5/2}$ spherical subshells (but not their splitting), as well as the deformed states emerging from them, change considerably when going from the NL1 to the NLSH parametrization (see Fig. 20 in Ref. [59] and Fig. 2 in the present manuscript for their deformed counterparts). This leads to a $Z = 104$ deformed shell gap in the NL1 and NL-Z parametrizations and a $Z = 100$ gap in the NLSH parametrization.

The situation is analogous for the neutron states (see Fig. 3). For example, the relative energies of the $\nu[624]7/2$, $\nu[615]9/2$ and $\nu[606]11/2$ states, emerging from the $\nu 1i_{11/2}$ spherical subshell, almost do not depend on the RMF parametrization. The same is true for relative energies of the states $\nu[743]7/2$, $\nu[734]9/2$ and $\nu[725]11/2$, emerging from the $\nu 1j_{15/2}$ subshell, and the states $\nu[761]1/2^*$ and $\nu[752]3/2^*$ from the $\nu 1j_{13/2}$ subshell. It is interesting that the relative energies of the states $\nu[631]1/2$ ($\nu 2g_{7/2}$), $\nu[622]5/2$ ($\nu 2g_{9/2}$), $\nu[622]3/2$ ($\nu 2g_{7/2}$), $\nu[620]1/2$ ($\nu 3d_{5/2}$), $\nu[613]7/2$ ($\nu 2g_{9/2}$) and $\nu[613]5/2$ ($\nu 2g_{7/2}$), originating from the different spherical subshells shown in parenthesis after the Nilsson labels, are almost independent on the RMF parametrization. This indicates that the relative energies of the $\nu 2g_{9/2}$, $\nu 2g_{7/2}$ and $\nu 3d_{5/2}$ spherical subshells only marginally depend on the RMF parametrization, which is clearly seen in the single-particle spectra of spherical nuclei (see Fig. 20 in Ref. [59] and Fig. 1 in Ref. [17] for spectra of ^{208}Pb and Figs. 4, 9 and 15 in Ref. [17] for spectra of superheavy nuclei). On the other hand, the increase of the separation between the $\nu[761]1/2^*$ and $\nu[750]1/2^*$ states when going on from the NL1 to the NLSH parametrizations shows that the separation between the $\nu 1j_{13/2}$ and $\nu 2h_{11/2}$ spherical subshells increases.

In a previous study in the $A \sim 150$ mass region of superdeformation [59], we also concluded that the dependence of the single-particle energies of deformed states on the RMF parametrizations reflect their energy displacement at spherical shape. Since different RMF sets give similar spin-orbit splittings (see Fig. 2 in Ref. [17] and Fig. 2 for the splitting and position of the $\pi[521]3/2$ and $\pi[521]1/2$ states), the dominant modification is a shift of the position of the l -shells.

There are similarities between the single-particle spectra (see Figs. 2 and 3) obtained with the NL1 and NL-Z parametrizations, on the one hand, and NL3 and NL-RA1, on the

shell gap in superheavy nuclei [17]. Their splitting, defined primarily by the spin-orbit splitting and their response to deformation, almost does not depend on the RMF parametrization. In part, this is due to the fact that their interaction with other orbitals is rather weak (see, for example, the Nilsson diagram (Fig. 4) in Ref. [79]).

other hand. Thus detailed study of quasi-particle spectra will be performed with only the NL1 and NL3 parametrizations. They can be considered as representative examples of the two groups of RMF parametrizations discussed in Sect. II B.

D. Odd-neutron nuclei $^{249,251}\text{Cf}$

The quasiparticle spectra of these two nuclei with neutron numbers $N = 151, 153$ are presented in Figs. 23 and 24. The ground state configuration of ^{249}Cf is correctly reproduced in both parametrizations. Only NL1 gives the correct ground state $\nu[620]1/2$ in ^{251}Cf , whereas NL3 gives the $\nu[615]9/2$.

The $\nu[622]5/2$ and $\nu[613]7/2$ (and $\nu[604]9/2$ in ^{251}Cf) states emerge from the $\nu 2g_{9/2}$ spherical subshell. The $\nu[622]5/2$ energy is reproduced within 300 keV in both nuclei by both parametrizations. However, in both nuclei the excitation energy of the $\nu[613]7/2$ state is overestimated by ≈ 0.55 MeV and by ≈ 1.0 MeV in the NL1 and NL3 parametrizations, respectively. The comparison of the average energies of the experimental and calculated $\nu[613]7/2$ and $\nu[622]5/2$ states suggests that the energy of the $\nu 2g_{9/2}$ subshell has to be decreased by ≈ 0.15 MeV and by ≈ 0.6 MeV in the NL1 and NL3 parametrizations, respectively.

The relative position of the $\nu[613]7/2$ and $\nu[615]9/2$ states, emerging from the $\nu 2g_{9/2}$ and $\nu 1i_{11/2}$ spherical subshells, is not reproduced in both parametrizations. In addition, the excitation energy of the $\nu[624]7/2$ state from the $\nu 1i_{11/2}$ subshell is overestimated by ≥ 1 MeV in ^{249}Cf (see Fig. 23). An analysis similar to the one given above suggests that the energy of the $\nu 1i_{11/2}$ spherical subshell has to be increased by ≈ 0.3 MeV and by ≈ 1 MeV in the NL1 and NL3 parametrizations, respectively, in order to bring the calculations in agreement with experiment.

In ^{251}Cf , the relative positions of the $\nu[622]3/2$ ($\nu 2g_{7/2}$) and $\nu[620]1/2$ ($\nu 3d_{5/2}$) states (see Fig. 24) differ in experiment and calculations (with NL3). In addition, NL3 fails to reproduce the $\nu[620]1/2$ energy. The states $\nu[622]3/2$ and $\nu[620]1/2$ are almost degenerate in energy in the NL1 parametrization, while in experiment the excitation energy difference between the $\nu[622]3/2$ and $\nu[620]1/2$ states is 178 keV. An increase (decrease) of the energy of the $\nu 2g_{7/2}$ spherical subshell by ≈ 0.15 MeV in NL1 (NL3) and a decrease of the energy of the $\nu 3d_{5/2}$ spherical shell by ≈ 0.5 MeV in the NL3 parametrization would remove these discrepancies.

In addition, the $\nu[761]1/2^*$ ³ state has been observed in ^{251}Cf . Its quasiparticle energy is well described (within 150-200 keV) in both parametrizations, suggesting that the energy of the $\nu 1j_{13/2}$ spherical subshell is correctly accounted for in both parametrizations.

The comparison of the average energies of the experimental and calculated $\nu[734]9/2$ and $\nu[725]11/2$ states in ^{251}Cf (see Fig. 24), from the $\nu 1j_{15/2}$ subshell, suggests that the energy of this subshell has to be decreased by ≈ 0.7 MeV and by ≈ 0.45 MeV in the NL1 and NL3 parametrizations, respectively. However, the $\nu[734]9/2$ state would still remain the ground state of ^{249}Cf after all the modifications discussed above.

³The use of asterisk at the Nilsson labels is explained in caption of Fig. 2.

E. Odd-proton nucleus ^{249}Bk

The quasiparticle spectrum of ^{249}Bk ($Z = 98, N = 152$) is presented in Fig. 25. Three states $\pi[642]5/2$, $\pi[633]7/2$ and $\pi[624]9/2$, from the $\pi 1i_{13/2}$ subshell, have been observed in experiment. We select this subshell as a reference, with respect to which the positions of other spherical subshells will be compared, because in the NL1 and NL3 parametrizations the $\pi[633]7/2$ state is close to experiment, and the $\pi[642]5/2$ and $\pi[624]9/2$ states are located below and above the Fermi level, respectively. The $\pi[642]5/2$ and $\pi[633]7/2$ states are reasonably well reproduced. The $\pi[624]9/2$ state is excluded from the direct comparison since vibrational admixtures are expected to be large due to high experimental excitation energy of this state.

The energy difference between the $\pi[521]3/2$ and $\pi[521]1/2$ states is well reproduced, suggesting that the spin-orbit splitting between the $\pi f_{5/2}$ and $\pi f_{7/2}$ spherical subshells is correctly described. However, their positions with respect to the Fermi level depend on the parametrization: for only NL1 is the $\pi[521]3/2$ state lowest in energy, in agreement with experiment. The energy difference between the $[633]7/2$ and $[521]3/2$ states is small, around 250 keV (see Fig. 25). A decrease (increase) of the energy of the $2f_{7/2}$ spherical subshells by ≈ 0.25 MeV in the NL3 (NL1) parametrizations would bring the relative positions of these states in agreement with experiment. This also implies the same shift of its spin-orbit partner $\pi 2f_{5/2}$.

The $\pi[514]7/2$ state, from the $\pi 1h_{9/2}$ subshell, is too low in energy in both parametrizations with respect to the $\pi[633]7/2$ state. An increase of the energy of the $1h_{9/2}$ spherical subshell by ≈ 0.85 MeV for NL3 and by ≈ 0.6 MeV for NL1 would bring calculations in agreement with experiment. The analyses of odd-proton nuclei around ^{208}Pb (see Fig. 7 in Ref. [24]) and of shape coexistence in the Pt-Hg-Pb isotopes [95] also point to this deficiency in the description of the $1h_{9/2}$ spherical subshell energy.

The calculations underestimate the position of the $\pi[530]1/2$ state, from the $\pi 2f_{7/2}$ subshell, by ≈ 1.5 MeV. If the energy of the $1h_{9/2}$ subshell were increased as discussed above, this would push the $\pi[530]1/2$ state closer to the Fermi level due to the interaction with the $\pi[541]1/2$ state, from the $\pi 1h_{9/2}$ subshell (see Fig. 4 in Ref. [79]). This would lead to a better agreement between calculations and experiment.

The $\pi[400]1/2$ state, from the $\pi 3s_{1/2}$ subshell, is also reasonably well reproduced (somewhat better with NL3 than with NL1). However, the relative positions of the $\pi[400]1/2$ and $\pi[642]5/2$ states (the latter from the $\pi 1i_{13/2}$ subshell) suggest that the energy of the $\pi 3s_{1/2}$ subshell has to be increased by ≈ 0.3 MeV in the NL1 parametrization.

F. Consequences for deformed shell gaps in the $A \sim 250$ mass region.

Figure 26 shows how the proton and neutron spectra in ^{254}No are modified if the spherical subshells are shifted as discussed in Sects. VI E and VI D. Similar corrected spectra are obtained with NL3 and NL1, indicating that the shifts are correctly defined. These shifts would lead to the deformed shell gaps at $N = 152$ and $Z = 100$, as seen in experiment (Sects. V A and V B). Neutron gaps at $N = 148, 150$ (NL1) ($N = 148$ in NL3) seen in uncorrected spectra disappear, while the proton gap at $Z = 104$ becomes smaller.

In addition, the ordering of the neutron and proton single-particle states below and above these shell gaps would be more similar to the Woods-Saxon potential (see Fig. 8 in Ref. [96]), whose parameters were defined by an overall fit to the single-particle spectra in heavy actinide nuclei [97].

These examples illustrate that in the region of high level density and small shells gaps, a shift of the energies of one or two single-particle states by a modest energy of 0.5 MeV can modify the nucleon number of the shell gap by two or four units. A new parametrization of the RMF Lagrangian, which implements the shifts discussed in Sects. VI E and VI D naturally, is called for.

G. Estimates for other parametrizations

The calculations of odd- A nuclei performed with the NL1 and NL3 sets indicate that, in general, the results are quite similar but somewhat better agreement is obtained in the NL1 parametrization. Moreover, some conclusions about the accuracy of the description of the quasi-particle states in other RMF parametrizations can be drawn with the aid of the spectra presented in Figs. 2 and 3. The NL-Z parametrization gives single-particle spectra in between those for NL1 and NL3 and, thus, a similar accuracy of the description of quasi-particle states is expected.

The agreement with experiment is worse for the NLSH and NL-RA1 parametrizations. Let us illustrate this by a few examples for NLSH, which deviate most from experiment. The energy splitting between $\nu[613]7/2$ and $\nu[615]9/2$ increases from ≈ 0.5 MeV up to ≈ 2.5 MeV when going from NL1 to NLSH (see Fig. 3). Thus in order to reproduce the relative positions of these states in $^{249,251}\text{Cf}$ (see Figs. 23 and 24), the relative distance between the spherical $\nu 2g_{9/2}$ and $\nu 1i_{11/2}$ subshells should be corrected by roughly 2 MeV.

The Fermi level for the odd-proton ($Z=97$) ^{249}Bk nucleus will be located somewhere in the vicinity of the $\pi[633]7/2$ and $\pi[514]7/2$ states (see Fig. 3). Thus, the $\pi[521]3/2$ and $\pi[521]1/2$ states (and the corresponding $\pi 2f_{7/2}$ and $\pi 2f_{5/2}$ spherical subshells) should be lowered by roughly 1 MeV with respect of the $\pi[633]7/2$ state (the $\pi 1i_{13/2}$ subshell) in order to reproduce the experimental spectra (see Fig. 25). In addition, the position of the $\pi[514]7/2$ state ($\pi 1h_{9/2}$ spherical subshell) should be raised by ≈ 700 keV with respect of the $\pi[633]7/2$ state (the $\pi 1i_{13/2}$ subshell).

Thus the empirical shifts required to reproduce experimental quasiparticle energies are much larger for NLSH than the ones needed for NL1 and NL3 (see Sects. VI D and VI E). Only after these shifts will the $\pi[633]7/2$ and $\pi[521]3/2$ states be located in the vicinity of the proton Fermi level and there will be a gap at $Z = 100$ between these states and $\pi[521]1/2$ and $\pi[514]7/2$ in agreement with an analysis based on the Woods-Saxon potential [96]. Although the NLSH parametrization is the only one parametrization which reproduces the $Z = 100$ gap (see Fig. 21), this gap is created between the wrong bunches of states.

H. Consequences of nuclear magnetism for quasiparticle states

The influence of nuclear magnetism on the binding energies of one-quasiparticle states in ^{249}Cf and ^{249}Bk is shown in Table IV. In all cases, it provides small additional binding.

It is state dependent and lies between -16 and -69 keV, depending weakly on the strength of the pair correlations and on particle number projection. This indicates that these heavy nuclei are rather robust against polarization effects induced by nuclear magnetism. Thus, if nuclear magnetism was neglected, the quasiparticle spectra in this mass region would only be marginally modified. The influence of nuclear magnetism on quasiparticle energies is larger in lighter systems [45] (see also Ref. [98] for a study of the effects of the time-odd mean fields on the quasiparticle energies within the Skyrme Hartree-Fock approach) and in two-particle configurations [99].

While the neglect of nuclear magnetism seems to be a reasonable approximation for the one-quasiparticle energies, it has to be taken into account when the strength of the pairing correlations is fitted to experimental odd-even mass differences because it modifies $\Delta^{(3)}$ by $\approx 10\%$ (see Table II).

I. Implications for the study of superheavy nuclei

In the NL1 and NL3 parametrizations, the energies of the spherical subshells, from which the deformed states in the vicinity of the Fermi level of the $A \sim 250$ nuclei emerge, are described with an accuracy better than 0.5 MeV for most of the subshells (see Figs. 27 and 28 where required corrections for single-particle energies are indicated). The discrepancy reaches 0.6-1.0 MeV for the $\pi 1h_{9/2}$ (NL3, NL1), $\nu 1i_{11/2}$ (NL3), $\nu 1j_{15/2}$ (NL1) and $\nu 2g_{9/2}$ (NL3) spherical subshells. Considering that the RMF parametrizations were fitted only to bulk properties of spherical nuclei, this level of agreement is good. However, the accuracy of the description of single-particle states is unsatisfactory in the NLSH and NL-RA1 parametrizations (see Sect. VI G).

The single-particle levels of spherical magic superheavy nuclei are not modified much with the empirical shifts of Sects. VI E and VI D (see Figs. 27 and 28 for the calculated and corrected single-particle spectra of a $^{292}_{172}120$ nucleus). This conclusion relies on the assumption that the shifts should be similar in the deformed $A \sim 250$ mass region and in superheavy nuclei. The corrected spectra from the NL1 and NL3 calculations are very similar, with minor differences coming from the limited amount of information on quasiparticle states used in the analysis. More systematic study of quasiparticle states in deformed nuclei are required to determine these corrections more precisely.

Let us consider the calculations for the nucleus with $Z = 120$, $N = 172$. The corrected single-particle levels still suggest that $N = 172$ and $N = 184$ are candidates for magic neutron numbers in superheavy nuclei. The position of the $\nu 4s_{1/2}$ spherical subshell and the spin-orbit splitting of the $3d_{5/2}$ and $3d_{3/2}$ subshells will decide which of these numbers (or both of them) is (are) actually magic. The corrected proton levels indicate that the $Z = 120$ gap is large whereas the $Z = 114$ gap is small. Hence, on the basis of the present investigation we predict that $Z = 120$ is the magic proton number. This conclusion is based on the assumption that the NL1 and NL3 sets predict the position of the $\pi 1i_{11/2}$ and $\pi 3p_{1/2,3/2}$ subshells within 1 MeV. The positions of $\pi 1j_{15/2}$ and $\pi 2g_{9/2}$ seems less critical, because they are located well above this group of states both in Skyrme and RMF calculations [17]. It seems possible to obtain information about the location of the $\pi 1i_{11/2}$ subshell, which may have been observed through its deformed state ($\pi[651]1/2^*$) in superdeformed rotational bands of Bi-isotopes [100,101]. An CRHB analysis may provide this critical information.

In this context it is important to mention that the RMF parametrizations, NL-SH and NL-RA1, which are the only ones to predict $Z = 114$ as the magic proton number [18,19], provide poor descriptions of the single-particle states (see Sect. VI G).

The Nilsson diagrams given, for example, in Figs. 3 and 4 of Ref. [79], suggest that spectroscopic studies of deformed odd nuclei with proton and neutron numbers up to $Z \approx 108$ and $N \approx 164$ may lead to observation of the deformed states with $\Omega = 1/2$, emerging from the $\pi 1i_{11/2}$ and $\pi 1j_{15/2}$ spherical subshells (located above the $Z = 120$ shell gap) and from $\nu 1k_{17/2}$ and either $\nu 2h_{11/2}$ or $\nu 1j_{13/2}$ subshells (located above the $N = 184$ shell gap). This will further constrain microscopic models and effective interactions.

No information on low- j states, such as $\pi 3p_{3/2}$, $\pi 3p_{1/2}$, $\nu 3d_{3/2}$ and $\nu 4s_{1/2}$, which decide whether $Z = 120$ or $Z = 126$ and $N = 172$ or $N = 184$ are magic numbers in microscopic theories (see Refs. [17,20] and references quoted therein), will come from the study of deformed nuclei (see Table III).

The measured and calculated energies of the single-particle states at normal deformation provide constraints on the spherical shell gaps of superheavy nuclei. In particular, the small splitting between the $\pi[521]1/2$ and $\pi[521]3/2$ deformed states, emerging from the $\pi 2f_{5/2}$ and $\pi 2f_{7/2}$ spherical subshells that straddle proton number 114, suggests that the $Z = 114$ shell gap is not large.

J. Concluding remarks to Section VI

In order to judge the reliability of the energies of single-particle states predicted for superheavy nuclei by self-consistent mean-field theories, it is necessary to check the theoretical energies against the experimental ones in the heaviest nuclei where data exist. The energies of quasiparticle states have been calculated in a fully self-consistent manner with the CRHB method for ^{249}Bk and $^{249,251}\text{Cf}$ and compared with experiment. The calculated single-particle energies depend on the Lagrangian parameterization; NL1, NL3 and NL-Z provide good descriptions of the measured energies, whereas NLSH and NL-RA1 do not. For the former set, the quasiparticle energies are generally reproduced for most orbitals within ≈ 500 keV. However, for some orbitals originating from a few specific spherical subshells, the discrepancy between theory and experiment can reach 1 MeV. Empirical shifts of the energies of these orbitals can be introduced to fit the experimental data. Including these shifts, the next spherical shell gaps beyond ^{208}Pb are predicted at $Z = 120$ and $N = 172, 184$; no gap is seen at $Z = 114$. The occurrence of some sizeable discrepancies in single-particle energies calls for an improved Lagrangian parametrization, which can better describe single-particle energies and, thereby, give more reliable predictions about the properties of superheavy nuclei.

VII. CONCLUSIONS

The cranked relativistic Hartree+Bogoliubov theory has been applied for a systematic study of the nuclei around ^{254}No , the heaviest elements for which detailed spectroscopic data are available. The deformations, rotational response, pair correlations, quasiparticle spectra, shell structure and the two-nucleon separation energies have been studied. The goal was to see how well the theory describes the experimental data and how this description depends

on the RMF parametrization. Although the relativistic mean field theory has been used extensively for the predictions of the properties of superheavy nuclei, it has not yet been demonstrated how well it describes spectroscopic data in the heaviest nuclei, which are the gateway to superheavy nuclei. The present investigation provides a basis for better judging the reliability of extrapolations to superheavy nuclei.

The calculations with the NL3, NL1, NL-RA1 and NL-Z parameter sets reproduce well the experimental quadrupole deformations of the Cm, Cf, Fm and No nuclei, whereas the NLSH set underestimate them.

In order to reproduce the moments of inertia in the $A \sim 250$ mass region, the strength of the D1S Gogny force in the particle-particle channel has to be attenuated by $\approx 12\%$. In contrast, the moments of inertia of lighter nuclei can be well described with the full strength D1S force.

With the attenuated D1S force, the rotational response is well described. In $^{252,254}\text{No}$ nuclei, the alignment of the proton $i_{13/2}$ ($\pi[633]7/2$) and neutron $j_{15/2}$ ($\nu[734]9/2$) pairs takes place simultaneously at $\Omega_x \approx 0.31$ MeV. While the crossing frequency depends only weakly on the RMF parametrization, the gain of aligned angular momentum at the band crossing and the sharpness of the band crossing are more sensitive to it. The moments of inertia at low spin in the Cm, Cf, Fm and No isotopes and their variations with nucleon number are reproduced.

The two-particle separation energies are best described by the NL3, NLSH and NL-RA1 parametrizations, which were derived by fitting experimental information on neutron-rich nuclei. The calculated deformed shell gaps occur at nucleon numbers which may deviate by as much as 4 from those observed in experiment.

The quasiparticle-states calculated for odd- A nuclei are the same as those identified in experiment. For many states, the difference between experimental and theoretical energies calculated with the NL1 and NL3 sets is less than 0.5 MeV, but may reach 1 MeV in some cases. The spectrum is less compressed in the calculations as compared with experiment, which reflects the low effective mass of the RMF theory. Inclusion of particle-vibration coupling may correct that. The agreement between experiment and theory can be considered quite good, considering that the 6 or 7 parameters of the RMF theory have been adjusted to the ground-state properties of spherical nuclei, without taking into account the experimental information on the single-particle states.

Concerning the predictions for superheavy nuclei we conclude the following.

(i) Among the investigated RMF sets, NL1, NL3 and NL-Z provide best description of single-particle states so they seem to be most promising for the study of superheavy nuclei. The corresponding self-consistent calculations predict as likely candidates for magic numbers $N = 172$ and $N = 184$ for neutrons and $Z = 120$ for protons. No significant shell gap is found for $Z = 114$. These conclusions take into account the possible shifts of spherical subshells that are suggested by the discrepancies between calculations and experiment found in our analysis of deformed odd-mass actinide nuclei.

(ii) NL-SH and NL-RA1, which are the only RMF sets predicting $Z = 114$ as a magic proton number, provide poor descriptions of single-particle states and thus are not considered as reliable for study of superheavy nuclei.

(iii) Experimental studies of deformed odd nuclei with proton and neutron numbers up to $Z \approx 108$ and $N \approx 164$ may lead to observation of the deformed states emerging from

the high- j spherical subshells located above $Z = 120$ and $N = 184$. Their observation will provide a crucial constraint on the magic numbers.

(iv) The study of deformed states will not provide access to a number of low- j subshells, which largely define whether $Z = 120$ or $Z = 126$ and $N = 172$ or $N = 184$ are magic numbers.

(v) More systematic studies of the splitting between the $\pi[521]1/2$ and $\pi[521]3/2$ deformed states, which originate from the $\pi 2f_{5/2}$ and $\pi 2f_{7/2}$ spherical subshells, may provide more stringent information on whether a shell gap exists at $Z = 114$.

The present results demonstrate the limitations of adjusting the RMF parameters only to the bulk properties of spherical nuclei and may point to missing components in the effective Lagrangian. A new fit to both the bulk and single-particle properties should lead to a more accurate theory.

Like many Hartree(-Fock) calculations based on effective interactions, the RMF theory underestimates the single-particle level density. This indicates that some important mechanism is missing, which may be the particle-vibration coupling.

VIII. ACKNOWLEDGMENTS

The authors would like to thank P. Ring, R. R. Chasman and A. Malov for valuable discussions. This work was supported in part by the U. S. Department of Energy, Grants No. W-31-109-ENG38 and DE-FG02-95ER40934. The numerical calculations were performed in part on the Cray PVP Cluster at the National Energy Research Scientific Computing Center.

IX. APPENDIX A: THE QUANTITY $\delta_{2N}(Z, N)$.

In order to understand the quantity $\delta_{2n}(Z, N)$ related to the second derivative of the binding energy as a function of nucleon number better, we first discuss the case when pairing is neglected. Then we perform a detailed analysis with pairing included in the CRHB+LN framework.

Figure 29 compares $\delta_{2n}(Z, N)$ obtained in the RMF calculations without pairing with $2E_{SP-GAP}$, where E_{SP-GAP} is the energy gap between the last occupied and the first unoccupied single-particle level in the (Z, N) system. One can see that $\delta_{2n}(Z, N)$ is shifted down by $0.56^{+0.12}_{-0.10}$ MeV with respect to $2E_{SP-GAP}$. This shift can be understood within the shell-correction method [63,102,103], in which the total energy of the system E_{tot} in the absence of pairing is given by

$$E_{tot} = E_{LD} + E_{sh}^\pi + E_{sh}^\nu \quad (18)$$

where E_{LD} is a liquid drop energy and E_{sh} is a shell energy (superscript ν stands for neutrons, π for protons). The latter is given by

$$E_{sh} = 2 \sum_{i-occ} e_i - 2 \int^{\tilde{\lambda}} e \tilde{g}(e) de = 2 \sum_{i-occ} e_i - \tilde{E} \quad (19)$$

where e is a single-particle energy, $\tilde{g}(e)$ the smeared level density and \tilde{E} the Strutinsky smoothed sum. In this equation λ is the Fermi energy corresponding to $\tilde{g}(e)$ and is determined from the condition of number conservation

$$N = 2 \int^{\lambda} \tilde{g}(e) de \quad (20)$$

Neglecting the variations in E_{sh}^{π} when the neutron number changes, one can write

$$\delta_{2n}(Z, N) = 2E_{SP-GAP} - \delta_{2n}^{\tilde{E}}(Z, N) + \delta_{2n}^{E_{LD}}(Z, N). \quad (21)$$

$E_{LD}(Z, N)$ and $\tilde{E}(Z, N)$ are smooth functions, which weakly depend on the particle number [63], and the $\delta_{2n}^{E_{LD}}(Z, N)$ and $\delta_{2n}^{\tilde{E}}(Z, N)$ quantities related to their second derivatives as a function of nucleon number are nearly constant within the considered interval. Hence, $\delta_{2n}(Z, N)$ differs from $2E_{SP-GAP}$ by nearly constant. Although the shell-correction method is an approximation to the fully variational many-body approach such as the RMF theory, it elucidates the main physics in a simple way. This example clearly shows that $\delta_{2n}(Z, N)$ is not a direct measure of $2E_{SP-GAP}$.

The pairing smoothes the variations of $\delta_{2n}(Z, N)$ because there is gradual change of occupation numbers from 1 to 0. Comparing Figs. 29 and 30 one sees that the pairing reduces the height of the maximum of $\delta_{2n}(Z, N)$ at the $N = 148$ shell gap by approximately a factor of two and increases $\delta_{2n}(Z, N)$ at the neutron numbers away from it. This illustrates that the values of $\delta_{2n}(Z, N)$ cannot be taken as direct measure of $2E_{SP-GAP}$ since they are strongly dependent on pairing; see also Ref. [104] and Fig. 17b for a comparison of the results of CRHB and CRHB+LN calculations.

Let us now consider the chain of the Fm isotopes within the CRHB+LN theory as an illustrative example how the $\delta_{2n}(Z, N)$ is built from different contributions. If we neglect the spurious center-of-mass correction, which in harmonic oscillator approximation does not contribute to $\delta_{2n}(Z, N)$, then the total energy in the laboratory frame is given by (see Eqs. (21-24,43) in Ref. [30] for details)

$$\begin{aligned} E = & -\frac{1}{2}g_{\sigma} \int d\mathbf{r} \sigma(\mathbf{r})\rho_s(\mathbf{r}) - \frac{1}{2}g_{\omega} \int d\mathbf{r} \omega_0(\mathbf{r})\rho_v^{is}(\mathbf{r}) \\ & -\frac{1}{2}g_{\sigma} \int d\mathbf{r} \left[\frac{1}{3}g_2\sigma^3(\mathbf{r}) + \frac{1}{2}g_3\sigma^4(\mathbf{r}) \right] \\ & -\frac{1}{2}g_{\rho} \int d\mathbf{r} \rho_0(\mathbf{r})\rho_v^{iv}(\mathbf{r}) \\ & -\frac{1}{2}e \int d\mathbf{r} A_0(\mathbf{r})\rho_v^p(\mathbf{r}) \\ & + Tr(h_D\rho) \\ & -\frac{1}{2}Tr(\Delta\kappa) \\ & -\lambda_2\langle(\Delta\hat{N})^2\rangle \end{aligned} \quad \left. \begin{array}{l} \{ = E_{S+V} \\ \{ = E_{\sigma NL} \\ \{ = E_{\rho} \\ \{ = E_{Coul} \\ \{ = E_{part} \\ \{ = E_{pairing} \\ \{ = E_{LN} \end{array} \right) \quad (22)$$

where first four terms represent the contributions from bosonic degrees of freedom, while last three terms from fermionic degrees of freedom. The E_{S+V} is the sum of the energies of the fields associated with the linear part of the σ -meson and the ω -meson. This sum represents the main part of the nucleonic potential [23,32]. The $E_{\sigma NL}$ term is the energy of the non-linear part of the σ -meson, while E_{ρ} is the energy of the ρ -meson field and the E_{Coul} is the energy of the Coulomb field. Finally, the E_{part} , $E_{pairing}$, E_{LN} terms are the particle and the

pairing energies as well as the energy correction entering into particle-number projection by means of the Lipkin-Nogami method, respectively.

Based on Eq. (22), one can express $\delta_{2n}(Z, N)$ as a sum of the contributions of different terms of the RMF Lagrangian

$$\begin{aligned}\delta_{2n}(Z, N) = & \delta_{2n}^{S+V}(Z, N) + \delta_{2n}^{\sigma NL}(Z, N) + \delta_{2n}^{\rho}(Z, N) + \delta_{2n}^{Coul}(Z, N) \\ & + \delta_{2n}^{part}(Z, N) + \delta_{2n}^{pairing}(Z, N) + \delta_{2n}^{LN}(Z, N).\end{aligned}\quad (23)$$

An analysis of these contributions to $\delta_{2n}(Z, N)$ is presented for the chain of the Fm isotopes in Fig. 30. The largest contributions to $\delta_{2n}(Z, N)$ come from the particle energies ($\delta_{2n}^{part}(Z, N)$) and from the main part of the nucleonic potential ($\delta_{2n}^{S+V}(Z, N)$). They are generally in opposite phase as a function of neutron number and thus they cancel each other to a large extent. It is interesting to see that the maximum (in absolute value) of these contributions is located at neutron number $N = 152$, while the large shell gap is seen in the single-neutron spectra at $N = 148$ (see Fig. 19). It is difficult to understand why the maximum of $\delta_{2n}^{part}(Z, N)$ and $\delta_{2n}^{S+V}(Z, N)$ does not correlate with the $N = 148$ shell gap, but a plausible reason is related to the trend of deformation changes. The calculated β_2 -deformation increases at neutron number $N = 138 - 148$, and then decreases at $N \geq 150$, see Fig. 14a.

The contributions to the $\delta_{2n}(Z, N)$ coming from the ρ -meson ($\delta_{2n}^{\rho}(Z, N)$), the non-linear self-coupling of the σ -meson ($\delta_{2n}^{\sigma NL}(Z, N)$), the Coulomb potential ($\delta_{2n}^{Coul}(Z, N)$) and the pairing interaction ($\delta_{2n}^{pairing}(Z, N)$) are non-negligible and at some particle numbers some of them are comparable with the size of the total $\delta_{2n}(Z, N)$.

It is interesting that total $\delta_{2n}(Z, N)$ can become negative, as seen in the Fm isotopes at $N = 168$ in the CRHB+LN calculations with the NL3 and NL-RA1 parametrizations; see Figs. 30b and f. This is a region of neutron numbers where the deformation changes are considerable; see Fig. 14. This result reflects their importance in the definition of $\delta_{2n}(Z, N)$ and again underlines the fact that many factors beyond the size of the shell gap contribute to $\delta_{2n}(Z, N)$. Since by definition the shell gap has to have positive value and because of the reasons mentioned above, it is clear that $\delta_{2n}(Z, N)$ cannot be a direct measure of the shell gap.

However, this quantity, being related to the second derivative of the binding energy as a function of nucleon number, is more sensitive to the local decrease in the single-particle density associated with a shell gap than the two-nucleon separation energy $S_{2n}(Z, N)$.

REFERENCES

- [1] A. Sobiczewski, F. A. Gareev, and B. N. Kalinkin, Phys. Lett. **22**, 500 (1966).
- [2] V. A. Chepurnov, Yad. Fis. **6**, 955 (1967).
- [3] H. Meldner, Ark. Fys. **36**, 593 (1967).
- [4] S. G. Nilsson, J. R. Nix, A. Sobiczewski, Z. Szymanski, S. Wycech, C. Gustafsson, and P. Möller, Nucl. Phys. **A115**, 545 (1968).
- [5] S. G. Nilsson, C. F. Tsang, A. Sobiczewski, Z. Szymanski, S. Wycech, C. Gustafsson, I.-L. Lamm, P. Möller, and B. Nilsson, Nucl. Phys. **A131**, 1 (1969).
- [6] U. Mosel and W. Greiner, Z. Phys. **222**, 261 (1969).
- [7] S. Hofmann, V. Ninov, F. P. Hessberger, P. Armbruster, H. Folger, G. Münzenberg, H. J. Schött, A. G. Popeko, A. V. Yeremin, S. Saro, R. Janik, and M. Leino, Z. Phys. **A354**, 229 (1996).
- [8] Yu. Ts. Oganessian, V. K. Utyonkov, Yu. V. Lobanov, F. Sh. Abdullin, A. N. Polyakov, I. V. Shirokovsky, Yu. S. Tsyganov, G. G. Gulbekian, S. L. Bogomolov, B. N. Gikal, A. N. Mezentsev, S. Iliev, V. G. Subbotin, A. M. Sukhov, G. V. Buklanov, K. Subotic, M. G. Itkis, K. J. Moody, J. F. Wild, N. J. Stoyer, M. A. Stoyer, and R. W. Lougheed, Phys. Rev. Lett. **83**, 3154 (1999).
- [9] Yu. Ts. Oganessian, V. K. Utyonkov, Yu. V. Lobanov, F. Sh. Abdullin, A. N. Polyakov, I. V. Shirokovsky, Yu. S. Tsyganov, G. G. Gulbekian, S. L. Bogomolov, B. N. Gikal, A. N. Mezentsev, S. Iliev, V. G. Subbotin, A. M. Sukhov, O. V. Ivanov, G. V. Buklanov, K. Subotic, M. G. Itkis, K. J. Moody, J. F. Wild, N. J. Stoyer, M. A. Stoyer, R. W. Lougheed, C. A. Laue, Ye. A. Karelina, and A. N. Tatarinov, Phys. Rev. C **63**, 011301(R) (2001).
- [10] S. Hofmann and G. Münzenberg, Rev. Mod. Phys. **72**, 733 (2000).
- [11] P. Armbruster, Ann. Rev. Nucl. Part. Sci. **50**, 411 (2000).
- [12] Y. T. Oganessian, Nucl. Phys. **A685**, 17c (2001).
- [13] Z. Patyk and A. Sobiczewski, Nucl. Phys. **A533**, 132 (1991).
- [14] S. Ćwiok, J. Dobaczewski, P.-H. Heenen, P. Magierski, and W. Nazarewicz, Nucl. Phys. **A611**, 211 (1996).
- [15] P. Möller and J. R. Nix, J. Phys. **G20**, 1681 (1994).
- [16] K. Rutz, M. Bender, T. Bürvenich, T. Schilling, P.-G. Reinhard, J. A. Maruhn, and W. Greiner, Phys. Rev. C **56**, 238 (1997).
- [17] M. Bender, K. Rutz, P.-G. Reinhard, J. A. Maruhn, and W. Greiner, Phys. Rev. C **60**, 034304 (1999).
- [18] G. A. Lalazissis, M. M. Sharma, P. Ring, and Y. K. Gambhir, Nucl. Phys. **A608**, 202 (1996).
- [19] M. Rashdan, Phys. Rev. C **63**, 044303 (2001).
- [20] P.-G. Reinhard, M. Bender and J. A. Maruhn, Comments on Modern Physics **2**, A177 (2002).
- [21] J.-F. Berger, L. Bitaud, J. Dechargé, M. Girod, and K. Dietrich, Nucl. Phys. **A685**, 1c (2001).
- [22] J. Dechargé, J.-F. Berger, K. Dietrich, and M. S. Weiss, Phys. Lett. **B451**, 275 (1999).
- [23] P. Ring, Prog. Part. Nucl. Phys. **37**, 193 (1996).
- [24] K. Rutz, M. Bender, P.-G. Reinhard, J. A. Maruhn, and W. Greiner, Nucl. Phys. **A634**, 67 (1998).

- [25] P. Quentin and H. Flocard, Ann. Rev. Nucl. Part. Sci. **28**, 523 (1978).
- [26] P. Ring and P. Schuck, *The Nuclear Many-body Problem* (Springer Verlag, Heidelberg, 1980)
- [27] C. Mahaux, P. F. Bortignon, R. A. Broglia, and C. H. Dasso, Phys. Rep. **120**, 1 (1985).
- [28] T. Bürvenich, K. Rutz, M. Bender, P.-G. Reinhard, J. A. Maruhn, and W. Greiner, Eur. Phys. J. **A3**, 139 (1998).
- [29] A. V. Afanasjev, J. König, and P. Ring, Phys. Rev. C **60**, 051303 (1999).
- [30] A. V. Afanasjev, P. Ring, and J. König, Nucl. Phys. **A676**, 196 (2000).
- [31] B. D. Serot and J. D. Walecka, Adv. Nucl. Phys. **16**, 1 (1986).
- [32] P.-G. Reinhard, Rep. Prog. Phys. **52**, 439 (1989).
- [33] H. J. Lipkin, Ann. Phys. **9**, 272 (1960).
- [34] Y. Nogami, Phys. Rev. **134**, 313 (1964).
- [35] Y. Nogami and I. L. Zucker, Nucl. Phys. **60**, 203 (1964).
- [36] H. C. Pradhan, Y. Nogami, and J. Law, Nucl. Phys. **A201**, 357 (1973).
- [37] W. Koepf and P. Ring, Nucl. Phys. **A493**, 61 (1989).
- [38] U. Hofmann and P. Ring, Phys. Lett. **B214**, 307 (1988).
- [39] J. König and P. Ring, Phys. Rev. Lett. **71**, 3079 (1993).
- [40] A. V. Afanasjev, J. König, and P. Ring, Nucl. Phys. **A608**, 107 (1996).
- [41] A. V. Afanasjev and P. Ring, Phys. Rev. C **62**, 031302 (2000).
- [42] T. Gonzales-Llarena, J. L. Egido, G. A. Lalazissis, and P. Ring, Phys. Lett. **B379**, 13 (1996).
- [43] J. F. Berger, M. Girod, and D. Gogny, Comp. Phys. Comm. **63**, 365 (1991).
- [44] J. F. Berger, M. Girod, and D. Gogny, Nucl. Phys. **A428**, 23c (1984).
- [45] A. V. Afanasjev and S. Frauendorf, in preparation.
- [46] A. V. Afanasjev, J. König, P. Ring, L. M. Robledo, and J. L. Egido, Phys. Rev. C **62**, 054306 (2000).
- [47] P.-G. Reinhard, M. Rufa, J. Maruhn, W. Greiner and J. Friedrich, Z. Phys. **A323**, 13 (1986).
- [48] M. Rufa, P.-G. Reinhard, J. A. Maruhn, W. Greiner, and M. R. Strayer, Phys. Rev. C **38**, 390 (1988).
- [49] G. A. Lalazissis, J. König and P. Ring, Phys. Rev. C **55**, 540 (1997).
- [50] M. M. Sharma, M. A. Nagarajan and P. Ring, Phys. Lett. **B312**, 377 (1993).
- [51] M. Bender, K. Rutz, P.-G. Reinhard, and J. A. Maruhn, Eur. Phys. J. **A7**, 467 (2000).
- [52] M. Bender, report nucl-th/0106024, Phys. Rev. C, in press.
- [53] M. Warda, J. L. Egido, L. M. Robledo, and K. Pomorski, Phys. Rev. C **66**, 014310 (2002).
- [54] P. Reiter, T. L. Khoo, C. J. Lister, D. Seweryniak, I. Ahmad, M. Alcorta, M. P. Carpenter, J. A. Cizewski, C. N. Davids, G. Gervais, J. P. Greene, W. F. Henning, R. V. F. Janssens, T. Lauritsen, S. Siem, A. A. Sonzogni, D. Sullivan, J. Uusitalo, I. Wiedenhöver, N. Amzal, P. A. Butler, A. J. Chewter, K. Y. Ding, N. Fotiades, J. D. Fox, P. T. Greenlees, R.-D. Herzberg, G. D. Jones, W. Korten, M. Leino, and K. Vetter, Phys. Rev. Lett. **82**, 509 (1999).
- [55] P. Reiter, T. L. Khoo, T. Lauritsen, C. J. Lister, D. Seweryniak, A. A. Sonzogni, I. Ahmad, N. Amzal, P. Bhattacharyya, P. A. Butler, M. P. Carpenter, A. J. Chewter, J. A. Cizewski, C. N. Davids, K. Y. Ding, N. Fotiades, J. P. Greene, P. T. Green-

- lees, A. Heinz, W. F. Henning, R.D. Herzberg, R. V. F. Janssens, G. D. Jones, H. Kankaanpää, F. G. Kondev, W. Korten, M. Leino, S. Siem, J. Uusitalo, K. Vetter, and I. Wiedenhöver, Phys. Rev. Lett. **84**, 3542 (2000).
- [56] M. Leino, H. Kankaanpää, R.-D. Herzberg, A. J. Chewter, F. P. Heβberger, Y. Le Coz, F. Becker, P. A. Butler, J. F. C. Cocks, O. Dorvaux, K. Eskola, J. Gerl, P. T. Greenlees, K. Helariutta, M. Houry, G. D. Jones, P. Jones, R. Julin, S. Juutinen, H. Kettunen, T. L. Khoo, A. Kleinböh, W. Korten, P. Kuusiniemi, R. Lucas, M. Muikku, P. Nieminen, R. D. Page, P. Rahkila, P. Reiter, A. Savelius, Ch. Schlegel, Ch. Theisen, W. H. Trzaska, and H.-J. Wollersheim, Eur. Phys. J. **A6**, 63 (1999).
- [57] A. V. Afanasjev, I. Ragnarsson, and P. Ring, Phys. Rev. C **59**, 3166 (1999).
- [58] A. V. Afanasjev, J. König and P. Ring, Nucl. Phys. **A608**, 107 (1996).
- [59] A. V. Afanasjev, G. A. Lalazissis, and P. Ring, Nucl. Phys. **A634**, 395 (1998).
- [60] A. V. Afanasjev, unpublished
- [61] D. Gogny, in *Nuclear self-consistent fields*, Proc. Internat. Conf. held at the Center for Theoretical Physics, Trieste, Italy, 1975, Eds. G. Ripka and M. Porneuf (North-Holland, Amsterdam, 1975), p. 333.
- [62] M. Farine, D. Von-Eiff, P. Schuck, J. F. Berger, J. Dechargé, and M. Girod, J. Phys. **G25**, 863 (1999).
- [63] S. G. Nilsson and I. Ragnarsson, *Shapes and Shells in Nuclear Structure* (Cambridge University Press, Cambridge, 1995).
- [64] R. Julin, Nucl. Phys. **A685**, 221c (2001).
- [65] J. L. Egido and L. M. Robledo, Phys. Rev. Lett. **85**, 1198 (2000).
- [66] Y. S. Chen and S. Frauendorf, Nucl. Phys. **A393**, 135 (1983).
- [67] J. L. Egido and P. Ring, Nucl. Phys. **A423**, 93 (1984).
- [68] A. Sobiczewski, I. Muntian, and Z. Patyk, Phys. Rev. C **63**, 034306 (2001).
- [69] S. Ćwiok, J. Dudek, W. Nazarewicz, J. Skalski, and T. Werner, Comp. Phys. Com. **46**, 379 (1987).
- [70] T. Duguet, P. Bonche and P.-H. Heenen, Nucl. Phys. **A679**, 427 (2001).
- [71] H. Laftchiev, D. Samsoen, P. Quentin and J. Piperova, Eur. Phys. J. **A12**, 155 (2001).
- [72] J. L. Egido, private communication (2001)
- [73] S. Raman, C. H. Malarkey, W. T. Milner, C. W. Nestor, Jr., and P. H. Stelson, At. Data and Nuclear Data Tables **36**, 1 (1987).
- [74] L. Grodzins, Phys. Lett. **2**, 88 (1962).
- [75] R.-D. Herzberg, N. Amzal, F. Becker, P. A. Butler, A. J. C. Chewter, J. F. C. Cocks, O. Dorvaux, K. Eskola, J. Gerl, P. T. Greenlees, N. J. Hammond, K. Hauschild, K. Helariutta, F. Heβberger, M. Houry, G. D. Jones, P. M. Jones, R. Julin, S. Juutinen, H. Kankaanpää, H. Kettunen, T. L. Khoo, W. Korten, P. Kuusiniemi, Y. Le Coz, M. Leino, C. J. Lister, R. Lucas, M. Muikku, P. Nieminen, R. D. Page, P. Rahkila, P. Reiter, Ch. Schlegel, C. Scholey, O. Stezowski, Ch. Theisen, W. H. Trzaska, J. Uusitalo, and H. J. Wollersheim, Phys. Rev. C **65**, 014303 (2002).
- [76] W. Nazarewicz and I. Ragnarsson, *Nuclear deformations* in *Handbook on nuclear properties*, Eds. D. N. Poenaru and W. Greiner (Clarendon Press, Oxford, 1996) p. 80.
- [77] A. T. Kruppa, M. Bender, W. Nazarewicz, P.-G. Reinhard, T. Vertse, and S. Ćwiok, Phys. Rev. **C61**, 034313 (2000).
- [78] M. Bender, W. Nazarewicz, and P.-G. Reinhard, Phys. Lett. **B515**, 42 (2001).

- [79] R. R. Chasman, I. Ahmad, A. M. Friedman, and J. R. Erskine, Rev. Mod. Phys. **49**, 833 (1977).
- [80] I. Ahmad and R. W. Hoff, in preparation, to be published in “Table of Isotopes”
- [81] I. Ahmad, R. K. Sjöblom, and P. R. Fields, Phys. Rev. C **14**, 218 (1976).
- [82] I. Ahmad, M. P. Carpenter, R. R. Chasman, J. P. Greene, R. V. F. Janssens, T. L. Khoo, F. G. Kondev, T. Lauritsen, C. J. Lister, P. Reiter, D. Seweryniak, A. Sonzogni, J. Uusitalo, and I. Wiedenhöver, Phys. Rev. C **62**, 064302 (2000).
- [83] I. Ahmad, F. T. Porter, M. S. Freedman, R. F. Barnes, R. K. Sjöblom, F. Wagner, Jr., J. Milsted, and P. R. Fields, Phys. Rev. C **3**, 390 (1971).
- [84] V. G. Soloviev, *Theory of Complex Nuclei* (Pergamon, 1976).
- [85] V. G. Soloviev, *Theory of Atomic Nuclei: Quasiparticles and Phonons* (Institute of Physics Publishing, Bristol and Philadelphia, 1992).
- [86] L. A. Malov, private communication (2001).
- [87] P. Ring, R. Beck, and H. J. Mang, Z. Phys. **231**, 10 (1970).
- [88] J. L. Egido, H. J. Mang, and P. Ring, Nucl. Phys. **A334**, 1 (1980).
- [89] I. Ahmad, R. R. Chasman, A. M. Friedman, and S. W. Yates, Phys. Lett. **B251**, 338 (1990).
- [90] M. Jaminon and C. Mahaux, Phys. Rev. **C40**, 354 (1989).
- [91] A. Bohr and B. R. Mottelson, *Nuclear Structure*, Vol. II (World Scientific, 1998).
- [92] F. A. Gareev, S. P. Ivanova, L. A. Malov, and V. G. Soloviev, Nucl. Phys. **A171**, 134 (1971).
- [93] S. P. Ivanova, A. L. Komov, L. A. Malov, and V. G. Soloviev, Izv. Akad. Nauk SSSR, Ser. Fiz. 37, 911 (1973) [Bull. Acad. Sci. USSR, Phys. Ser., **v. 37, No. 5**, 3 (1973)].
- [94] F. S. Stephens, Rev. Mod. Phys. **47**, 43 (1975).
- [95] T. Niksic, D. Vretenar, P. Ring and G. A. Lalazissis, Phys. Rev. C **65**, 054320 (2002).
- [96] I. Ahmad, R. R. Chasman, and P. R. Fields, Phys. Rev. C **61**, 044301 (2000).
- [97] R. R. Chasman and I. Ahmad, Phys. Lett. **B392**, 255 (1997).
- [98] T. Duguet, P. Bonche, P.-H. Heenen, J. Meyer, Phys. Rev. **C65**, 014310 (2002).
- [99] A. V. Afanasjev, P. Ring, and I. Ragnarsson, Proc. of the Int. Workshop PINGST2000 “Selected topics on $N = Z$ nuclei”, 2000, Lund, Sweden, Eds. D. Rudolph and M. Hellström, (2000) p. 183
- [100] R. M. Clark, S. Bouneau, A. N. Wilson, B. Cederwall, F. Azaiez, S. Asztalos, J. A. Becker, L. Bernstein, M. J. Brinkman, M. A. Deleplanque, I. Delonche, R. M. Diamond, J. Duprat, P. Fallon, L. P. Farris, E. A. Henry, J. R. Hughes, W. H. Kelly, I. Y. Lee, A. O. Macchiavelli, M. G. Porquet, J. F. Sharpey-Schafer, F. S. Stephens, M. A. Stoyer, and D. T. Vo, Phys. Rev. **C 53**, 117 (1996).
- [101] R. M. Clark, S. Bouneau, F. Azaiez, S. Asztalos, J. A. Becker, B. Cederwall, M. A. Deleplanque, R. M. Diamond, J. Duprat, P. Fallon, L. P. Farris, E. A. Henry, J. R. Hughes, W. H. Kelly, I. Y. Lee, A. O. Macchiavelli, M. G. Porquet, J. F. Sharpey-Schafer, F. S. Stephens, M. A. Stoyer, D. T. Vo, and A. Wilson, Phys. Rev. **C51**, R1052 (1995).
- [102] V. M. Strutinsky, Nucl. Phys. **A95**, 420 (1967).
- [103] M. Brack, J. Damgaard, A. S. Jensen, H. C. Pauli, V. M. Strutinsky, C. Y. Wong, Rev. Mod. Phys. **44**, 320 (1972).
- [104] J. Dobaczewski, W. Nazarewicz, and T. R. Werner, Phys. Scripta **T56**, 15 (1995).

FIGURES

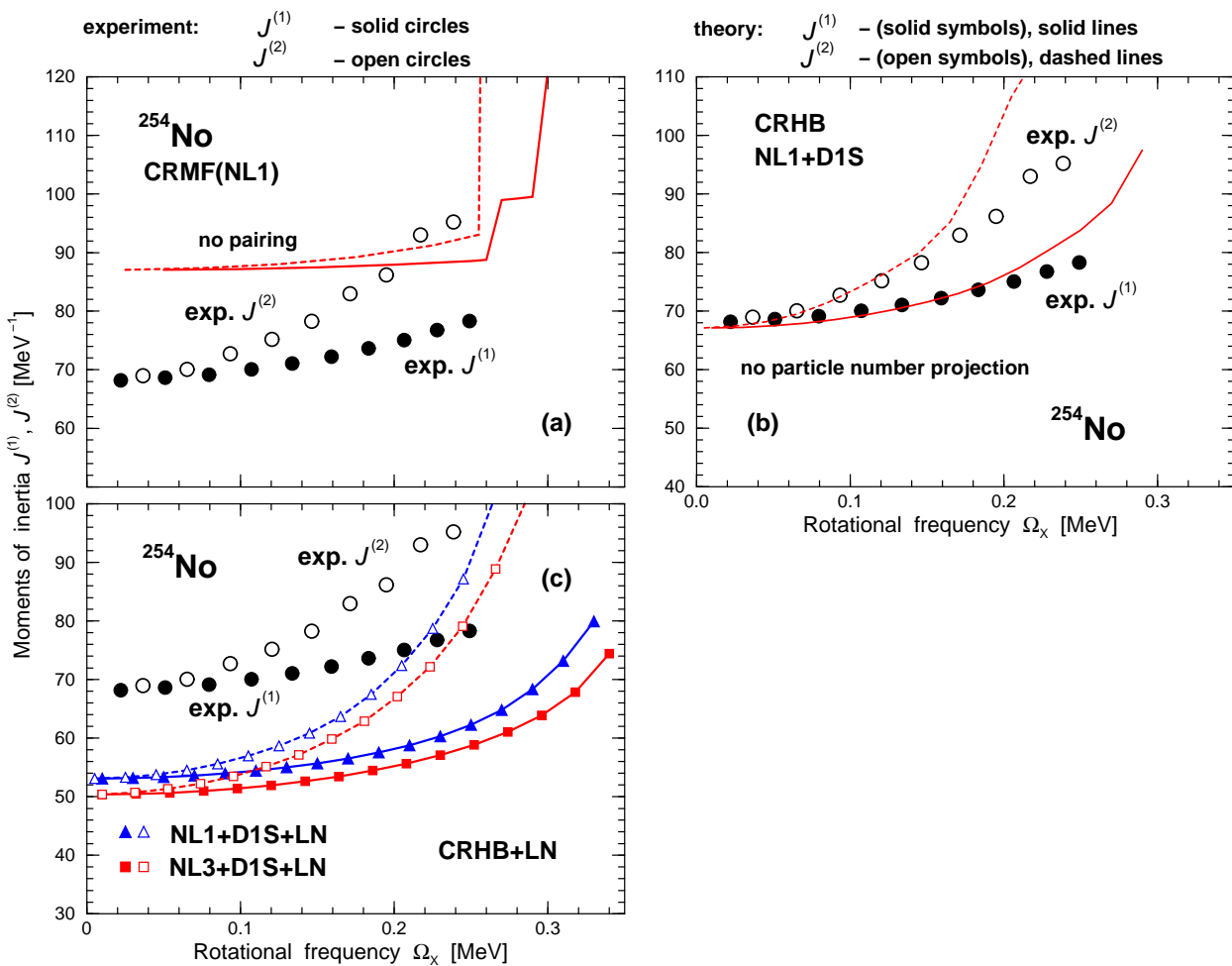


FIG. 1. Experimental and calculated dynamic ($J^{(2)}$) and kinematic ($J^{(1)}$) moments of inertia of the lowest band in ^{254}No . Panel (a) shows the CRMF results without pairing. The CRHB and CRHB+LN results are displayed in panels (b) and (c), respectively. The results of the CRHB(+LN) calculations are shown only up to the rotational frequency where a paired band crossing takes place. Note different scales of the ordinate on different panels.

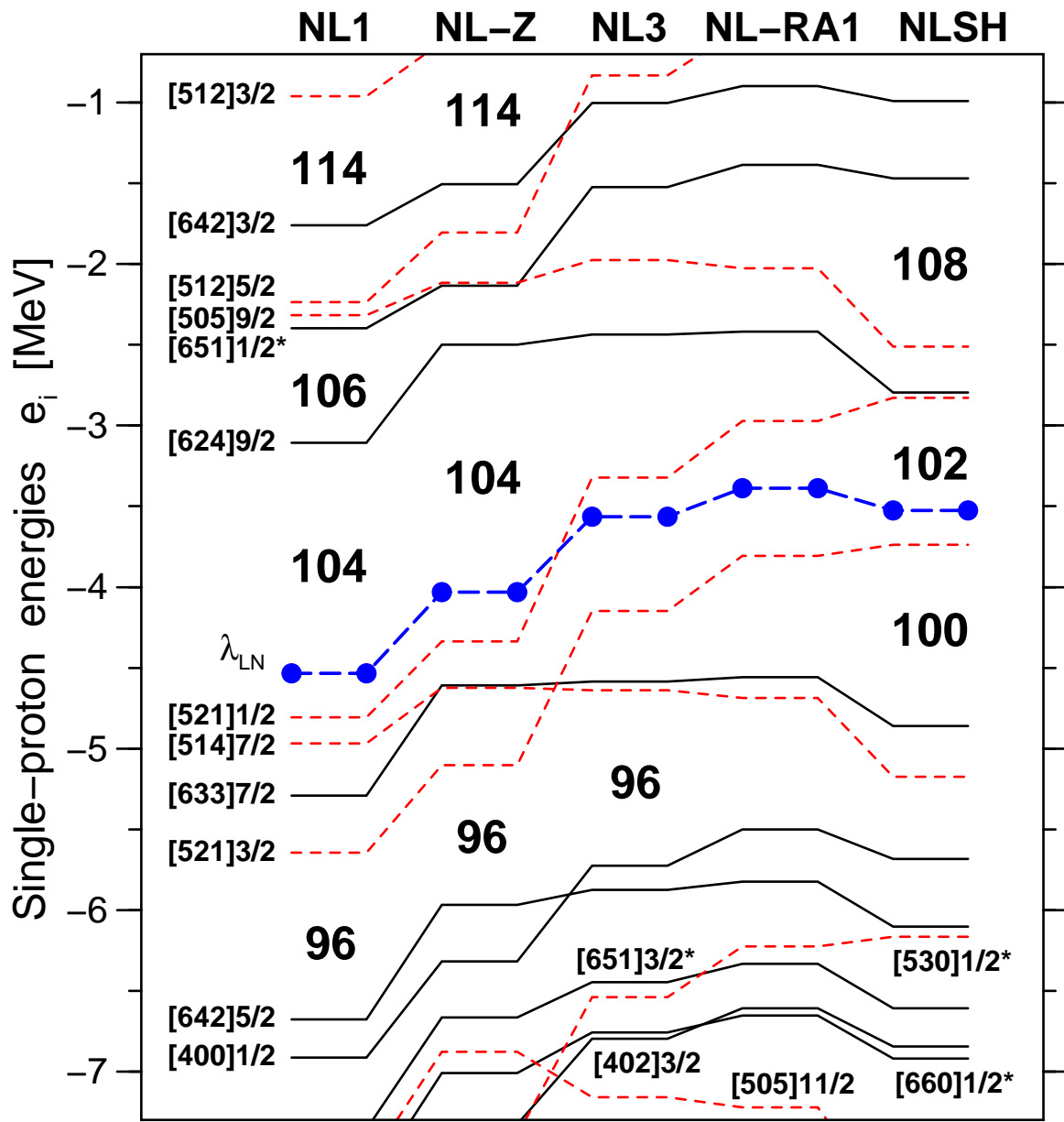


FIG. 2. Single-proton energies in ^{254}No obtained at the equilibrium deformation in the CRHB+LN calculations with different RMF parametrizations. Solid and dashed lines are used for positive and negative parity orbitals, respectively. The λ_{LN} values are shown by the long-dashed line with solid circles. The single-particle orbitals are labeled by means of the asymptotic quantum numbers $[Nn_z\Lambda]\Omega$ (Nilsson quantum numbers) of the dominant component of the wave function. The asterisk (*) at the Nilsson label indicates that the wave function is fragmented and the weight of dominant component is below 50%. In this case, the Nilsson label does not characterize the wave function but is an indicator of the position of the orbital within the $[N]\Omega$ group (see Ref. [63]), where N is the main oscillator quantum number of the dominant N -shell and Ω the projection of total angular momentum onto the symmetry axis. N can be considered as a good approximate quantum number in almost all cases, since typically the weight of a specific N -shell in the structure of the wave function is at least 85% or larger. However, the $\pi[402]3/2$ and $\pi[651]3/2^*$ orbitals are strongly mixed by $\Delta N = \pm 2$ interaction.

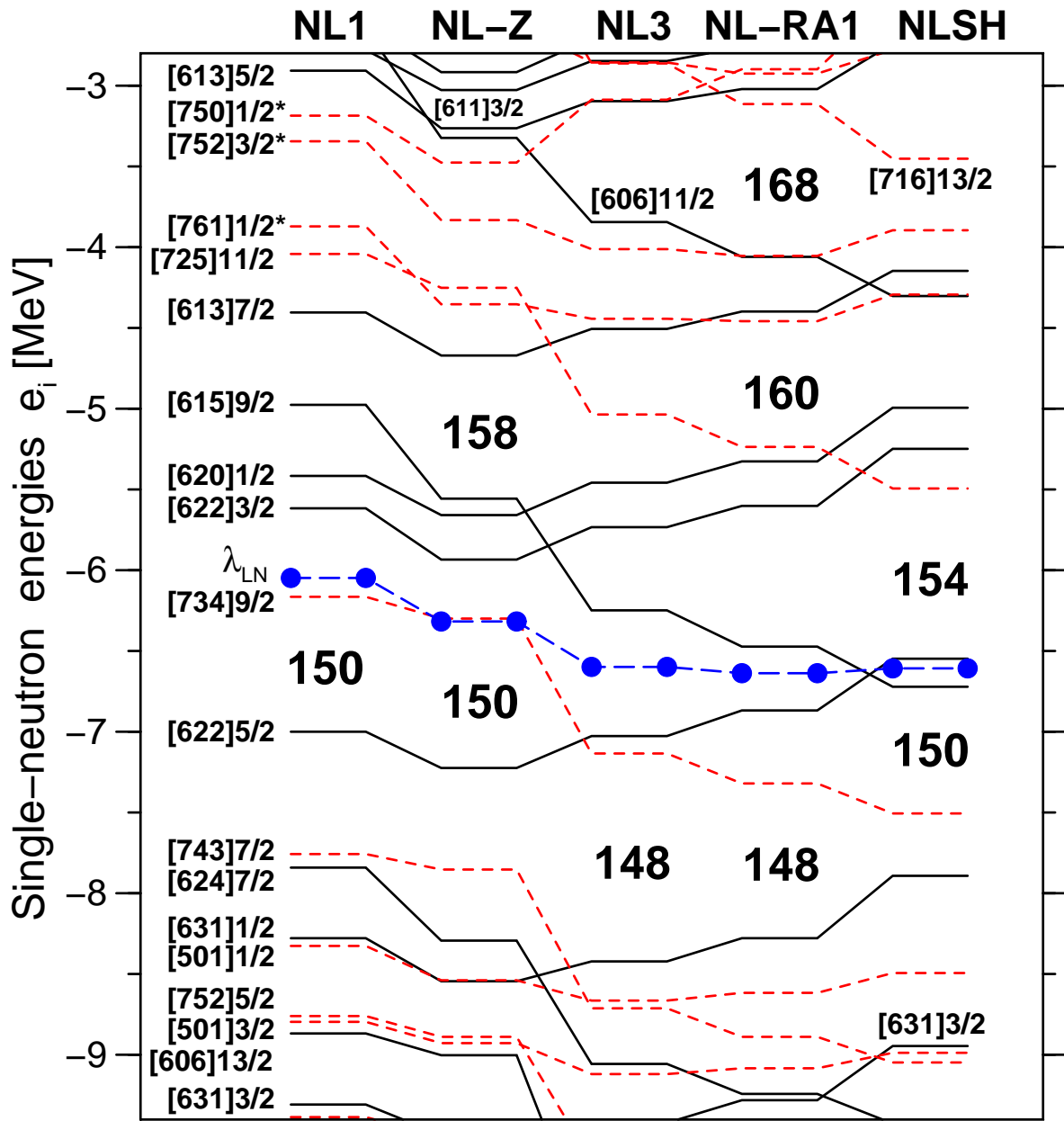


FIG. 3. The same as Fig. 2 but for the single-neutron energies.

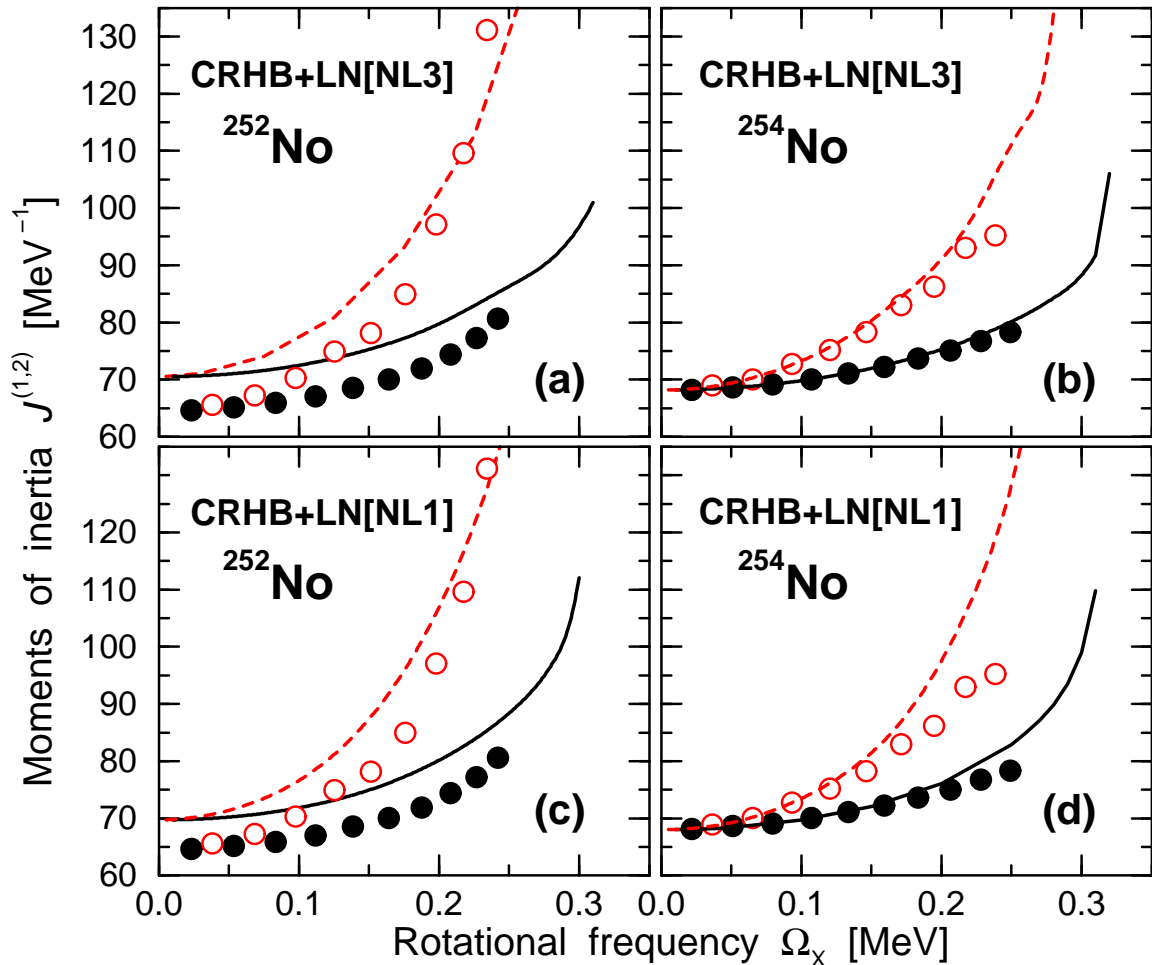


FIG. 4. Experimental and calculated dynamic and kinematic moments of inertia of the normal-deformed bands in $^{252,254}\text{No}$. The experimental $J^{(1)}$ and $J^{(2)}$ values (from Refs. [54–56,64]) are shown by solid and open circles, respectively. Solid and dashed lines are used for the calculated $J^{(1)}$ and $J^{(2)}$ values, respectively. In the calculations, the D1S Gogny force is attenuated by the scaling factor f given in Table I. The results of the calculations with NL3 and NL1 parametrizations are displayed in the upper and the bottom panels, respectively. They are shown only up to a rotational frequency where a sharp band crossing takes place.

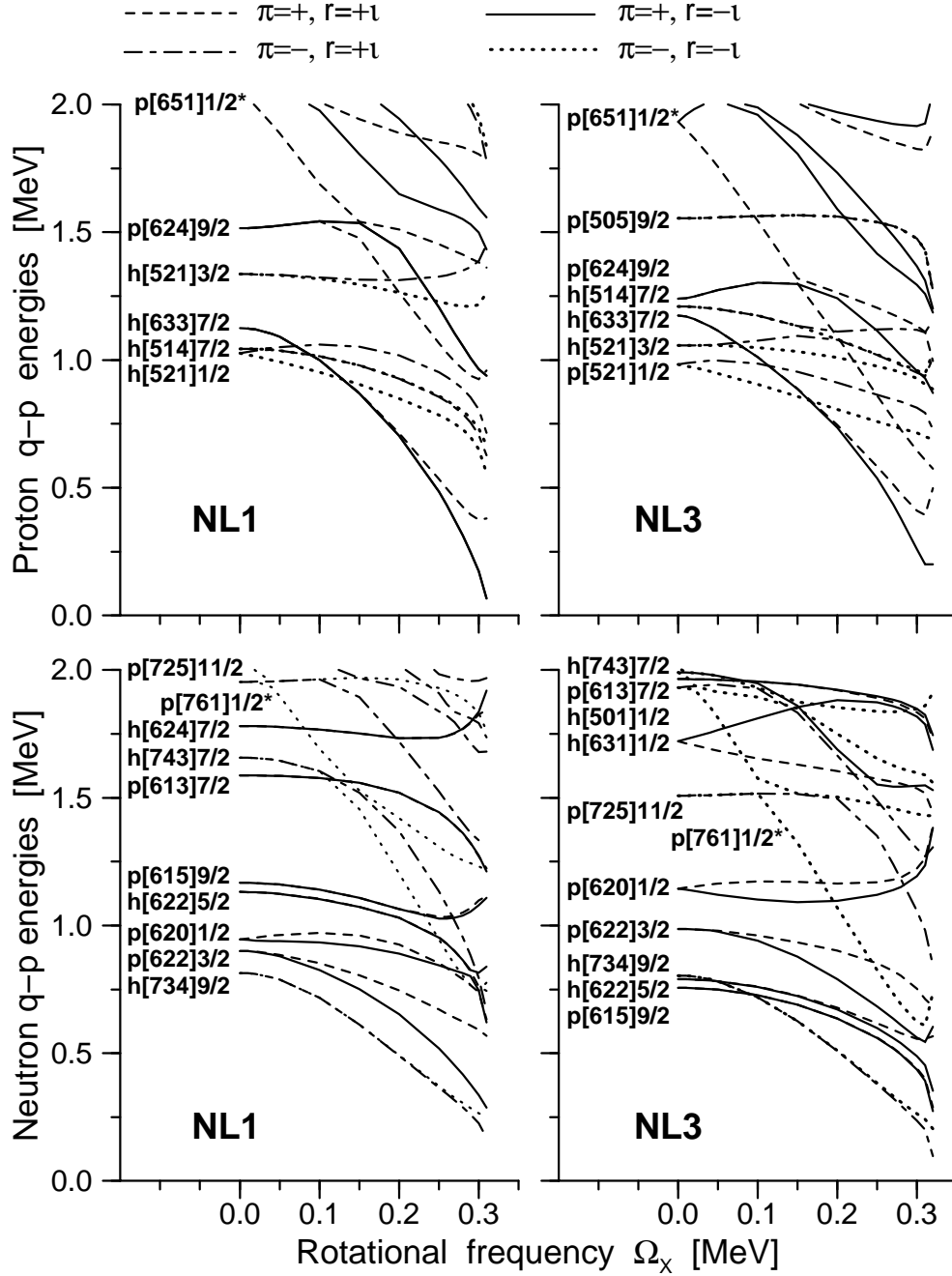


FIG. 5. Proton (top panels) and neutron (bottom panels) quasiparticle energies corresponding to the lowest configuration in ^{254}No . The CRHB+LN calculations have been performed with the NL1 (left panels) and NL3 (right panels) parametrizations. The letters 'p' and 'h' before the Nilsson labels are used to indicate whether a given Routhian is of particle or hole type.

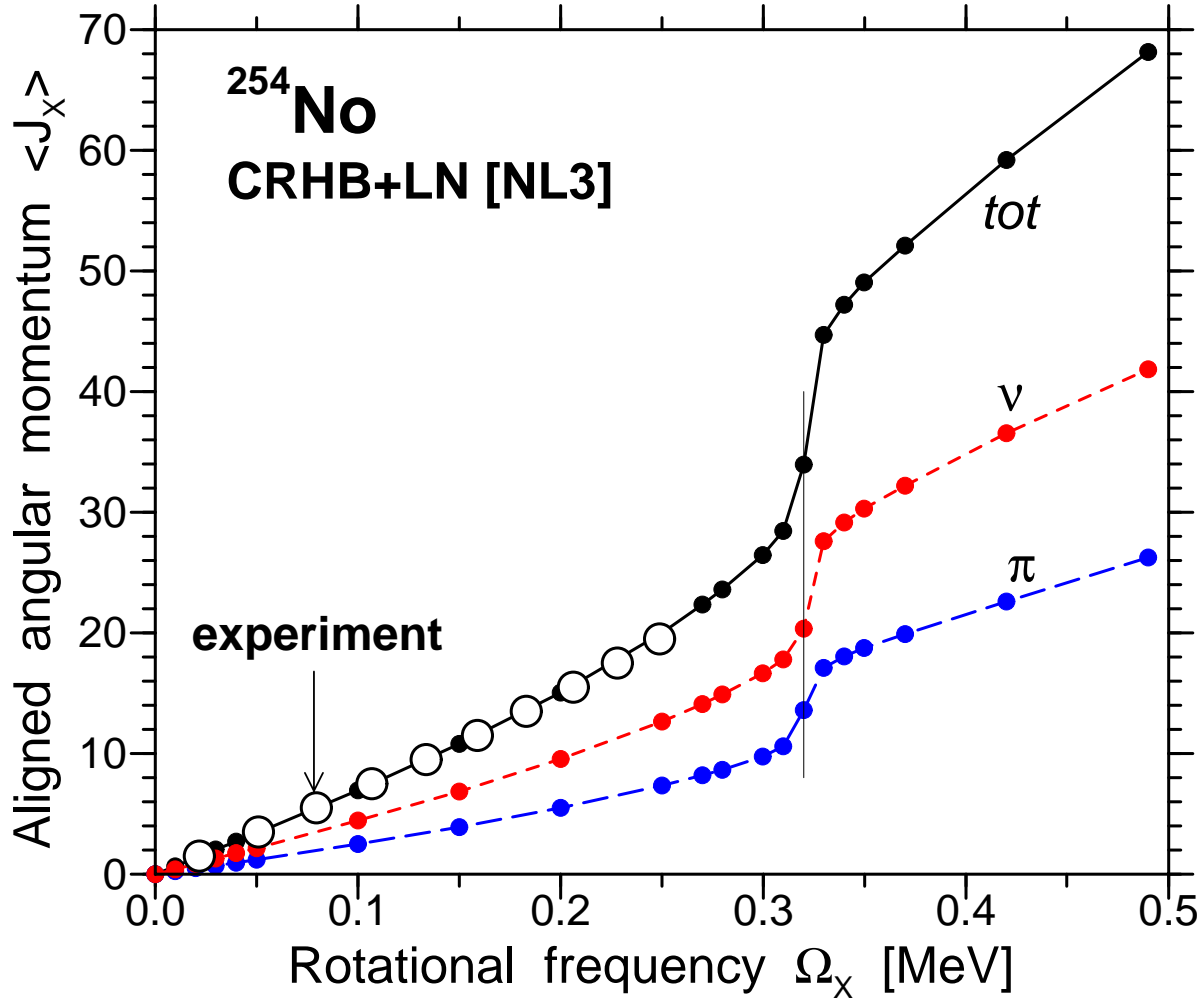


FIG. 6. Aligned angular momenta (in units \hbar) versus rotational frequency Ω_x in ^{254}No . Proton, neutron and total $\langle J_x \rangle$ are shown. Small solid circles on lines show the frequencies at which the CRHB+LN calculations have been performed. The experimental quantities, defined as $\langle J_x \rangle = \sqrt{I(I+1)} \approx I + 1/2$ (see Ref. [66]), are shown by open large circles. The crossing frequency $\Omega_x \approx 0.32$ MeV is indicated by a thin vertical line.

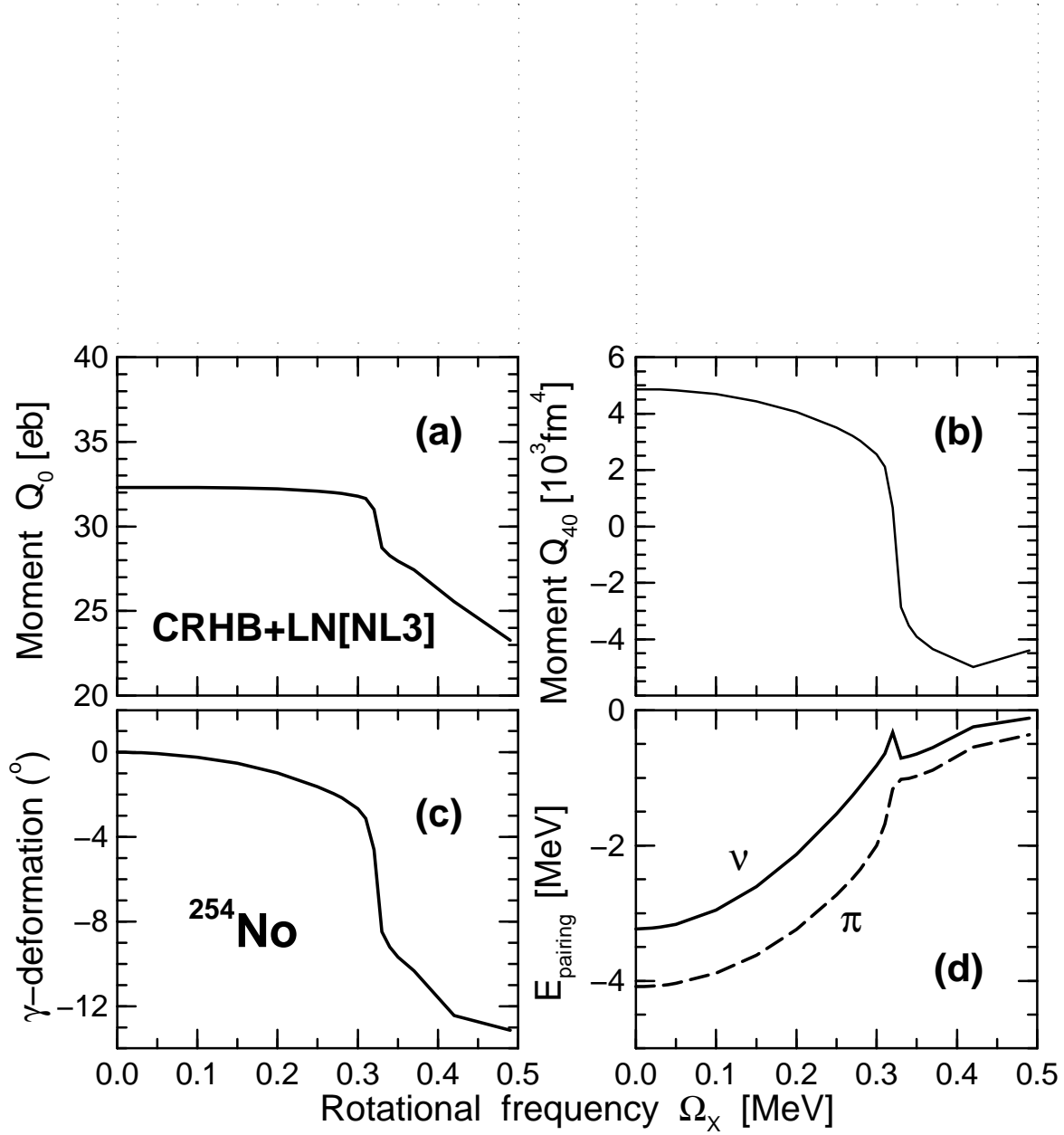


FIG. 7. The results of CRHB+LN calculations with the NL3 parametrization for ^{254}No . Mass quadrupole moments Q_0 , mass hexadecapole moments Q_{40} , and γ -deformation as a function of rotational frequency Ω_x are given on panels (a),(b) and (c), respectively. Proton and neutron pairing energies are shown in panel (d).

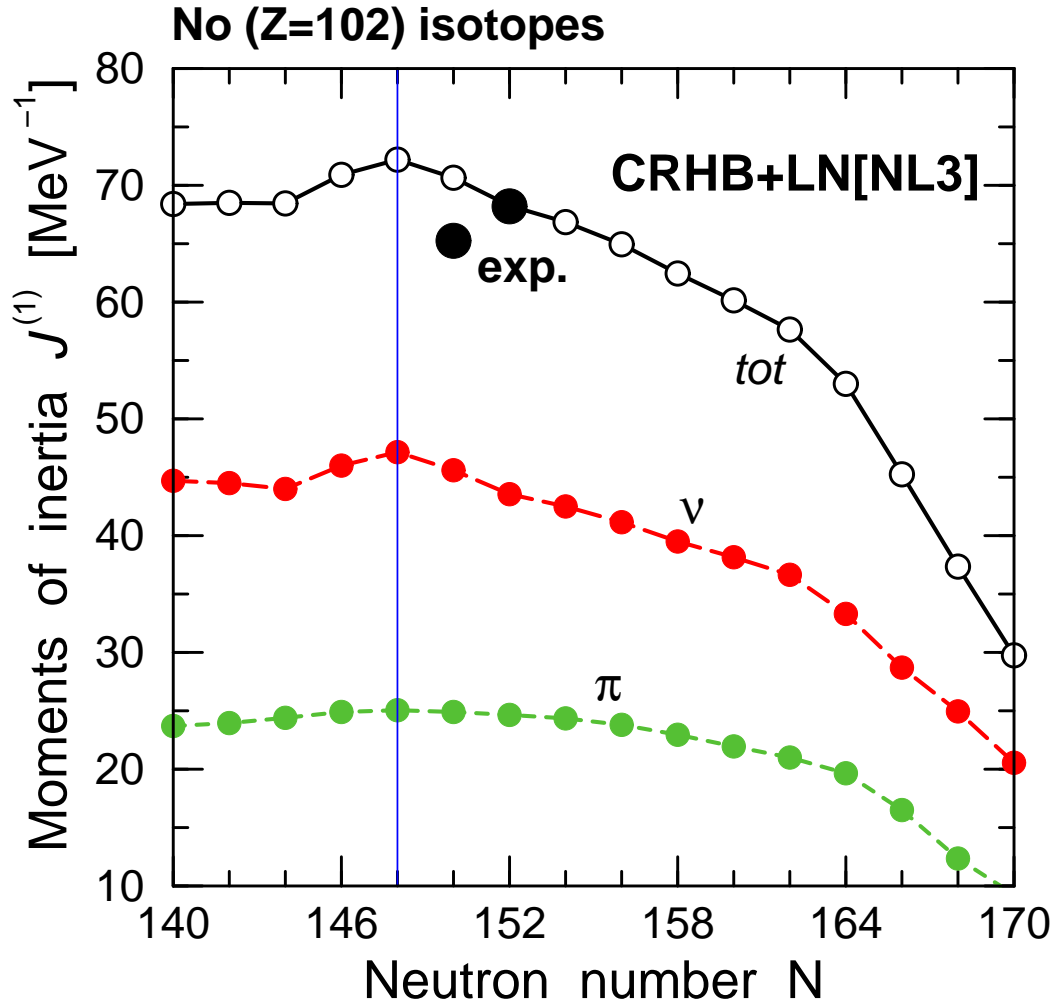


FIG. 8. Kinematic moments of inertia $J^{(1)}$ (total, neutron and proton contributions) in the No isotopes as a function of the neutron number N . The CRHB+LN calculations are carried out with the NL3 parametrization at $\Omega_x = 0.02$ MeV. The vertical line shows the position of the $N = 148$ shell gap.

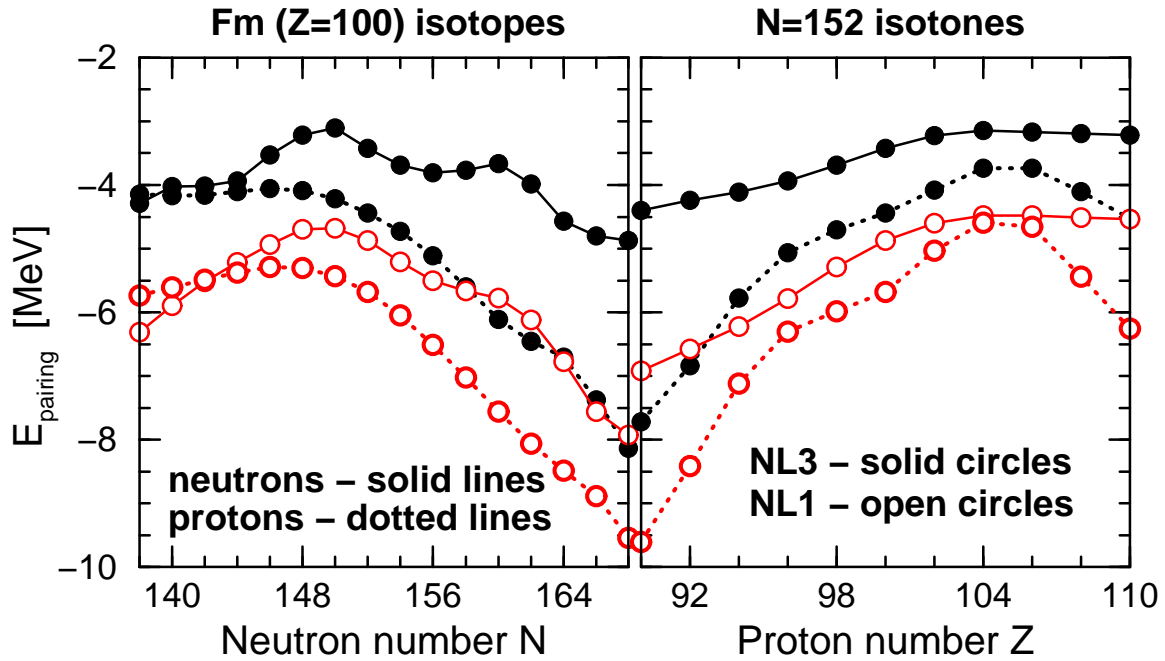


FIG. 9. Proton and neutron pairing energies $E_{pairing} = -\frac{1}{2}Tr(\Delta\kappa)$ obtained in the CRHB+LN calculations with the NL1 and NL3 parametrizations for the Fm ($Z = 100$) isotopes and the $N = 152$ isotones.

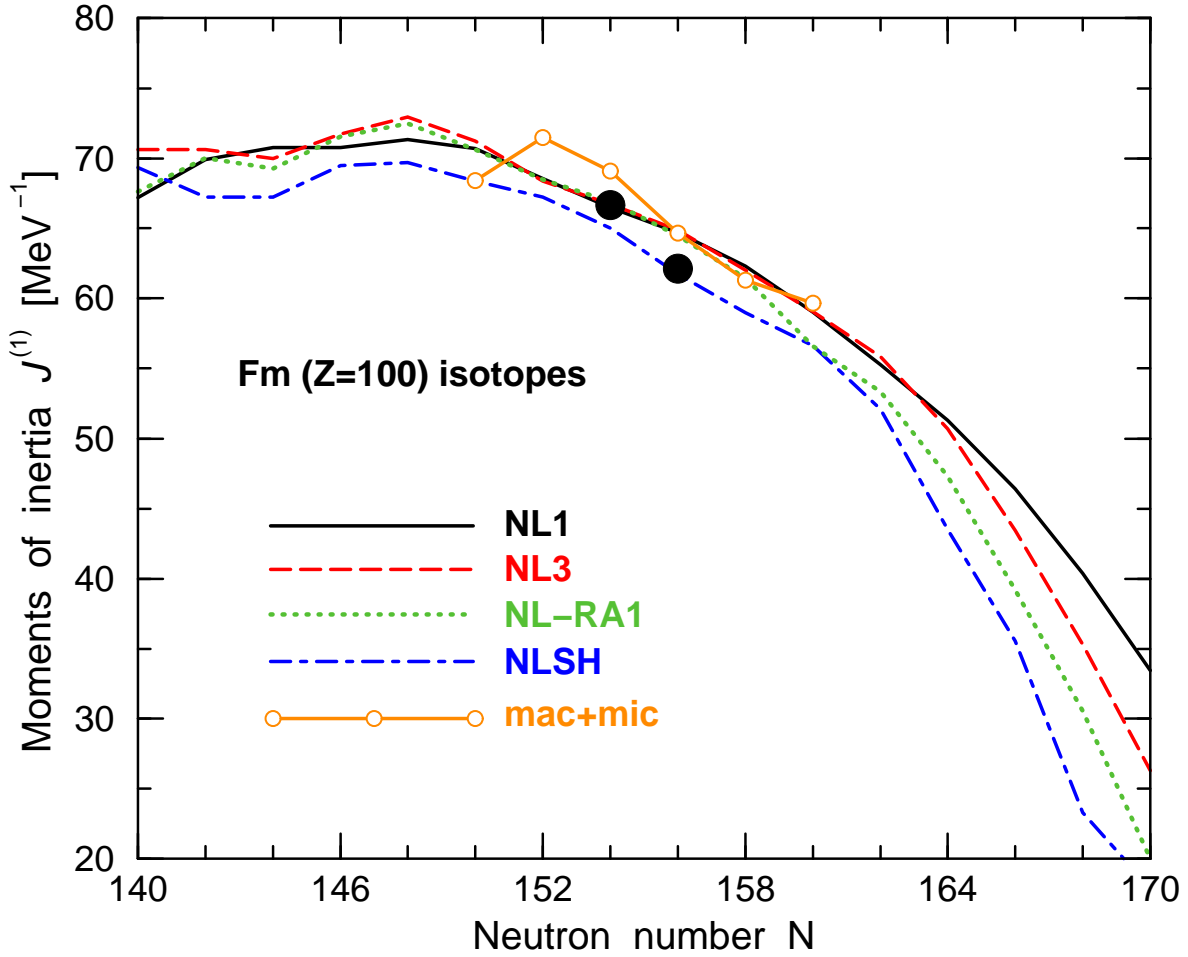


FIG. 10. Kinematic moments of inertia $J^{(1)}$ in the Fm isotopes as a function of the neutron number N . The results of the CRHB+LN calculations at $\Omega_x = 0.02$ MeV with different RMF parametrizations are presented by lines. The results with the NL-Z parametrization follow those with NL1, but are systematically lower by ≈ 1 MeV $^{-1}$. The results of the calculations of Ref. [68] within the macroscopic+microscopic (mac+mic) method are shown by solid lines with open circles. Experimental data are shown by solid circles.

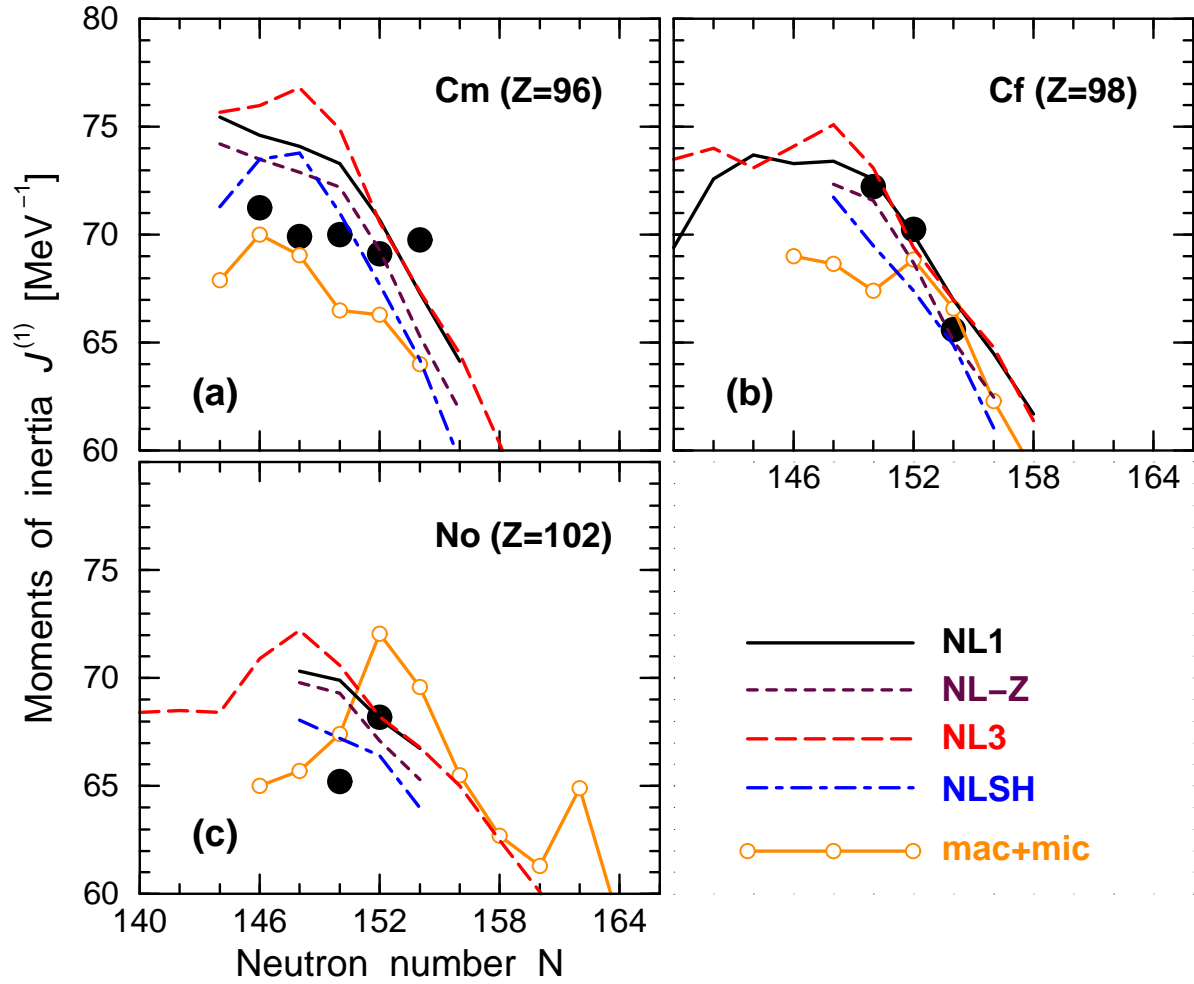


FIG. 11. The same as in Fig. 10, but for Cm, Cf and No isotopes. The results with NL-RA1 almost coincide with those for NL3 that are displayed.

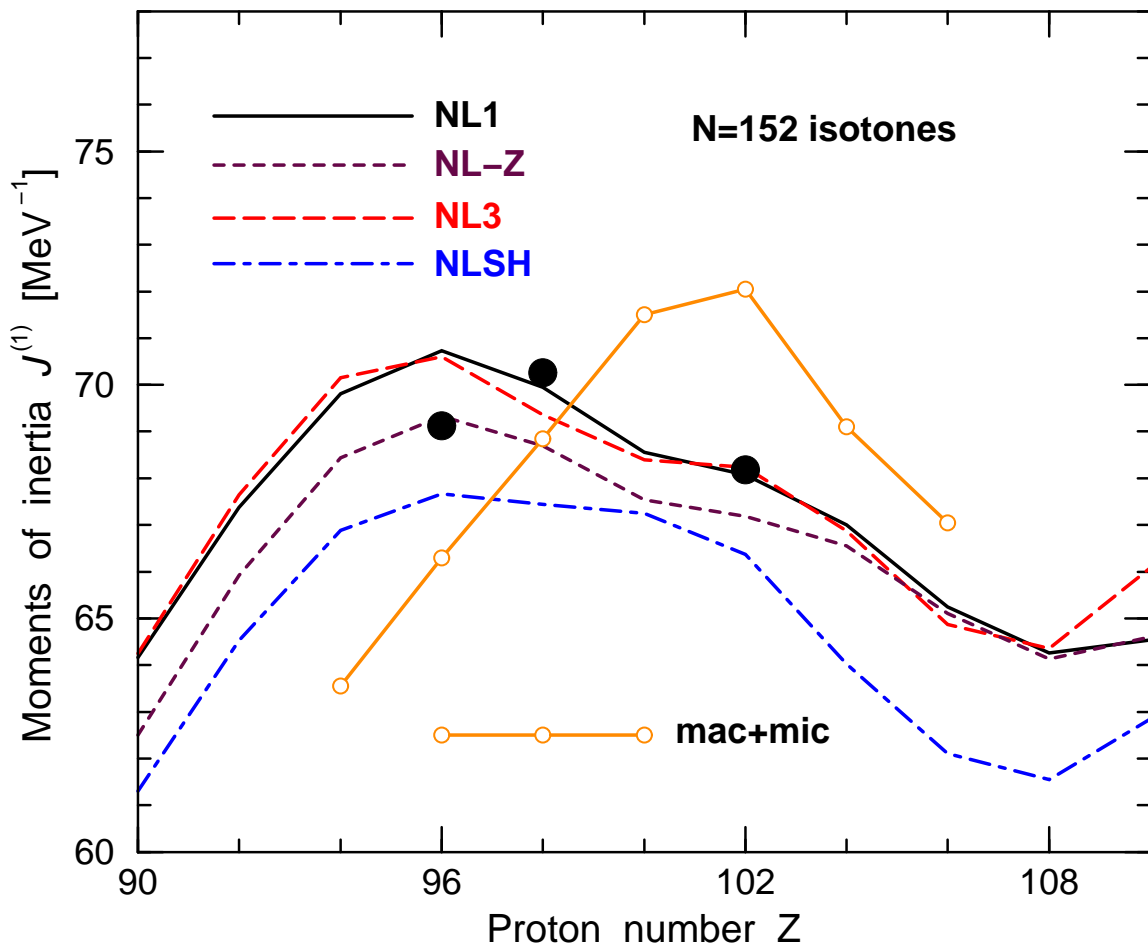


FIG. 12. The same as Fig. 10, but for the $N = 152$ isotones as a function of proton number Z . The results with NL-RA1 are very close to those with NL3.

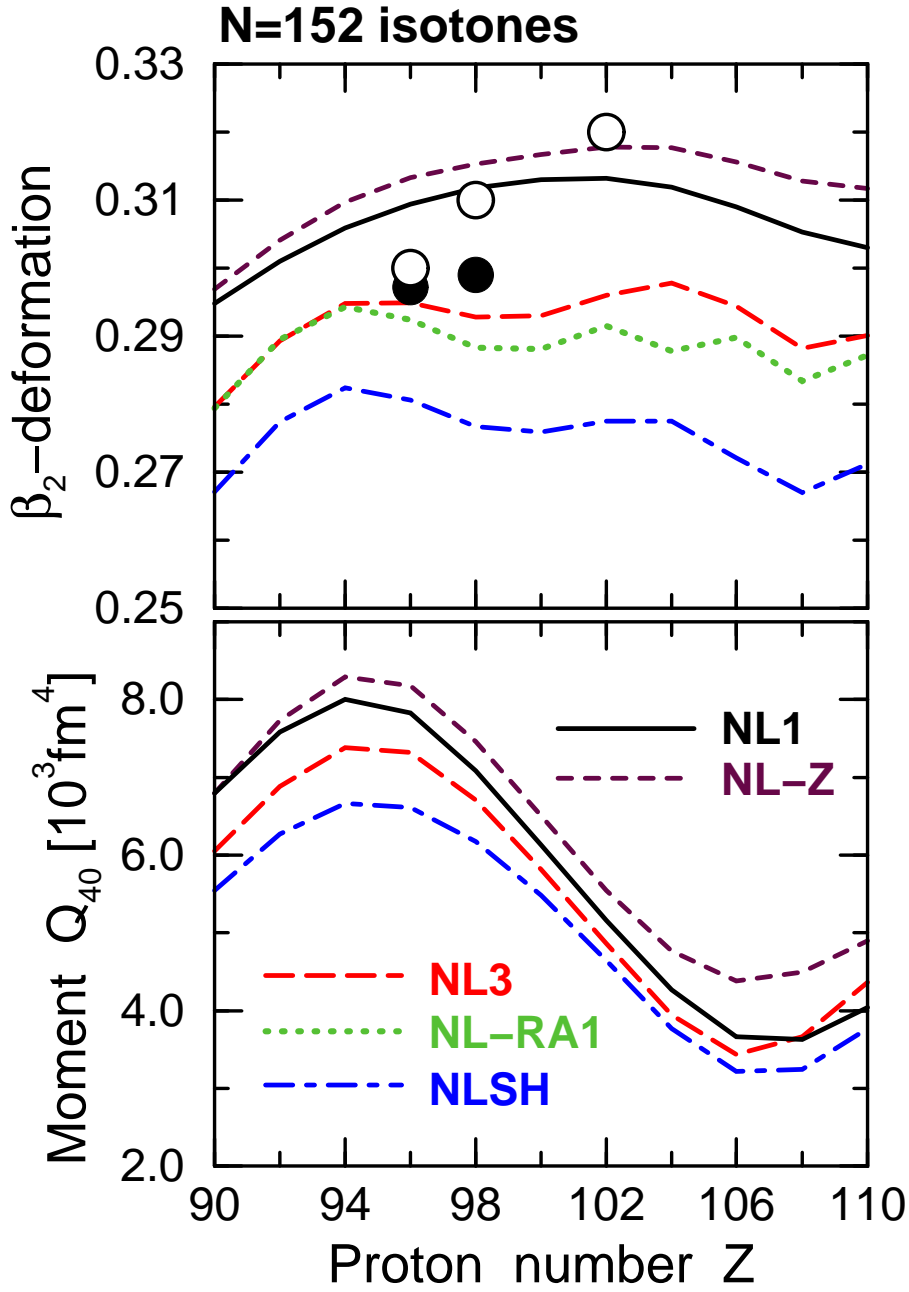


FIG. 13. The calculated (lines) and experimental (circles) deformation parameters β_2 (top panel) and calculated mass hexadecapole moments Q_{40} (bottom panel) in the chain of $N = 152$ isotones. The experimental values of β_2 obtained in the direct measurements [73] are shown by solid circles, while those deduced from the $2^+ \rightarrow 0^+$ transition energies, with the prescription of Ref. [75], are given by open circles. Since the results with NL-RA1 for Q_{40} coincide with those with NL3, they are not shown in the bottom panel.

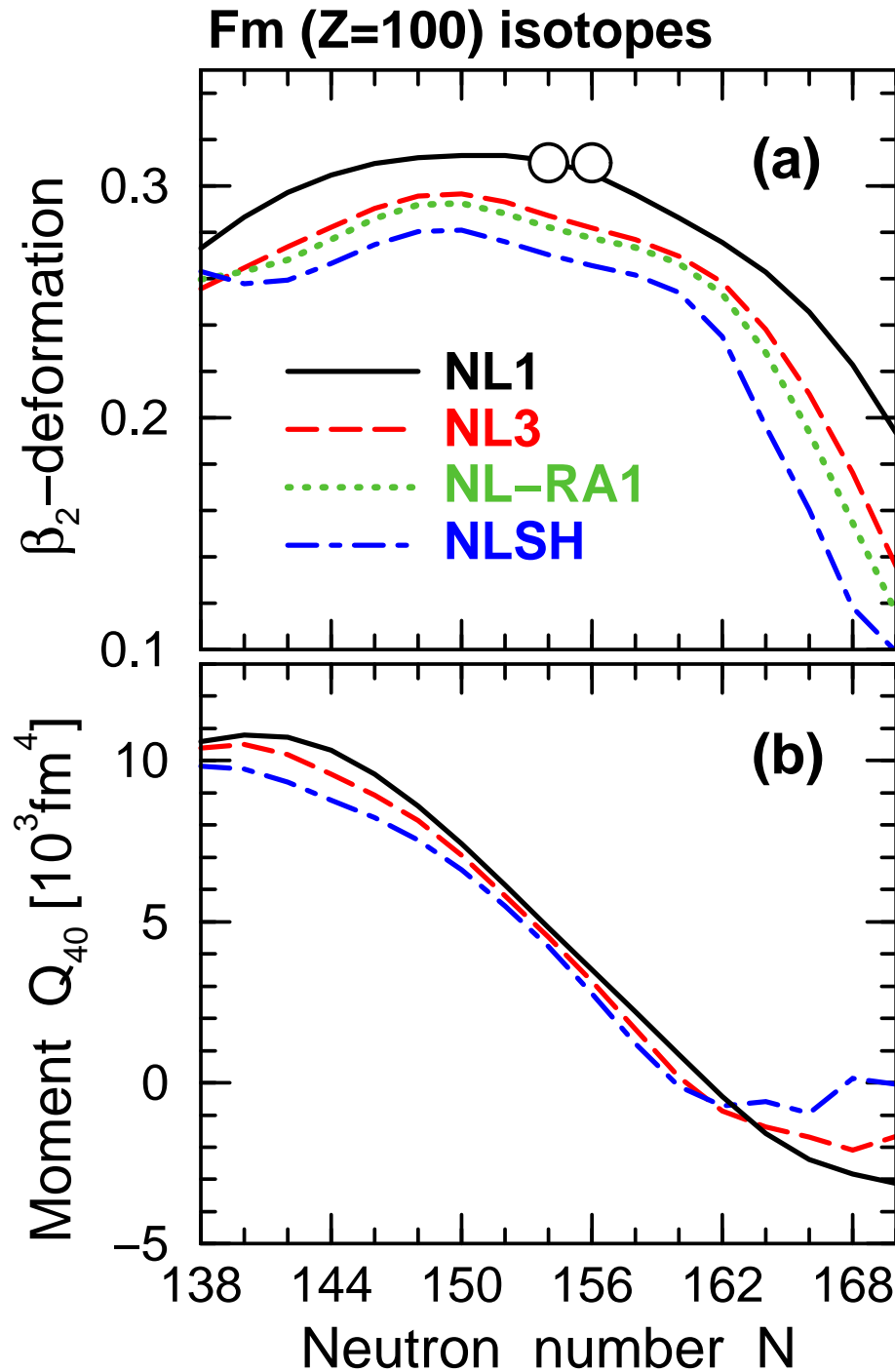


FIG. 14. The same as in Fig. 13, but for the chain of the Fm isotopes. The values of β_2 calculated with NL1 and NL-Z are very close to each other, thus the values obtained with NL-Z are omitted. The results for Q_{40} obtained with NL-RA1 and NL-Z are very close to those with NL3 and NL1.

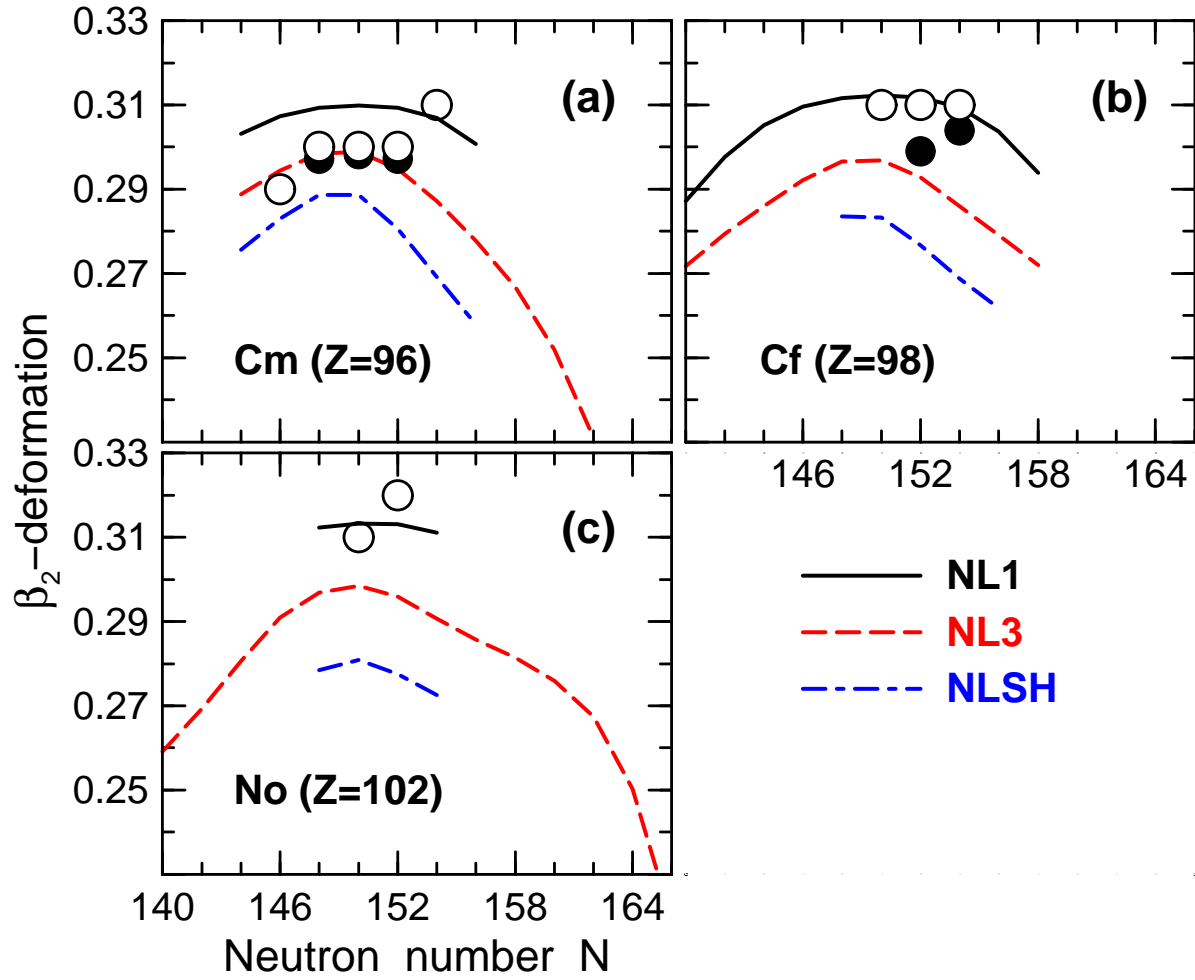


FIG. 15. The same as in Fig. 13, but for the chains of the Cm, Cf and No isotopes.

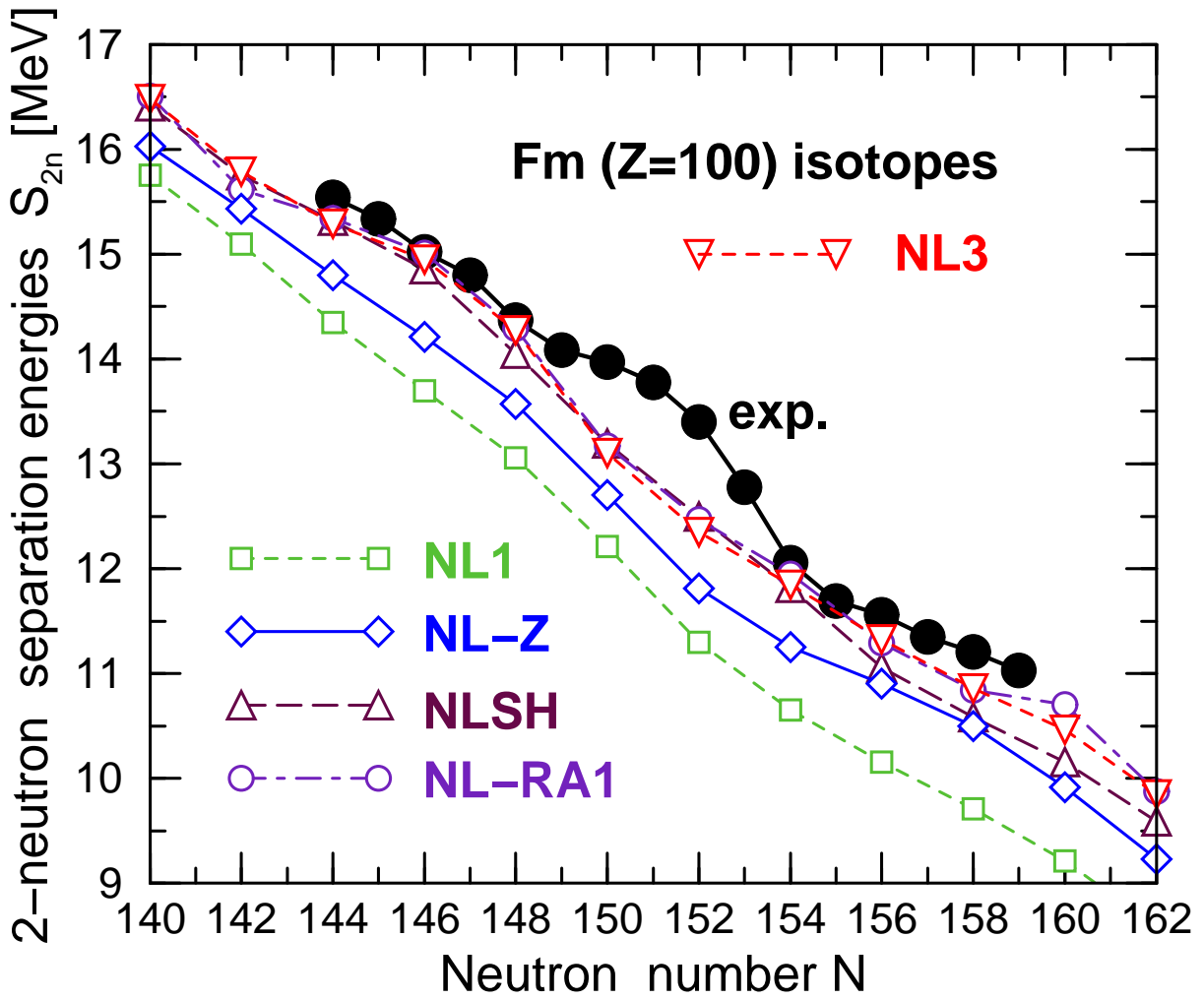


FIG. 16. The two-neutron separation energies $S_{2n}(Z, N)$ obtained in the CRHB+LN calculations for Fm ($Z = 100$) isotopes with different RMF parametrizations. Solid circles are used for experimental data, while open symbols for the theoretical results.

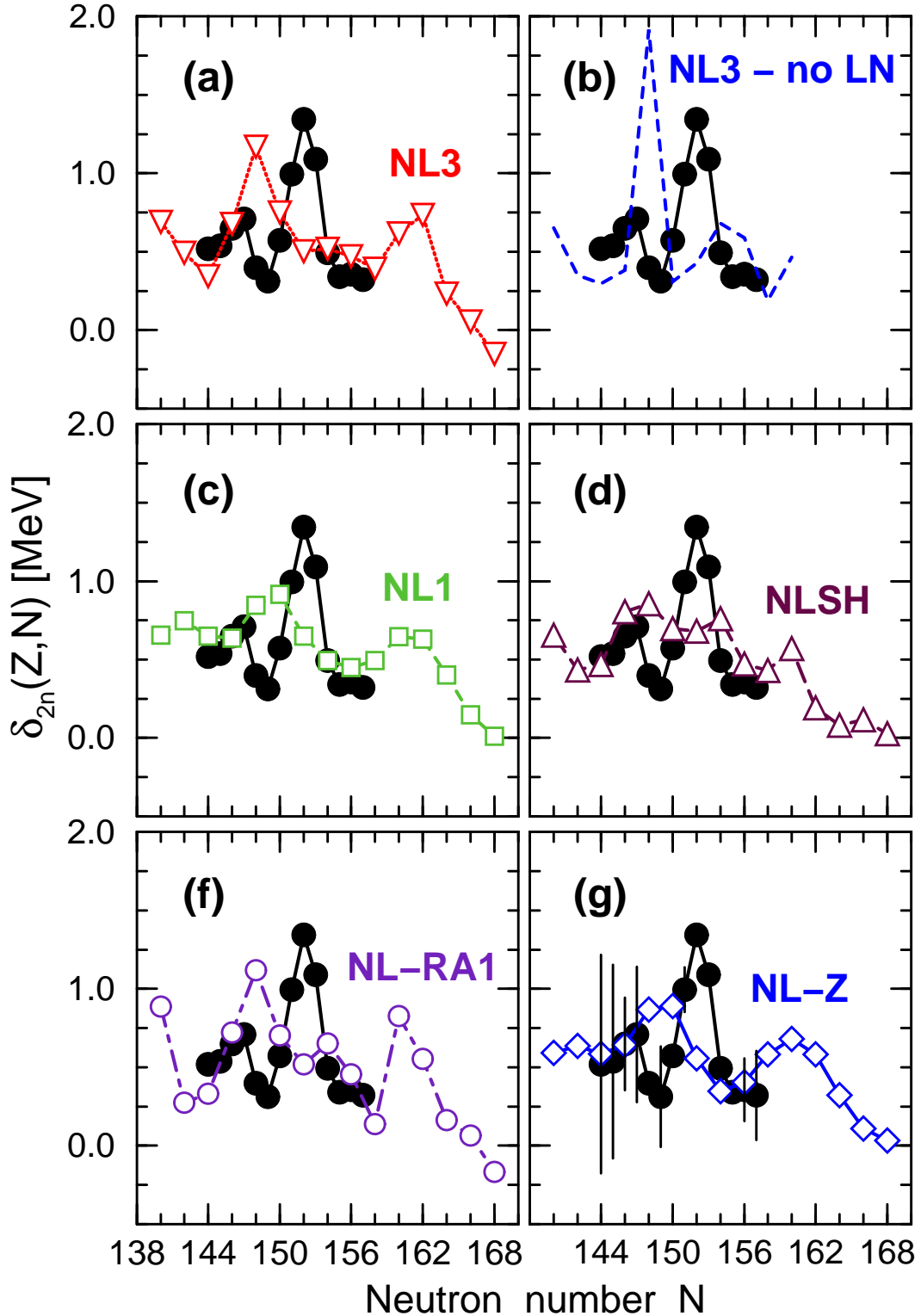


FIG. 17. The quantity $\delta_{2n}(Z, N)$ for Fm nuclei. The experimental data (solid circles) are compared with the results (open symbols) obtained in the CRHB+LN calculations with the indicated RMF parametrizations in panels (a-c-g). The results of the calculations without LN are shown in panel (b) by the dashed line. The experimental error bars are shown in panel (g).

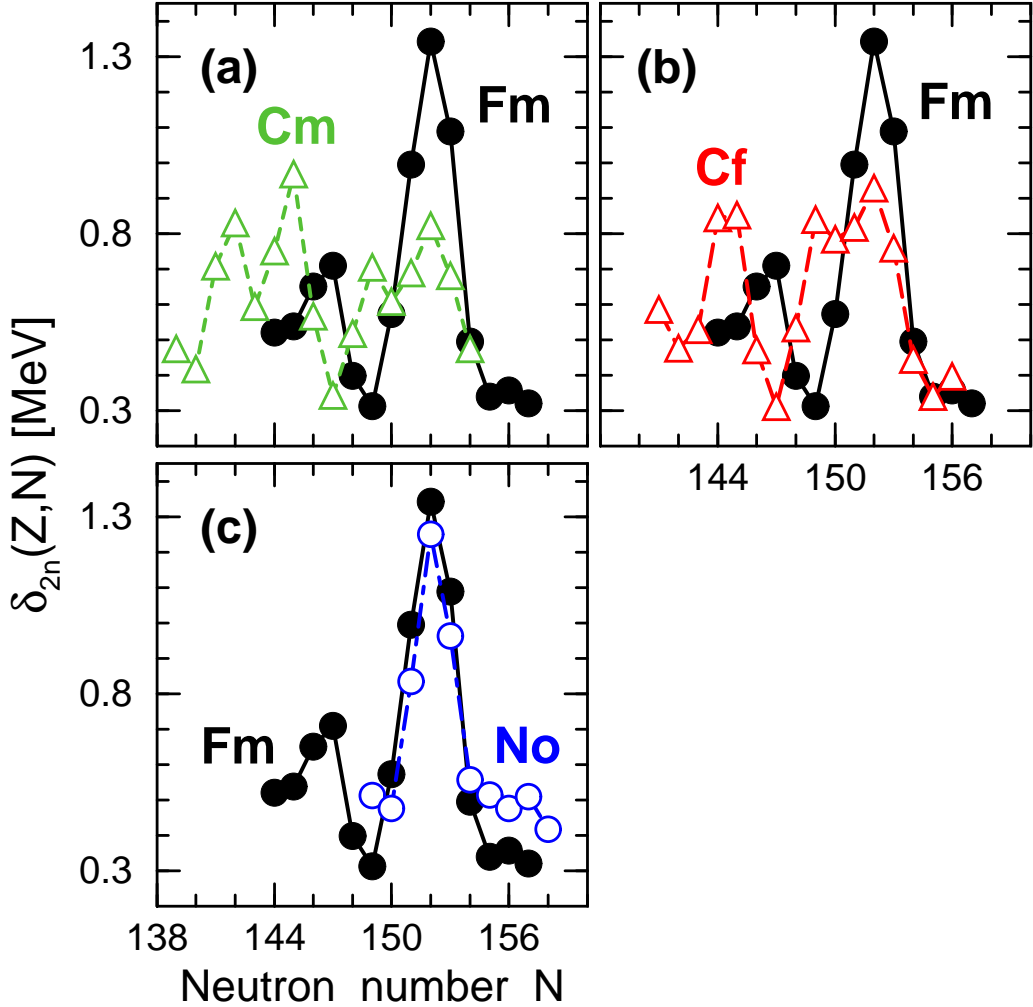


FIG. 18. Experimental $\delta_{2n}(Z, N)$ values, shown by open symbols for Cm ($Z=96$) (panel (a)) , Cf ($Z=98$) (panel(b)), and No ($Z=102$) (panel(c)) nuclei. In all panels the experimental values for Fm ($Z=100$) nuclei are shown by solid circles in order to indicate the variations of $\delta_{2n}(Z, N)$ with change of proton number Z .

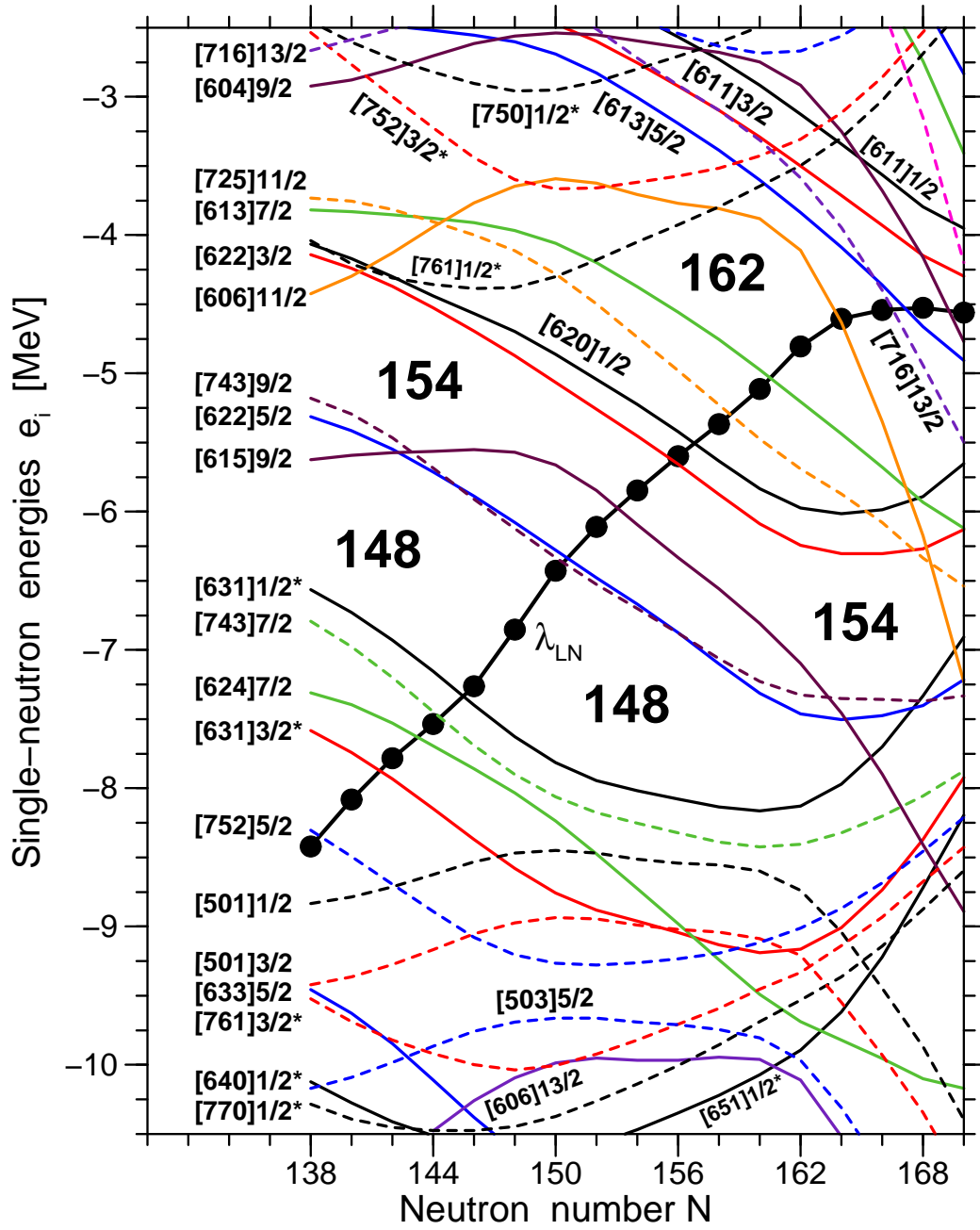


FIG. 19. Single-neutron energies in the Fm isotope chain as a function of neutron number N obtained at the equilibrium deformation in the CRHB+LN calculations with the NL3 parametrization. Solid and dashed lines are used for positive and negative parity orbitals, respectively. The λ_{LN} values are shown by solid line with solid circles. For other details, see caption of Fig. 2.

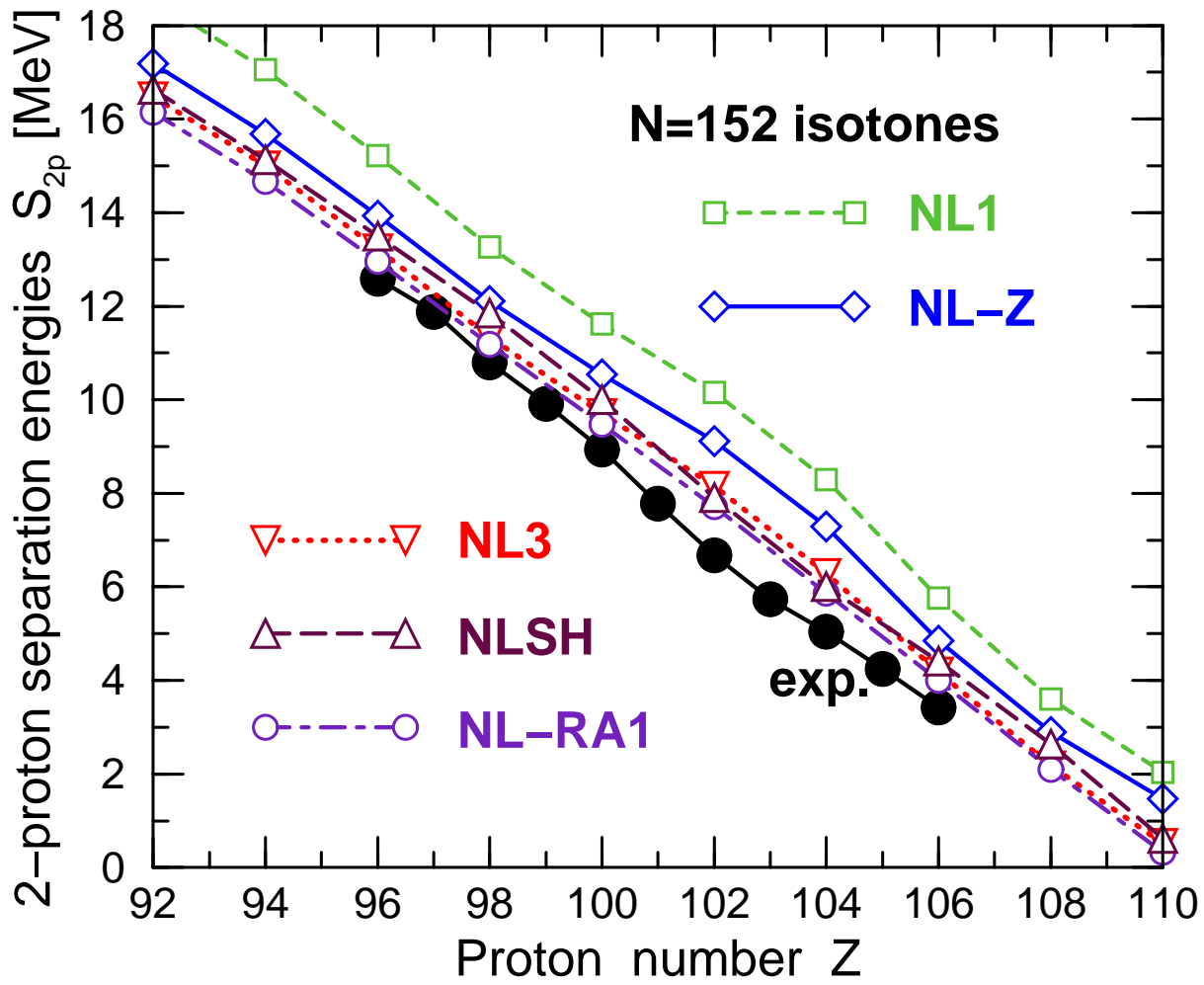


FIG. 20. The same as in Fig. 16, but for the two-proton separation energies $S_{2p}(Z, N)$ obtained for the $N = 152$ isotones.

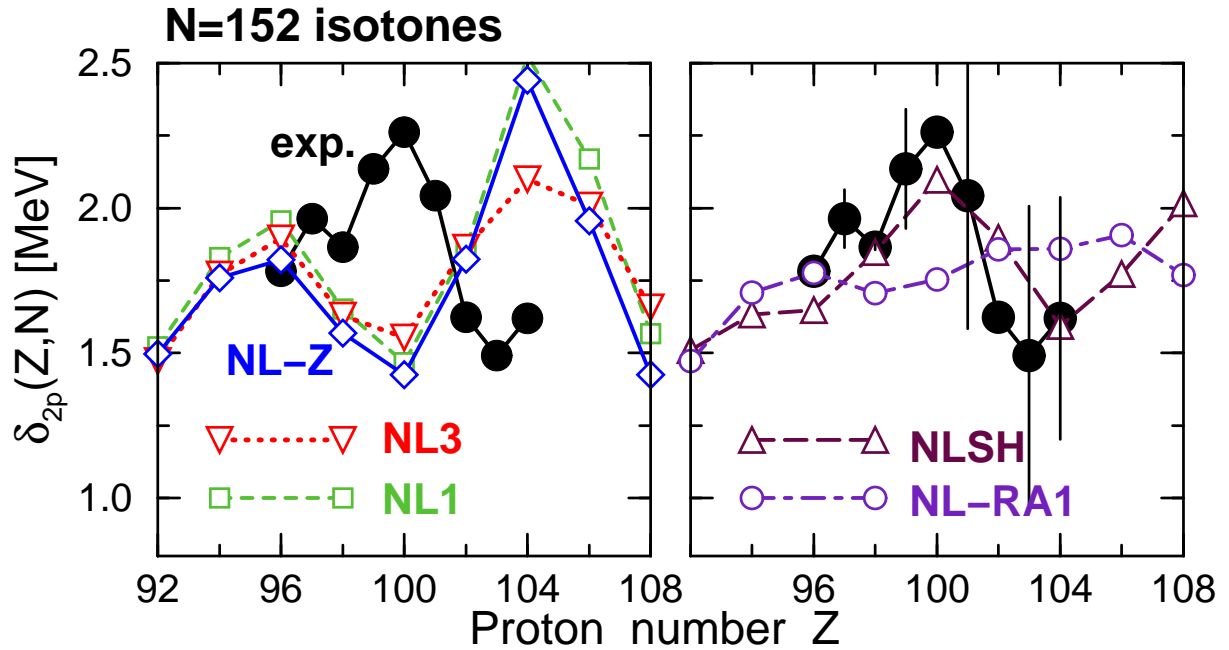


FIG. 21. The quantity $\delta_{2p}(Z, N)$ for the chain of $N = 152$ isotones obtained in the CRHB+LN calculations with indicated RMF parametrizations. Solid circles are used for experimental data, while open symbols for theoretical results. The experimental error bars are shown in panel (b).

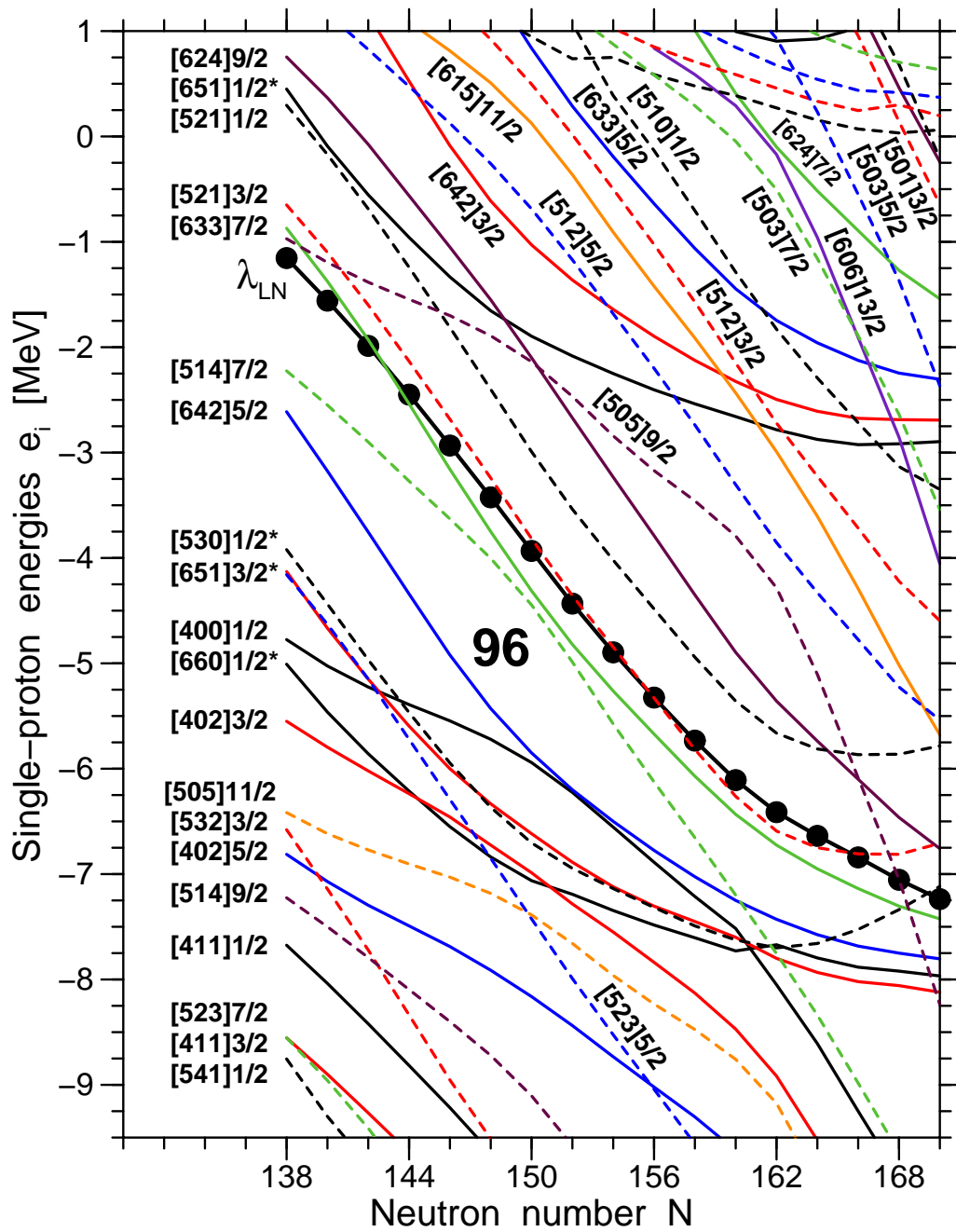


FIG. 22. The same as Fig. 19, but for the single-proton energies.

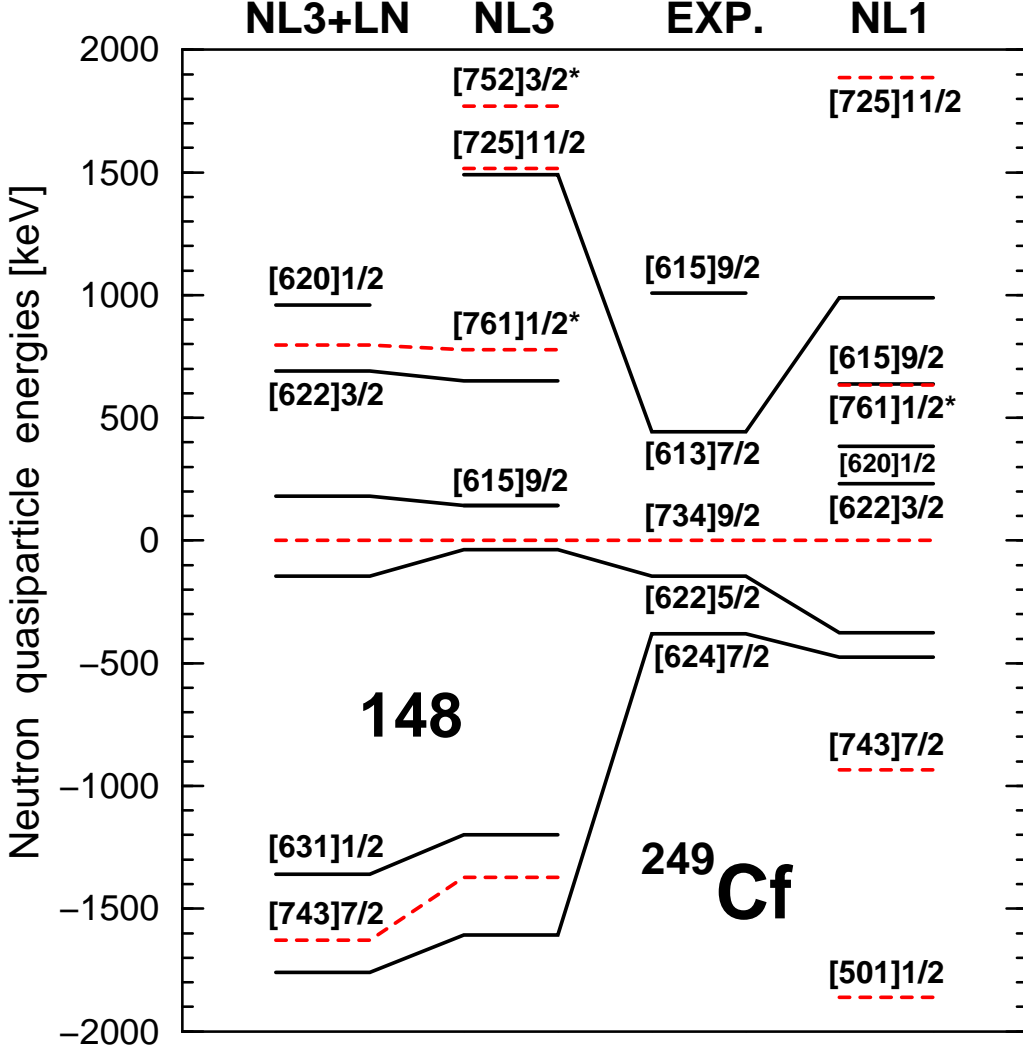


FIG. 23. Experimental and theoretical quasiparticle energies of neutron states in ^{249}Cf . Positive and negative energies are used for particle and hole states, respectively. The experimental data are taken from Ref. [81]. Solid and dashed lines are used for positive and negative parity states, respectively. The symbols 'NL3' and 'NL1' indicate the RMF parametrization. The CRHB results shown below them were obtained with original D1S Gogny force ($f = 1.0$) used in pairing channel and without particle number projection. 'NL3+LN' indicates results with the LN method, the NL3 parametrization and scaling f of the strength of D1S force (given in Table I). In each calculational scheme, attempts were made to obtain solutions for every state shown in figure. The absence of a state indicates that convergence was not reached.

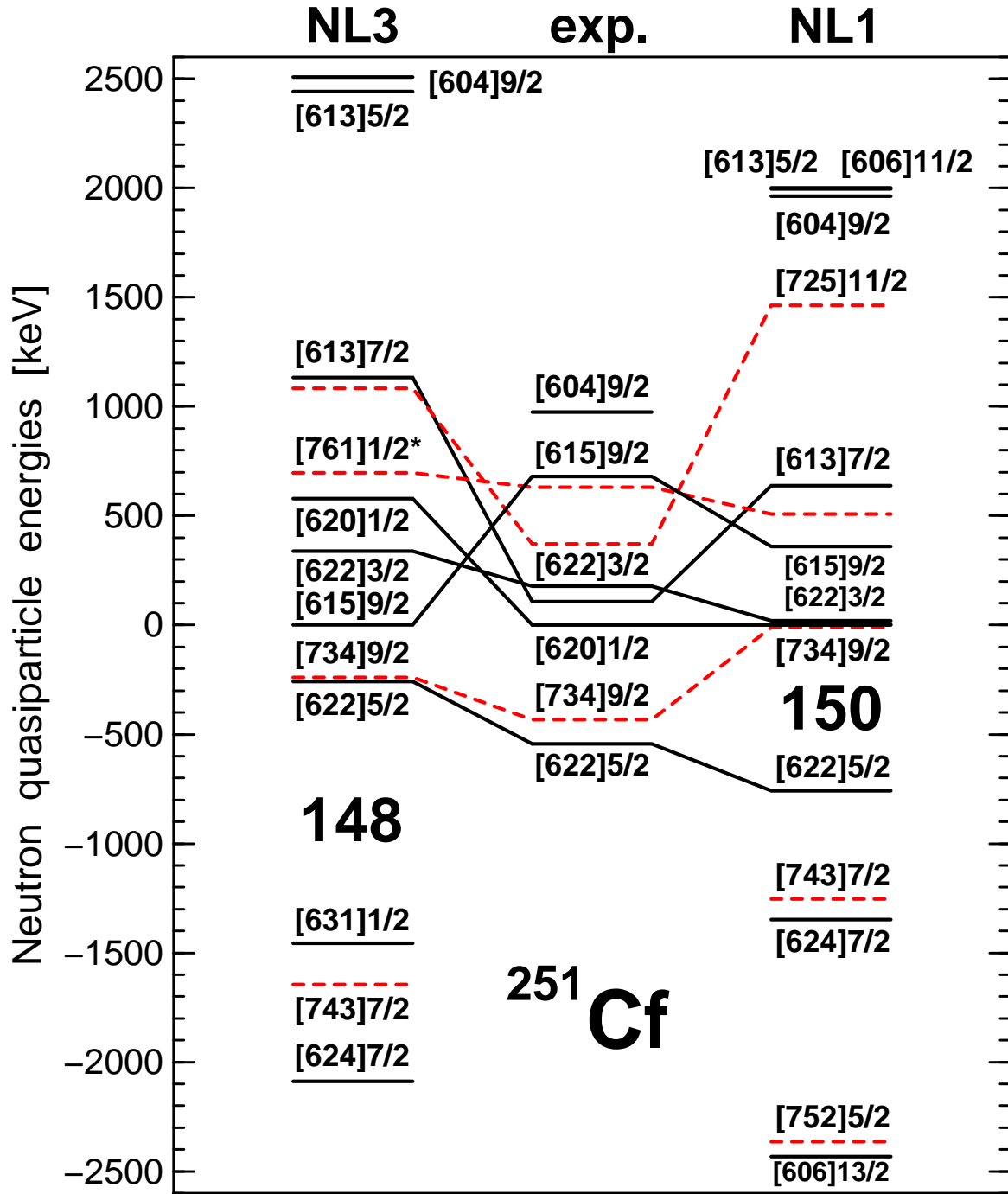


FIG. 24. The same as in Fig. 23 but for neutron states in ^{251}Cf . The experimental data are from Refs. [82,83,89].

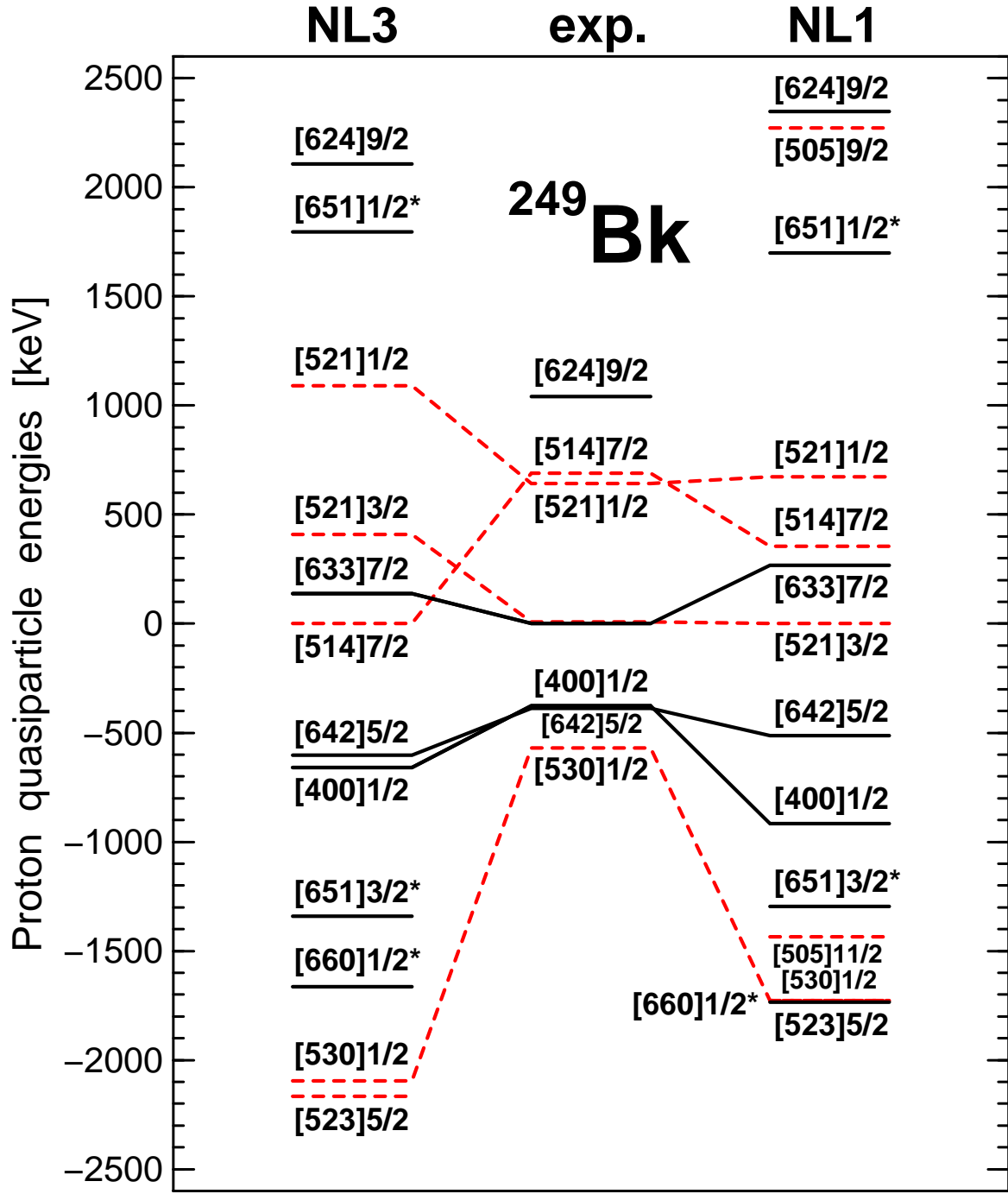


FIG. 25. The same as in Fig. 23 but for proton states in ^{249}Bk . The experimental data are from Ref. [80].

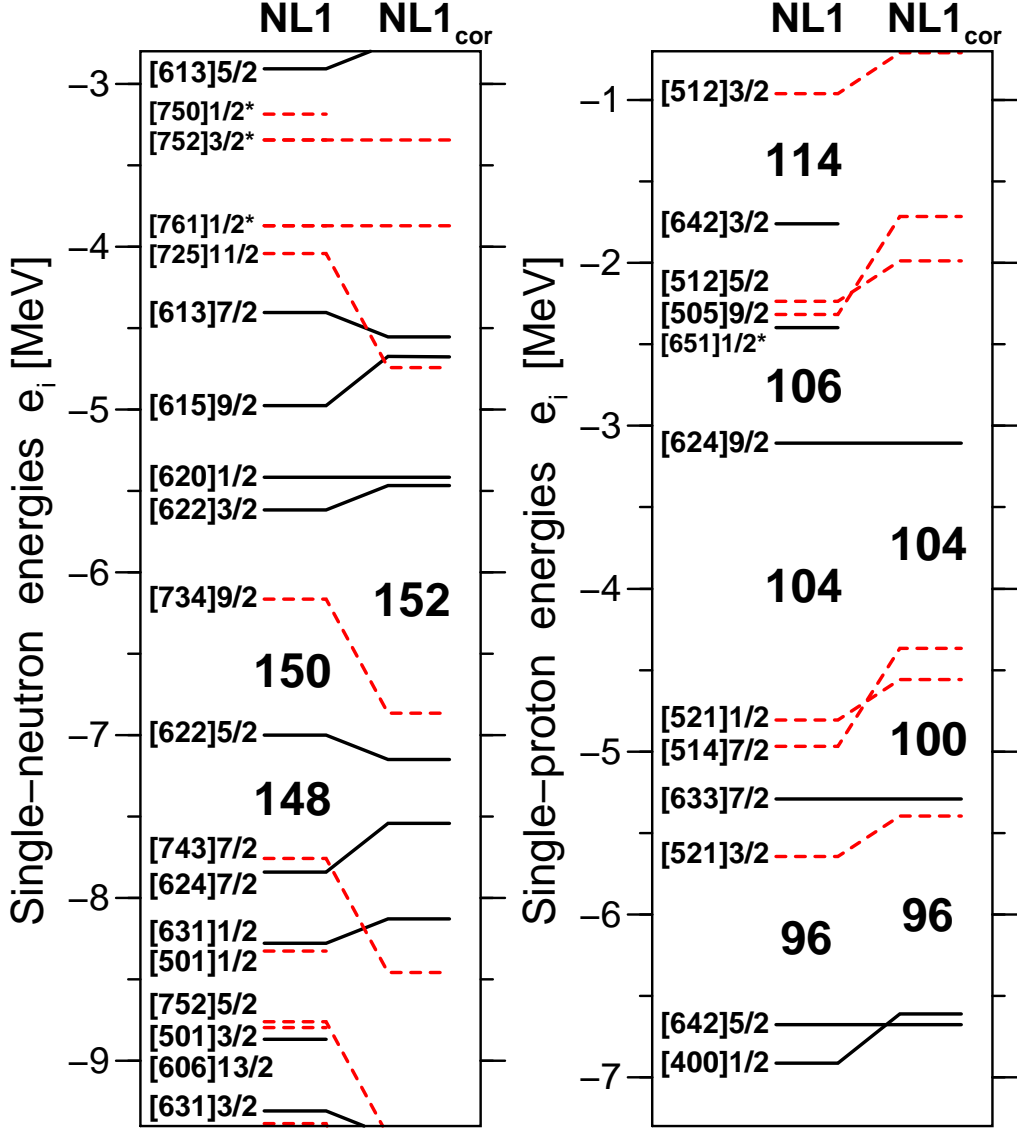


FIG. 26. Neutron and proton single-particle energies in ^{254}No . The columns marked by 'NL1' show the original spectra obtained with the NL1 parametrization (see Figs. 2 and 3). The columns 'NL1_{cor}' show how the spectra are modified if the energies were shifted as discussed in Sect. VI E and VID. Solid and dashed lines are used for positive and negative parity states. Deformed gaps are indicated.

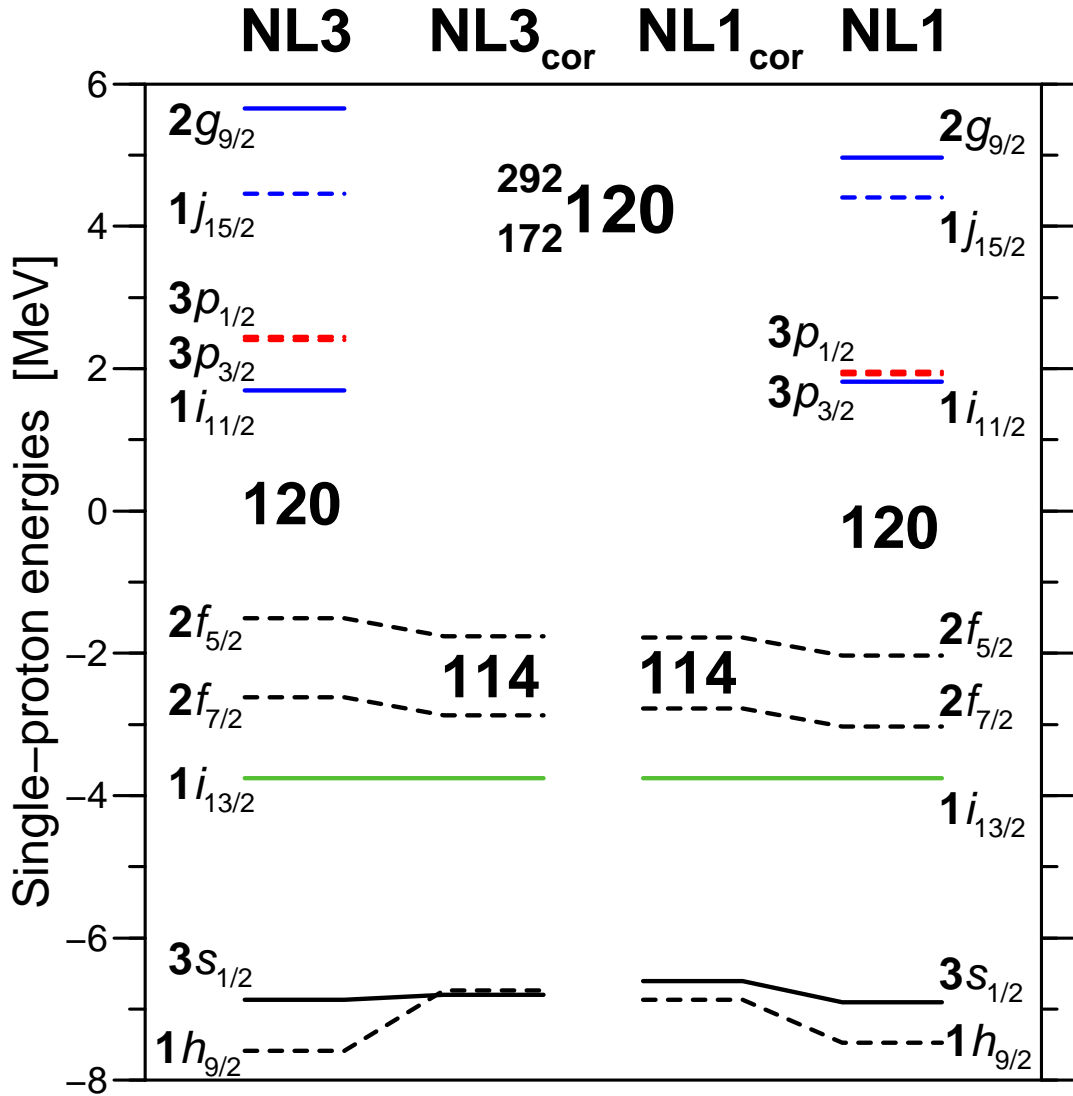


FIG. 27. Proton single-particle states in a $^{292}_{172}\text{120}$ nucleus. Columns 'NL3' and 'NL1' show the states obtained in the RMF calculations at spherical shape with the indicated parametrizations. The energy of the $1i_{13/2}$ state in the NL1 parametrization is set to be equal to that in NL3, which means that the energies of all states in NL1 (last column) are increased by 0.78 MeV. The columns 'NL3_{cor}' and 'NL1_{cor}' show how the spectra are modified if empirical shifts were introduced based on discrepancies between calculations and experiment for quasiparticle spectra in deformed ^{249}Bk (see Sect. VI E for numerical values). Solid and dashed lines are used for positive and negative parity states. Spherical gaps at $Z = 114$ and $Z = 120$ are indicated.

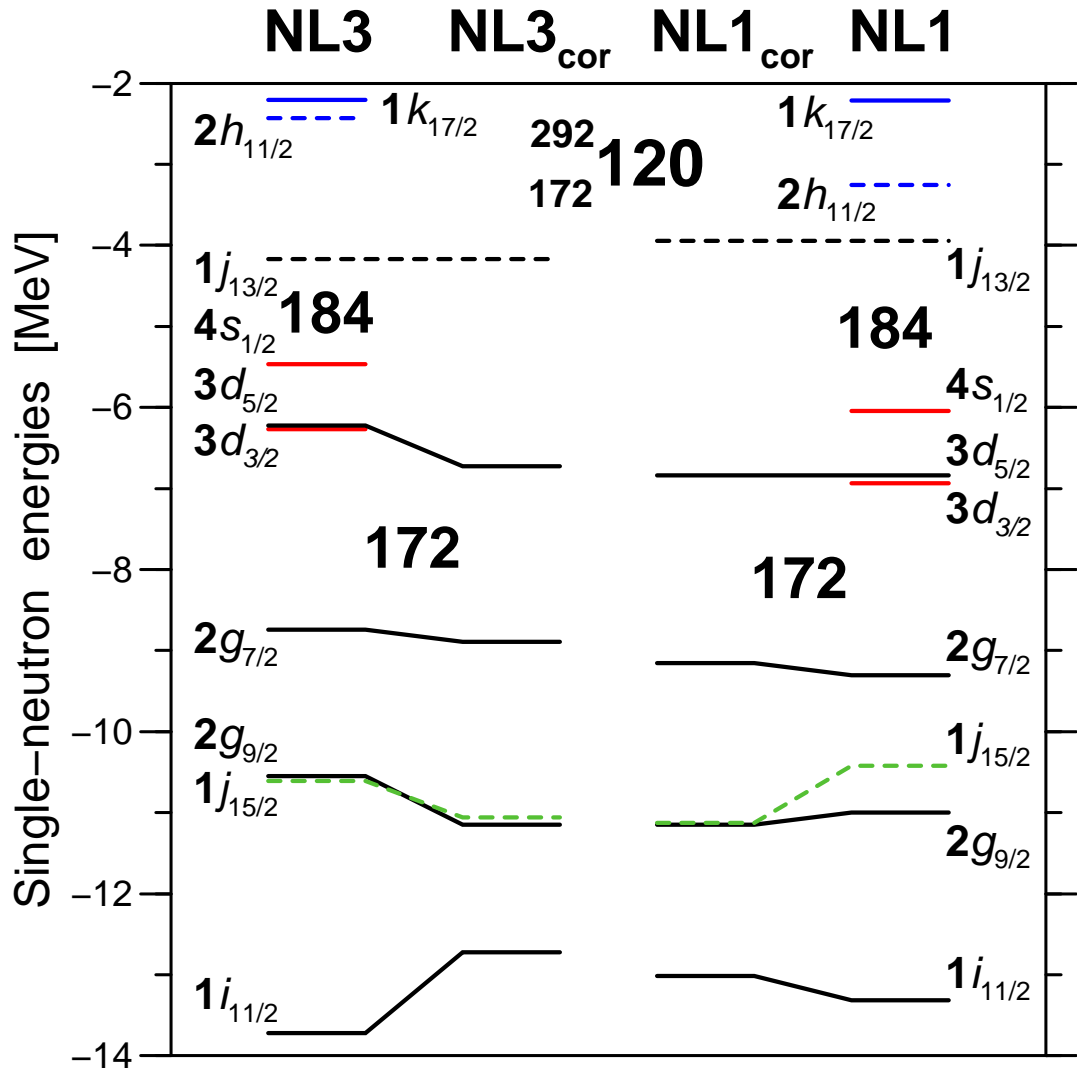


FIG. 28. The same as Fig. 27, but for neutron single-particle states. The energies of all states obtained with the NL1 parametrization (last column) are increased by 0.76 MeV in order to have the same energies of the $2g_{9/2}$ states in the second and third columns. Spherical gaps at $N = 172$ and $N = 184$ are indicated.

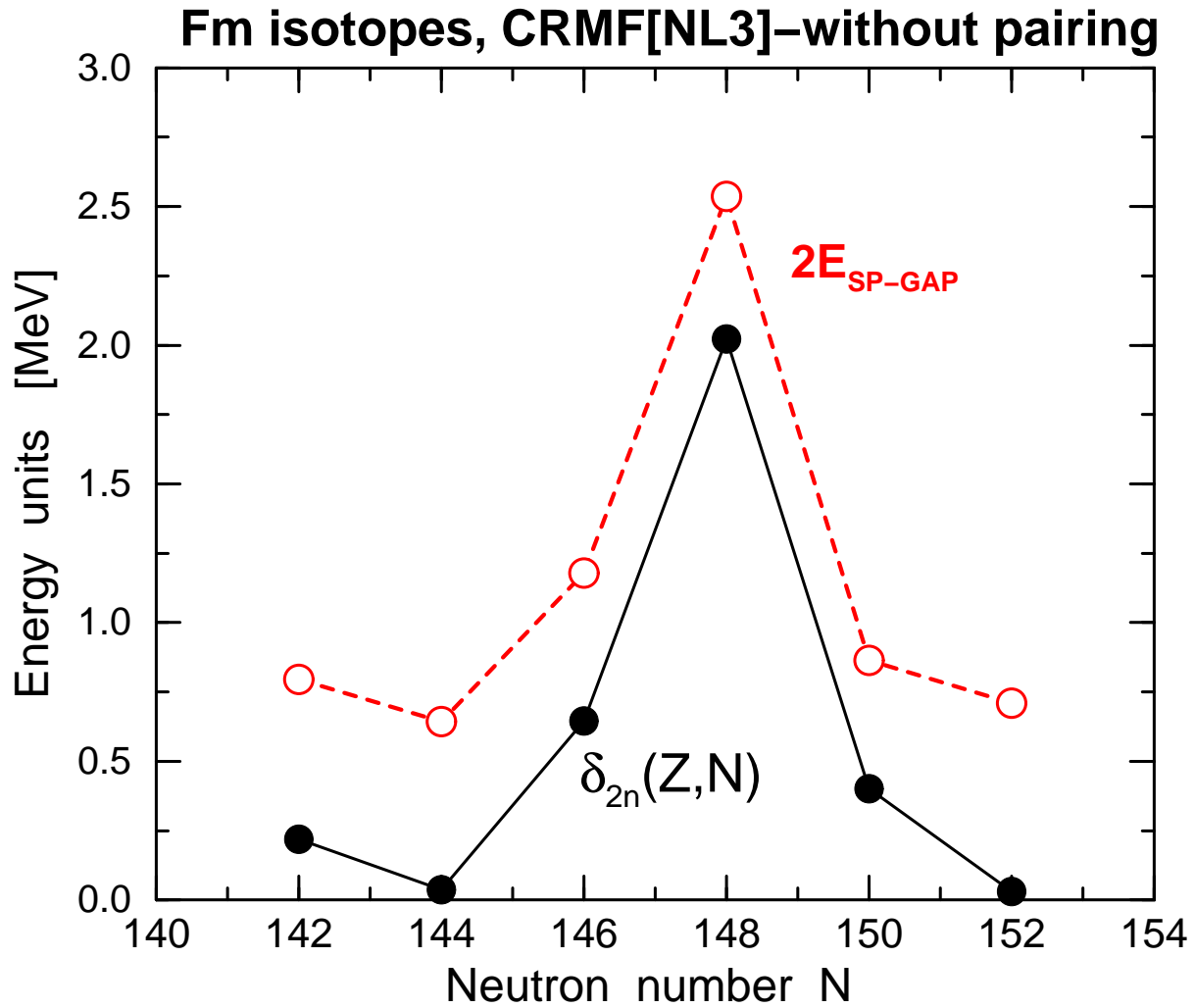


FIG. 29. Comparison of the $\delta_{2n}(Z, N)$ quantity with the twice the size of the shell gap $2E_{SP-GAP}$, which is the distance between the last occupied and first unoccupied orbitals. Both quantities are calculated with the NL3 parametrization and without pairing.

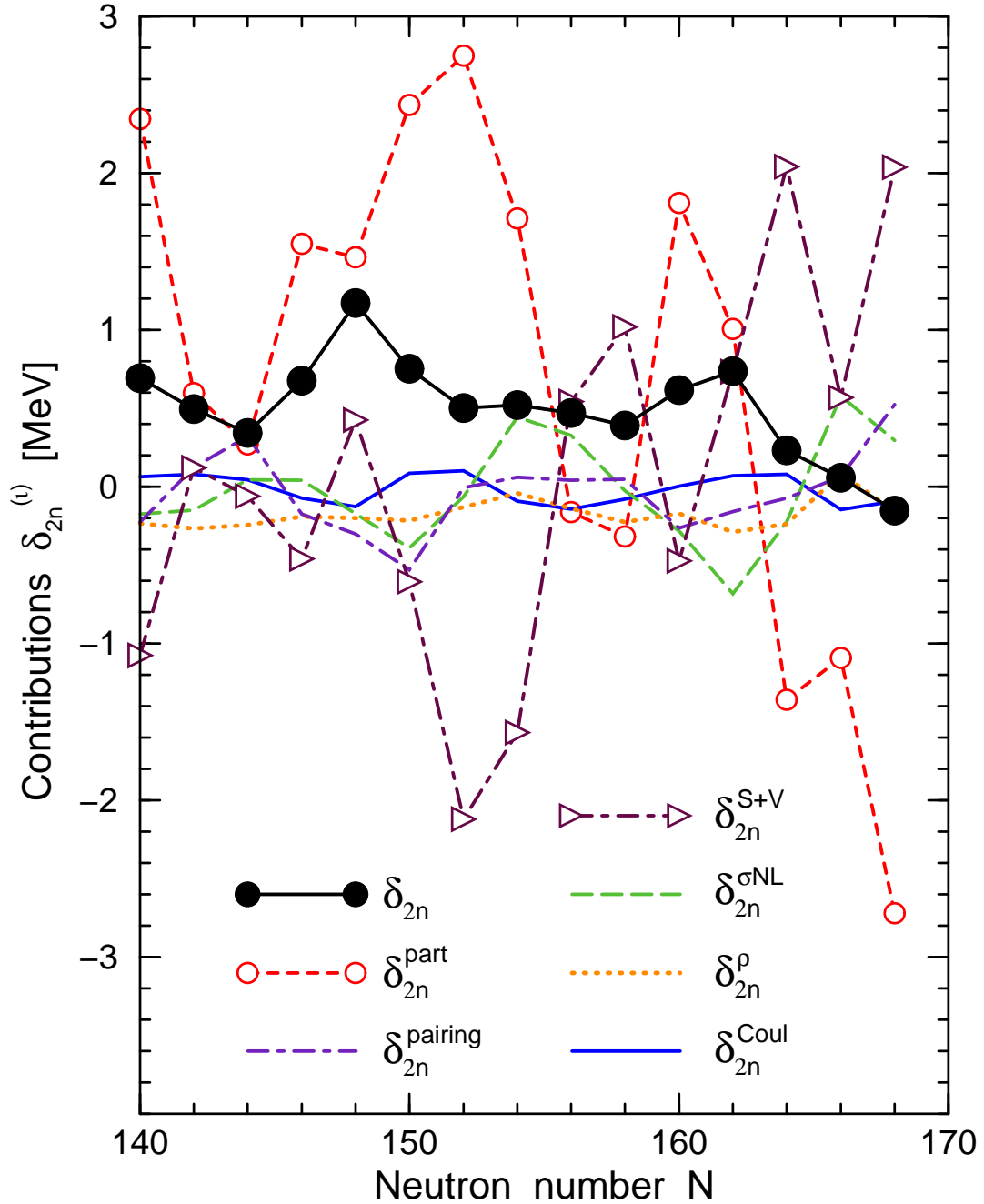


FIG. 30. The contributions $\delta_{2n}^{(i)}(Z, N)$ of the different terms of the CRHB+LN theory to the quantity $\delta_{2n}(Z, N)$ as a function of the neutron number N for the chain of the Fm isotopes. The contribution δ_{2n}^{LN} is not shown since it typically lies in the range from -30 keV up to $+30$ keV. The only exceptions are $N = 148$ and $N = 162$, where $\delta_{2n}^{LN} = 83$ and 62 keV, respectively.

TABLES

TABLE I. The scaling factors f of the Gogny D1S force (see Eq. (10)) used for different parametrizations of the RMF Lagrangian in the CRHB+LN calculations.

Parametrization	NL1	NL-Z	NL3	NL-RA1	NLSH
f	0.893	0.880	0.864	0.861	0.876

TABLE II. Three-point indicators of the odd-even staggering of binding energies $\Delta^{(3)}(N) = \frac{(-1)^N}{2} [B(N-1, Z) + B(N+1, Z) - 2B(N, Z)]$, where $B(N, Z)$ is the (negative) binding energy of a system with N neutrons and Z protons. An analogous proton indicator $\Delta^{(3)}(Z)$ is obtained by fixing the neutron number N and replacing N by Z . Column 1 indicates the type of indicator (proton $\Delta^{(3)}(Z)$ or neutron $\Delta^{(3)}(N)$) and nucleus with Z (proton indicator) and N (neutron indicator). Columns 3 and 4 give the results obtained in CRHB calculations with $f = 1.0$ for the D1S force and with the NL3 and NL1 parametrizations, while columns 5 and 6 give those obtained in CRHB+LN calculations with f values given in Table I.

$\Delta^{(3)}(\dots)$	exp	NL3	NL1	NL3+LN	NL1+LN
1	2	3	4	5	6
$\Delta^{(3)}(Z)$ [^{249}Bk]	0.399	0.516	0.515		
$\Delta^{(3)}(N)$ [^{249}Cf]	0.519	0.481	0.559	0.458	0.515
$\Delta^{(3)}(N)$ [^{251}Cf]	0.531	0.491	0.605		

TABLE III. Spherical subshells active in superheavy nuclei and their deformed counterparts active in the $A \sim 250$ mass region. The left column shows the spherical subshells active in the vicinity of the “magic” spherical gaps ($Z = 120, N = 172$). Their ordering is given according to the RMF calculations with the NL3 parametrizations in the $^{292}_{172}120$ system (see Figs. 27 and 28). Although the gaps depend on the specific RMF parametrization, the same set of spherical subshells is active with other parametrizations (see, for example, Fig. 4 in Ref. [17]). The right column shows the deformed quasiparticle states observed in $^{249}_{97}\text{Bk}_{152}$ [80] and $^{249,251}_{98}\text{Cf}_{151,153}$ [81–83]. The bold style is used for the states which may be observed in nuclides with $N \approx 162$ and/or $Z \approx 108$. The symbols ‘N/A’ (not accessible) are for the deformed states which typically increase their energy with deformation and thus are not likely to be seen experimentally.

Spherical subshell	Deformed state
Proton states	
$\pi 1j_{15/2}$	$\pi [770]\mathbf{1/2}$
$\pi 3p_{1/2}$	N/A
$\pi 3p_{3/2}$	N/A
$\pi 1i_{11/2}$	$\pi [651]\mathbf{1/2}$
$Z = 120$	
$\pi 2f_{5/2}$	$\pi [521]1/2$
$\pi 2f_{7/2}$	$\pi [521]3/2, \pi [530]1/2$
$\pi 1i_{13/2}$	$\pi [642]5/2, \pi [633]7/2, \pi [624]9/2$
$\pi 3s_{1/2}$	$\pi [400]1/2$
$\pi 1h_{9/2}$	$\pi [514]7/2$
Neutron states	
$\nu 1k_{17/2}$	$\nu [880]\mathbf{1/2}$
$\nu 2h_{11/2}$	$\nu [750]\mathbf{1/2}$
$\nu 1j_{13/2}$	$\nu [761]1/2$
$N = 184$	
$\nu 4s_{1/2}$	N/A
$\nu 3d_{5/2}$	$\nu [620]1/2$
$\nu 3d_{3/2}$	N/A
$N = 172$	
$\nu 2g_{7/2}$	$\nu [622]3/2$
$\nu 2g_{9/2}$	$\nu [622]5/2, \nu [613]7/2, \nu [604]9/2$
$\nu 1j_{15/2}$	$\nu [734]9/2, \nu [725]11/2$
$\nu 1i_{11/2}$	$\nu [615]9/2, \nu [624]7/2$

TABLE IV. Additional binding (ΔE_{NM}) induced by nuclear magnetism for different neutron (^{249}Cf) and proton (^{249}Bk) quasiparticle states obtained in the CRHB calculations with the NL3 parametrization and full strength (scaling factor $f = 1.0$) of the Gogny force. The quantity ΔE_{NM} is defined as the difference of binding energies obtained in the calculations with and without nuclear magnetism. As tested for a number of states, the change of the scaling factor f to the one given in Table I and/or the use of the LN method modifies ΔE_{NM} only marginally.

neutron state	ΔE_{NM} (keV)	proton state	ΔE_{NM} (keV)
$\nu[734]9/2$	-36	$\pi[521]1/2$	-16
$\nu[615]9/2$	-55	$\pi[514]7/2$	-35
$\nu[624]7/2$	-56	$\pi[633]7/2$	-22
$\nu[622]3/2$	-27	$\pi[624]9/2$	-23
$\nu[622]5/2$	-33	$\pi[521]3/2$	-27
$\nu[734]7/2$	-37	$\pi[523]5/2$	-33
$\nu[613]7/2$	-29	$\pi[642]5/2$	-23
$\nu[725]11/2$	-34		
$\nu[761]1/2^*$	-69		
$\nu[752]3/2^*$	-53		